Venting of Volcanic Hg and CO₂ through East Lake, Newberry Volcano, Oregon

By
S. Molly Wagner
Faculty Advisor: Johan Varekamp

A Thesis submitted to the Faculty of Wesleyan University in partial fulfillment of the requirements for the degree of Master of Arts in Earth and Environmental Sciences

Middletown, Connecticut   May 2019

Acknowledgements

<p style="text-align:center;">**Table of Contents**</p>

Abstract

Abstract

East Lake, one of the twin crater lakes at Newberry Volcano, Oregon, receives a gaseous flux of CO_2, Hg^0, and H_2S from the hydrothermal system below. This work presents an initial model for the mercury and carbon cycles within the lake. The rate of Hg input into the lake is recorded in the lake sediments, whereas analyses of Hg in the water column provides the pathways. The carbon cycling is derived from analyses of the water and CO_2 escape fluxes from the lake surface. Modeling of the surface fluxes as well as the carbon burial rate as a result of photosynthesis suggests a year-round input of ~25 tonnes CO_2 day^{-1} from below. The lake has a gaseous zone (~10% of surface area) near the shoreline hot springs with elevated CO2 fluxes. Mercury travels with the CO2 bubbles from the hydrothermal system into the lake, with concentrations of 3-8 ng L-1 total Hg (dissolved and particulate bound), with 10s to 100s ng L-1 in the gaseous zone. Methylmercury levels reach up to 40% of total Hg. The sediment carries 1-13 ppm Hg, with 5-13 ppm in core samples from the gaseous zone. The sediment Hg concentrations correlate with the abundance of Corg, except in the gaseous zone, which correlates with Stotal. It appears that two Hg pathways of fixation occur: (1) a largely inorganic pathway in the sediment/sediment-water interface in the zones of intense streaming H2S-CO2-Hg, and (2) an organic pathway in the lake waters that invokes oxidation of Hg, methylation, bioaccumulation, and deposition in association with Corg. Comparison of total water column Hg versus burial rate suggests a processing time of a few months between injection and extraction. The approximate depositional volume of Hg for the lake's existence

5

(6,500 years) is on the order of 10 tonnes of Hg. These results indicate that secular variations in CO2 fluxes can only be used when understanding the full chemical and physical lake system, given the large variations in monthly CO2. The data indicates that Newberry is a modest source of volcanic Hg, but is contained within the bounds of the lake.

Chapter 1: Introduction

Volcanic lakes receive subterranean inputs of hydrothermal gases or fluids including dissolved nutrients that support their ecosystems. Most 'normal' lakes receive carbon dioxide from the atmosphere and dissolved nutrients from their watershed. Crater lakes often have very small watersheds, so their ecosystems may depend on the hydrothermal inputs for a supply of nutrients, which is often accompanied by many other toxic substances like arsenic, mercury, and other heavy metals (Lefkowitz et al., 2016; Engle et al., 2006; Phelps and Buseck, 1980; Smith, 2010; Varekamp and Buseck, 1986). Yet life in these volcanic ecosystems thrives with diatoms, algae, and vegetation just as they do in non-volcanic lakes.

The purpose of this study is to quantify the inputs of mercury (Hg) and carbon dioxide (CO_2) that enter East Lake together from an underlying hydrothermal system, and to determine the fate of that Hg. The obtained fluxes will be used to determine the natural background fluxes of volcanic CO_2 and Hg at East Lake and will be compared to other volcanic sites, to place East Lake in a global context. The societal importance of these results concerns individual public health as East Lake is a popular site for recreational fishing, and large-scale safety as monitoring of secular changes in gas fluxes serves as a valuable tool to signal magmatic activity below the surface.

1.1 Mercury Cycling and Impacts

The element mercury ($_{80}$Hg) is a volatile trace constituent of the earth, found abundantly in heavy metal and coal deposits (Krabbenhoft and Sunderland, 2013). Lithospheric Hg is released naturally by degassing, wind entrainment of dust particles, volcanic eruptions, forest fires, and biogenic emissions. Basaltic eruptions are the primary mechanism of the release of Hg from the deep mantle (Morel et al., 1998). In recent geologic times, the anthropogenic release of Hg is associated with metal production from ores, waste handling and treatment, and burning of coal, peat, and wood (Morel et al., 1998). Natural Hg releases make up about 30% of the total flux into the atmosphere, whereas the remainder is composed of modern anthropogenic Hg releases and recycled other anthropogenic Hg, re-released from temporary storage in soils, freshwaters, and oceans (Selin et al. 2008). Currently, the most significant global Hg reservoirs are terrestrial soils hosting a large fraction of the older anthropogenic Hg. Increases in atmospheric CO_2 stimulate primary productivity, and these large Hg stores are likely to be released into the atmospheric reservoir in the future (Krabbenhoft and Sunderland, 2013). The modern northern hemispheric atmosphere holds 1.5 ng m^{-3} Hg^0 (Rizzo et al.).

Most Hg in the atmosphere exists as elemental gaseous Hg (Hg^0) and oxidizes to water-soluble Hg^{2+} on the surface of water droplets by reaction with Br as

$$Hg + Br + M \leftrightarrow HgBr + M \qquad\qquad \text{(Eq. 1.1)}$$

$$HgBr + X + M \rightarrow HgBrX + M, \quad X \equiv OH, Br, Cl \qquad\qquad \text{(Eq. 1.2)}$$
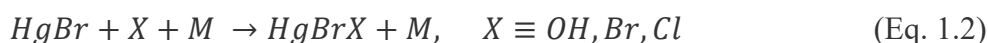
(Holmes et al., 2010). This oxidation occurs slowly in the atmosphere such that Hg

has a residence time of 6-12 months before it is deposited globally by wet

precipitation (Morel et al., 1998). Mercury(II) is then available to cycle through the

bio- and hydro-spheres until being stored back in the sedimentary lithosphere (Figure

1.1; Krabbenhoft and Sunderland, 2013).
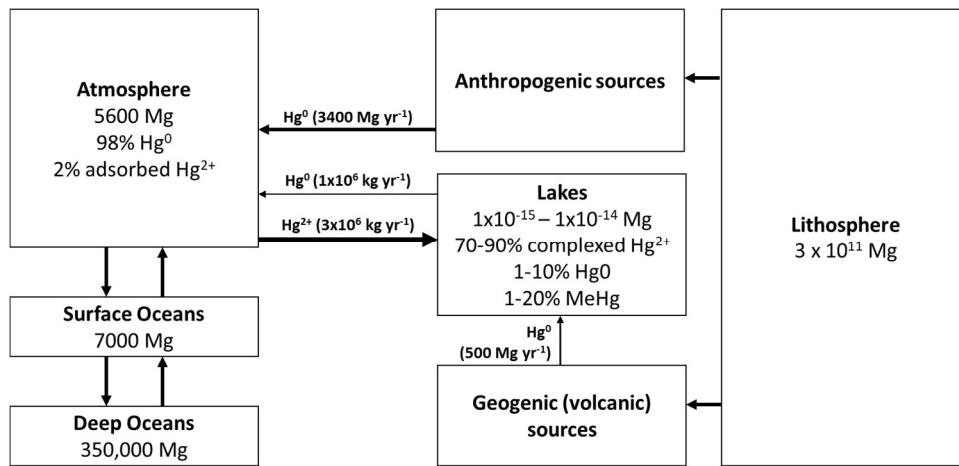
Figure 1.1. Box diagram of global Hg cycle, after Morel et al. (1998) and Selin (2009).

When degassed from reducing subsurface environments, Hg enters soils and

aquatic ecosystems in the elemental form. In non-anoxic waters it will be converted to

Hg^{2+} (Morel et al., 1998). In global oxic freshwaters, total Hg levels range between 1

and 20 ng L^{-1} (Morel et al., 1998).

The main mechanisms of Hg loss from lakes and the marine environment are

sedimentation and gas evasion (Figure 1.2). The proportion of each is a function of

the Hg content in epilimnion that can be reduced and thus be made available as gas

(Morel et al., 1998). At Hg concentrations greater than 10 ng L^{-1}, microbial action is

the dominant factor controlling reduction of Hg^{2+} and Hg^0 will be primarily found

near the sediments and transported to upper waters by diffusion and advection. In waters with lower total Hg concentrations, Hg^0 is highest near the air-water interface due to photoreduction processes. Particulate Hg in the water column is usually tightly held with suspended organic matter or iron oxides, which will ultimately be deposited as lake sediments (Morel et al., 1998).
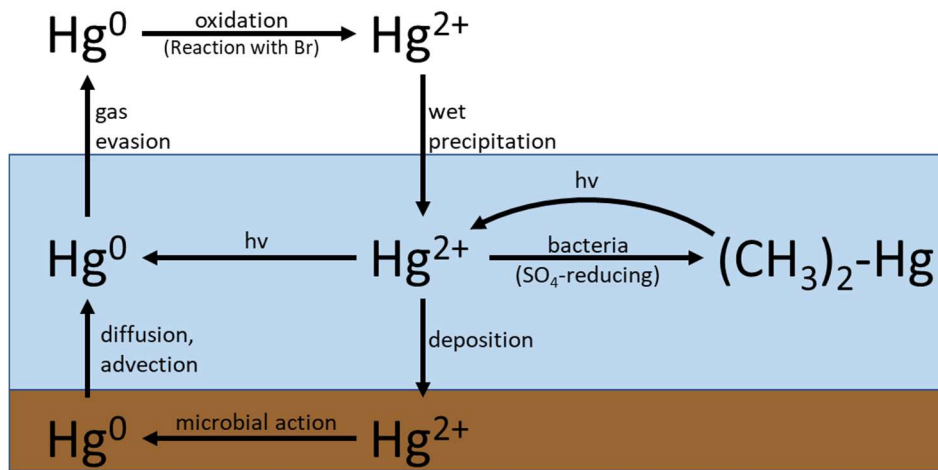
Figure 1.2. Processes of Hg cycling in a normal (non-volcanic) lake.

Mercury becomes a threat to human and ecosystem health when inorganic Hg becomes methylated (MeHg), which serves as a potent neurotoxin to humans and animals (Krabbenhoft and Sunderland, 2013). Methylation rates correlate in time and space with the abundance and activity of sulfate-reducing bacteria that catalyze the process. There is a net demethylation in oxic surface waters due to photochemical processes (Morel et al., 1998). Levels of MeHg range from below detection in surface waters to 1 ng L^{-1} in the deep waters with low oxygen concentrations (Morel et al., 1998).

Most Hg enters the water system as Hg^{2+} and when it adsorbs onto organic matter or other substrates, it is unavailable to be methylated and MeHg levels remain low. However, high concentrations of dissolved organic carbon (DOC) can keep Hg in solution, thus making it available for the bacteria that will carry out methylation (Ullrich et al., 2001).

Two forms of Hg (monomethyl-Hg and dimethyl-Hg) are available for biological uptake but only the monomethyl species is available for accumulation in the food chain (Table 1.1; Ullrich et al., 2001). Mercury must be transported across specialized cation transporters in the lipid membrane that surrounds unicellular organisms for bioaccumulation to occur. It must then be retained and passed on to predators (Morel et al., 1998). Bioaccumulation will not occur for the forms Hg^{0}, Hg^{2+}, and Me_2Hg, which are bound to parts of the prey that will eventually be excreted. Only MeHg that is bound to a soluble fraction of cell will continue to be passed along to higher levels in the ecosystem when assimilated by predators (Morel et al., 1998).

	MeHg/Total Hg
Water column	10%
Phytoplankton	15%
Zooplankton	30%
Fish	95%

Table 1.1. Percent of MeHg per total Hg in levels of the average water system. MeHg is the vector through which biomagnification occurs, as it binds well to material that moves up the food chain without excretion (Morel et al., 1998)

The Hg^{2+} ion shows a strong chemical affinity for sulfide and can be found in complexes including HgS_2H_2, HgS_2H^-, HgS_2^{2-}, and CH_3HgS^- (Morel et al., 1998). The form $HgS_{(s)}$ is known as cinnabar or metacinnabar, a mineral with an extremely low solubility product. It is stable at very low concentrations of Hg^{2+} and reduced S in hydrothermal fluids. When S^{2-} concentrations are high, the Hg^{2+} will be complexed and not available for cinnabar precipitation (Morel et al., 1998). Alternatively, HgS may precipitate from the gas phase through reactions of H_2S with Hg^0 vapor (White, 1971; Varekamp and Buseck, 1986).

1.2 Processing of Gases in Volcanic Lakes

About 16% of Holocene volcanoes contain crater lakes (Delemelle and Bernard, 1999). The constant diffusion of gases into crater lakes serves as an accessible lens for observing subsurface processes than periodic eruption of gas (and ash and lava) from a vent. Volcanic lakes act as surface manifestations of subsurface hydrothermal water-rock interaction, but the water compositions are further influenced by dilution by meteoric water, evaporation, drainage, recirculation, and organic processes of the ecosystem (Mazot and Bernard, 2015).

Volcanic gas emissions represent a path of exposure to magma bodies at depth, principally along zones of high permeability in the crust (D'Alessandro et al., 1997). Concentrations of the most common volcanic gases – H_2O, CO_2, and SO_2 – depend on the magma source rocks, the degree of partial melting, and the differentiation mechanism (Schmincke, 2004). After water vapor, CO_2 is the most

12

abundant species and makes up 10-40% of emitted gas (Hards, 2005). Relative proportions of volcanic gases are primarily affected by near-surface processes when they mix with meteoric water or hydrothermal fluids and are thus dictated by their solubilities in water (Rizzo et al., 2019, Schmincke, 2004).

When its saturation point is exceeded or when it is distilled out by another gas, a free gas phase is released from a magma body. Carbon dioxide is the first gas to be released in a silicate melt, followed by S gas species. Changes in the relative proportions of these gases can signal a new eruption. Therefore, tracking gas emissions is a useful tool in volcanic monitoring (Schmincke, 2004). Many studies have attempted to quantify global CO_2 emissions from various volcano types to better understand how this input affects the Earth's environment (Table 1.2). The rate of volcanic degassing from the Earth is also a topic of interest as it is a major factor controlling the long time scale partial pressure of CO_2 in the atmosphere (Hards, 2005).

When incoming CO_2 reacts with the water, it will form species like H_2CO_3, HCO_3^-, and CO_3^{2-}. Some acid volcanic lakes (pH < 4) let CO_2 pass directly through the water column without being absorbed into the dissociated species. Acidic lakes thus tend to show higher CO_2 emission rates that neutral and alkaline lakes (614, 201, and 5.5 t km^{-2} day^{-1}, respectively; Mazot and Bernard, 2015). The flux reaches a steady state once a neutral lake is saturated with CO_2, and neutral lakes will emit similar amounts of CO_2 as acid lakes.

Volcanic CO_2 Input	CO_2 emission Source	Method	Reference
540 Mt yr $^{-1}$	**Subaerial** volcanoes	Direct measurement, remote sensing	Burton et al., 2013
300 Mt yr $^{-1}$	**Subaerial** volcanoes	Direct sampling, $C/^3He$ ratios	Morner and Etiope, 2002
167 Mt yr $^{-1}$	**Global** volcanoes	Correlation spectrometry with SO_2	D'alessandro et al., 1997
80-132 Mt yr $^{-1}$	**Intraplate** volcanism	Direct sampling, $C/^3He$ ratios	Morner and Etiope, 2002
117±19 Mt yr $^{-1}$	Global **volcanic lakes**	Floating accumulation chamber	Perez et al., 2011
94 Mt yr $^{-1}$	Global **volcanic lakes**	Direct measurement, remote sensing	Burton et al., 2013

Table 1.2. Estimates of global CO_2 contributions from various studies and methods. Volcanic lakes account for about 20% of CO_2 flux into atmosphere.

The condition for CO_2 evolution from a lake surface is the ΔP_{CO_2} between the internal and atmospheric P_{CO_2}. If the lake P_{CO_2} exceeds the standard 0.4 bar atmospheric value, diffusion over the water-air interface will enable CO_2 to escape. Alternatively, in lakes with vigorous CO_2 inputs from below, remnant bubbles may reach the lake surface and escape.

Carbon dioxide evolution through and out of the lake may follow one of two pathways: an active bubbling flux or a passive degassing one (Mazot and Taran, 2009). In an active bubbling system, bubbles that have entered from the bottom of the lake may maintain a discrete form and escape at the surface. These bubbles start at high pCO2, but partially dissolve to a much smaller size as they travel. That dissolved

CO_2 accounts for the latter method of degassing, where the pCO_2 gradient between the water and air induces a flux to the atmosphere. Zones in these lakes with the highest CO_2 fluxes are usually indicators of underlying tectonic structures, namely faults and fractures that serve as main transport pathways of gases to the surface (Andrade et al., 2016, Mazot and Bernard, 2015).

Volcanic lakes receive either direct or hydrothermally processed volcanic gases, which are then modified by lake processes. When overprinting of lake processes is removed, remaining temporal (secular) variations in CO_2 fluxes are often related to changes in volcanic activity levels. Typical lake gas exchange and equilibration with the atmosphere is dominated by photosynthesis and by oxidative respiration/decay, which process oxygen and CO_2 as

$$6\ CO_2 + 6\ H_2O \rightarrow C_6H_{12}O_6 + 6\ O_2 \text{ (photosynthesis)} \qquad \text{(Eq. 1.3)}$$

$$C_6H_{12}O_6 + 6\ O_2 \rightarrow 6\ CO_2 + 6\ H_2O \text{ (respiration/decay).} \qquad \text{(Eq. 1.4)}$$

A highly productive lake in which there is a large amount of photosynthesis will be home to abundant algae, which fill the surface waters with O_2 and may deplete them of CO_2 if recharge with atmospheric CO_2 is slow. As these organisms die off and settle to the lake floor, they consume O_2 and supply CO_2 back to the water. The thermal stratification of the lake impedes mixing of surface and deep waters through the summer season, whereas turnovers in the fall and spring create thoroughly mixed lakes for a limited time.

Fluvial input supplies dissolved CO_2, bicarbonate, and particulate organic carbon (C_{org}) in 'normal' lakes. However, many volcanic lakes are situated within the

small watershed of a crater and do not receive such an external carbon supply. In volcanic lakes, the additional supply of CO_2 to the bottom waters from the sub-surface is often accompanied by additional volcanic volatiles including Hg. Extensive effort has been put into studying how volcanic CO_2 inputs interact with the lake system (Perez et al., 2011; Andrade et al., 2016; Mazot and Bernard, 2015).

1.3 Mercury Emission and Uptake

Measuring degassed Hg can be a useful tool for monitoring magma influx and forecasting volcanic activity because most of what is initially present in the magma is released to the atmosphere before solidification, due to its volatility (Varekamp and Buseck, 1981). Changes in Hg flux from soils can be signals of magmatic or fluid intrusion (Varekamp and Waibel, 1987). The primary mechanism of Hg release and fractionation in fossil and active hydrothermal systems is the separation of the fluids from the gas phase (Smith, 2010).

The primary control on concentrations of Hg in coexisting thermal waters and vapor phases is the amount of vapor phase separation from those thermal waters. Subsurface heating partitions the vapor phase, and waters are usually depleted in Hg by the time they near the surface. However, that vapor may intersect the surface to form fumaroles and acid hot springs (Phelps and Buseck, 1980).

The amount of Hg released from a volcanic system to the atmosphere varies with eruption type and level of processing since release from the magma. Non-explosive (ash-poor) volcanoes emit an average of 20 Mg yr^{-1}, while explosive (ash-

rich) volcanoes emit 100s of Mg yr^{-1} (Pyle and Mather, 2003). Fumes before an eruption carry a large ratio of Hg/SO$_4$ because early escape of CO$_2$ from a magma distills Hg. Volcanic domes are depleted in volatiles and demonstrate a smaller Hg/SO$_4$ ratio because they come from older, evolved magma bodies (Varekamp and Buseck, 1986). Likewise, fumaroles represent the highly processed and low-temperature endmember of emissions and thus often underestimate Hg emission rates (Pyle and Mather, 2003).

Volcanic Hg pollution has the potential to affect environments considerable distances from the source as the buoyant gas-rich plumes rise from summit craters and are injected into the troposphere. Records from peat bogs and ice cores show instances associated with massive volcanic atmospheric injections where the steady-state pre-industrial atmospheric burden increased 5- to 10-fold. The resulting Hg accumulation rates on earth surface nearly equal those of peak anthropogenic pollution (Pyle and Mather, 2003).

Many previous volcanic degassing studies have focused on the Hg/S or Hg/SO$_4$ ratio as sulfur degassing has been exhaustively studied (Table 1.3). This method has yielded consistent flux estimates for volatile metals that are present only as condensed particles in volcanic plumes such as Pb, Cu, and Zn. However, this method can lead to uncertainties across four orders of magnitude for Hg because the mass proportions of Hg/SO$_4$ is highly variable across volcano types and S phases (Pyle and Mather, 2003). Sulfur concentrations in volcanic systems are challenging to measure due to the formation of non-volatile compounds such as sulfides. It is

generally present in magma in the reduced form, S_2^-, but as H_2S or SO_2 depending on temperature and degree of oxidation (Schmincke, 2004). Measuring the Hg/CO_2 ratio will be a more accurate portrayal of deep-Earth chemistry because measurement of CO_2 gas flux is more representative than the measurement of sulfur gas flux.

Volcanic Hg Input	Hg emission source	Reference
700 t yr^{-1}	Degassing and erupting volcanoes	Pyle and Mather, 2003
1,000-7,000 t yr^{-1}	Global volcanoes	Varekamp and Buseck, 1981
1290 t yr^{-1}	Active (800) plus passive (30) degassing, geothermal flux (60), and soil degassing (400)	Varekamp and Buseck, 1986
76 +/- 30 t yr^{-1}	Passive degassing of subaerial volcanoes	Bagnato et al., 2014

Table 1.3. Estimates of global volcanic Hg emission from various sources and methods. Passively degassing volcanoes account for a few percent of the global flux.

Chapter 2: Background

2.1 Geologic Setting and Newberry Volcano

Newberry volcano, Oregon (43°43'50.4" N 121°12'35.7" W, elevation 6,400 ft) is one of the largest Quaternary volcanoes in the continental United States with eruptions beginning at least 0.5 million years ago (Tepee Draw ash-flow tuff). It sits 60 km east of the Cascade Arc but is itself a 1600 km^2 shield volcano. The summit caldera is 7 km across (Figure 2.1), the result of at least 25 Holocene eruptions with the most recent dated to 1300 k.a. (Big Obsidian Flow, Paulina Lake Ash Flow, Newberry Pumice) (MacLeod and Sherrod, 1988). It is a collapse structure of nested ring fractures and measures up to 500 m deep but was likely deeper before accumulating Pleistocene and Holocene sequences of flows, tuffs, and sedimentary rocks (MacLeod and Sherrod, 1988).
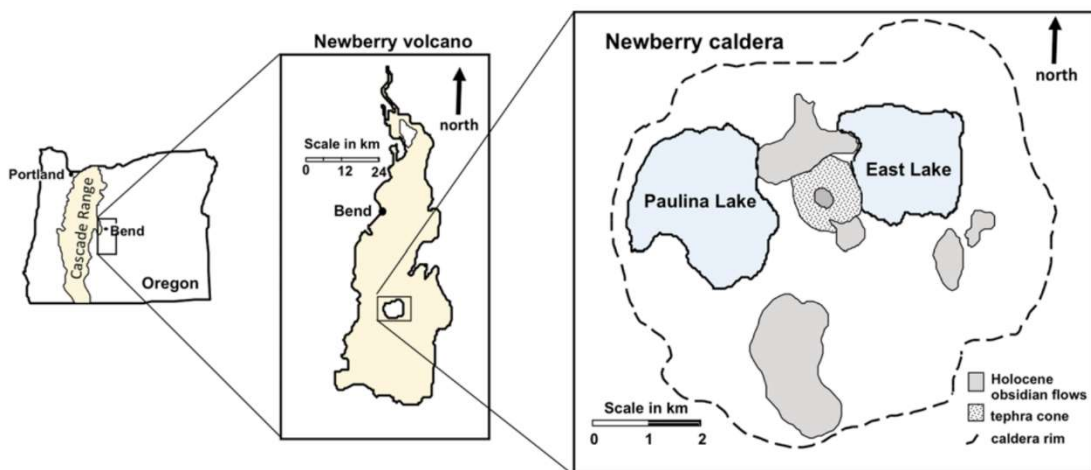
Figure 2.1. Location of Newberry Volcano and its twin crater lakes, East Lake and Paulina Lake (Lefkowitz et al., 2016). Newberry is not a part of the Cascade Volcano range.

19

Surface geology (Figure 2.2) at Newberry includes sequences of pyroclastic flows, alluvial deposits, mafic lava domes and flows, and silicic lava domes and flows (MacLeod and Sherrod, 1988).
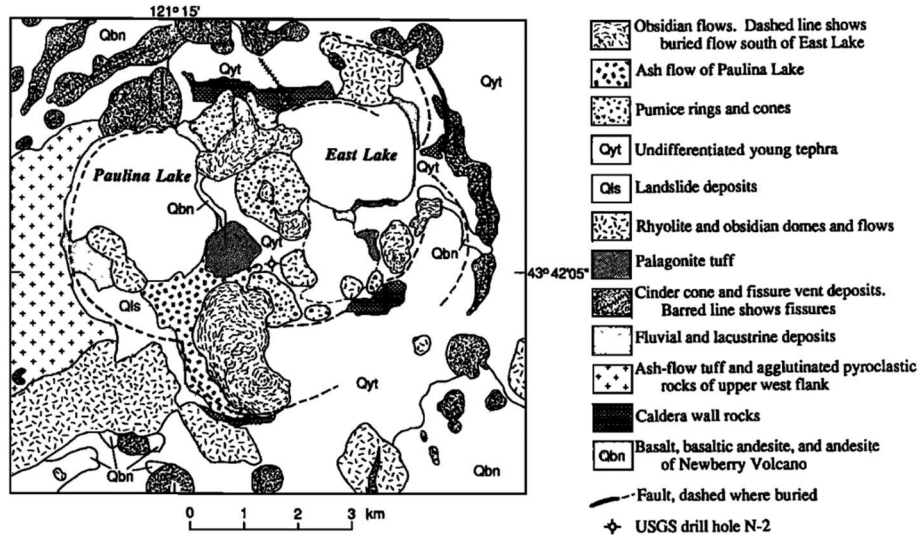
Figure 2.2. Geologic map of Newberry caldera (MacLeod and Sherrod, 1988)

Newberry is an intracontinental plume volcano – a manifestation of buoyant, upwelling mantle material (Hards, 2005). The volcano sits in an extensional tectonic regime and is marked by normal faults of Quaternary and Pliocene age (MacLeod and Sherrod, 1988). Repeated eruptions over 0.5 Ma are an indication that magma bodies have emptied and continually reformed beneath the surface. The combination of the regional fault system and repeated magmatic intrusions has led to a "thermal chimney" that continues to focus the ascent of new magma (MacLeod and Sherrod, 1988).

The same magma associated with basaltic fissure eruptions around the caldera likely has heated the silicic magma chamber from below, slowing crystallization of the melt and triggering rhyolitic eruptions. Changes in regional stress are also likely initiators of an eruption (MacLeod and Sherrod, 1988).

2.2 East Lake and Paulina Lake

The twin crater lakes in the Newberry caldera represent two end members of the volcanic lakes spectrum: East Lake with a CO_2 bubble input and Paulina Lake with subaqueous carbonate-rich hydrothermal springs (Lefkowitz et al., 2016). The lakes sit adjacent to each other within the caldera, separated by a volcanic ridge and tuff cone just 2 km wide.

East Lake sits at a surface elevation of 1945 m above mean sea level, with a surface area of 4.2 km^2 and a volume of 86 x 10^6 m^3 with an average depth of 20 m (Figure 2.3; Lefkowitz et al., 2016). The north side of the lake holds a drowned crater with a maximum depth of 55 m. In the southeast corner of the lake there is a pit with a depth of 12 m, and a hot spring beach serving as a popular destination for visitors to the lake.

East Lake is characterized by the ebullition of CO_2, H_2S, and Hg with a pH of 6-7, while Paulina Lake is characterized by high carbonate and As content with a pH greater than 8 (Varekamp et al., 2016).
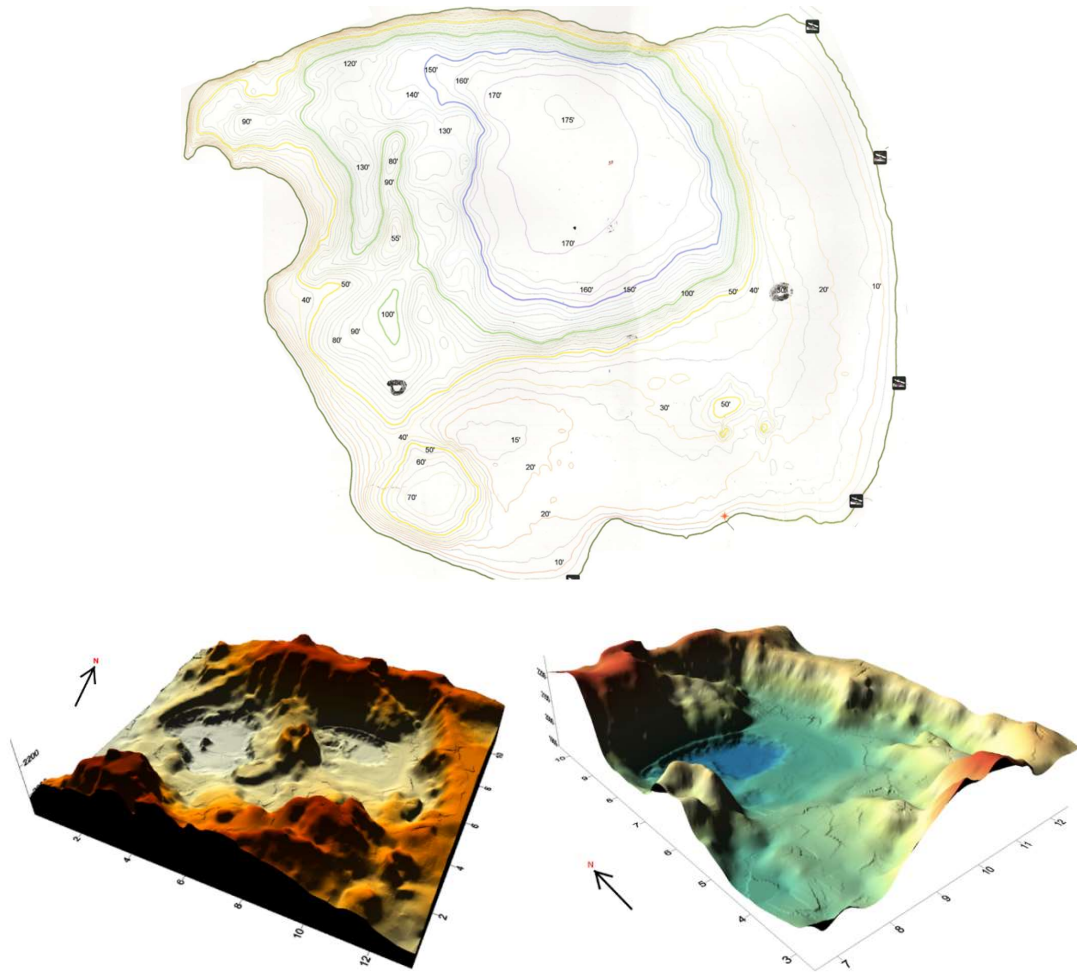
Figure 2.3. Bathymetry of Newberry caldera (*bottom left*) and of East Lake with caldera walls (*bottom right*). Altitude is in meters, and distance is in kilometers. Generated in SURFER by Foster, 2017.

2.3 Previous Work at Newberry

Several Wesleyan undergrad theses in recent years have focused on the Newberry crater lakes. Students collected samples and data in the summers (June, July, or August) of 2009-2012 and 2014-2016. Data contributions to this research have been collected over the last seven years, beginning in 2011.

Lefkowitz (2012) and Lefkowitz et al. (2016) produced an examination of both East Lake and Paulina Lake summarizing their history and identifying the persistent differences between the two. These studies used the geochemistry of the volcano's surface expression, the lakes, to get a "snapshot" of the hydrothermal system below.

Other Wesleyan researchers started to quantify the CO_2 flux from the two lakes and have determined the isotopic composition of the escaping gas (^{13}C and ^{18}O in CO_2) and developed simple carbon cycle models to explain the induced isotopic gradients in the lake water. Brumberg (2017) examined the carbon dynamics of both East Lake and Paulina Lake, and Capece (2016) did the same for East Lake specifically. They made the observation that degassed CO_2 in EL has isotope values that are far from predicted theoretical equilibrium values. One hypothesis to explain this is that the volcanic CO_2 bubbles that rise from the EL bottom do not fully dissolve during their travels upwards, and that remnant 'micro-bubbles' of volcanic CO_2 are part of the escaping CO_2 flux. That CO_2 gas would have a different isotopic composition than the diffusively emitted CO_2 from EL surface water. These works launched the investigation of CO_2 flux continued in this study.

Chapter 3: Methods

3.1 Field Methods

Field data and samples were collected in August and September 2017 and May and August 2018 (Figures 3.1, 3.2).

3.1.1 Field measurements of lake surface CO_2 fluxes

The lake's CO_2 flux was determined by the floating chamber method with a WEST flux analysis system (Chiodid et al., 1998, Mazot and Bernard, 2015). The floating flux chamber (filled with ambient air) was deployed on the water and gas accumulating in the chamber was continuously pumped through an anhydrone water trap ($Mg(ClO_4)_2$) into a LICOR CO_2 analyzer (LI-6252) which analyzes CO_2 based on infrared absorption spectroscopy. The pump rate was set at 1.5 L/min and CO_2 built in the chamber. The increase in CO_2 over time is proportional to the CO_2 flux from the lake.

The LICOR, pump, laptop and power supply were mounted on an instrument panel secured in a small flat bottomed boat (the HULC, Figure 3.2) powered by an electric trolling motor. Sampling locations were recorded with a Garmin xTrex 20x handheld GPS. At each site, the chamber was deployed for at least 100 seconds with measurements taken every 3 seconds. A linear best-fit line applied to these data (Figure 3.3) gave a volumetric flux rate for the area covered by the chamber, which could be converted to molar concentration (mol m^{-2} day^{-2}) with the K factor
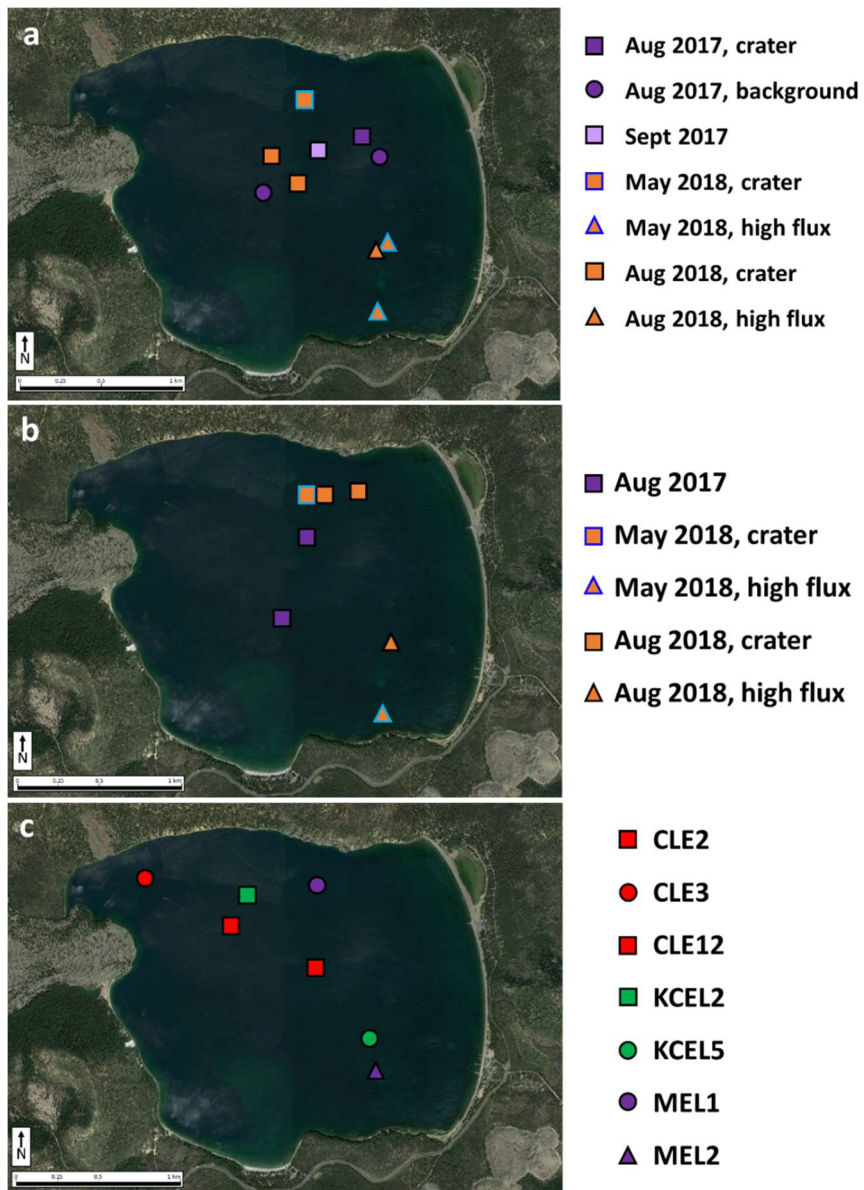
Figure 3.1. Field maps of (a) physical parameter measurements, (b) mercury sample collection taken in 2017-2018. (c) sediment cores taken in 2011-2018. Samples and measurements from 2011 are in red, 2015 in green, 2017 in purple, and 2018 in orange. Blue outlines represent May data. High flux locations are marked with triangles, drowned crater with squares, and background with circles.

$$K = \frac{86400 \cdot P}{10^6 \cdot R \cdot T_k} \cdot \frac{V}{A}$$
(Eq 3.1)

where P is the barometric pressure in bar, R is the gas constant 0.0831 bar L K^{-1}

mol^{-1}, T_k is the air temperature in °C, V is the volume of the chamber in L, and A is

the chamber surface area in m^2. P and T were recorded by the LICOR for each

location, and for this chamber V is 11.231 L, and A is $6.697 * 10^{-2}$ m^2.

In 2017, measurement locations followed a path from the east side of the lake

at the East Lake Resort, around in a loop, and back. In May and August 2018, the

GPS was used to ensure measurements were taken in a grid-like pattern with about

0.2 miles between measurements to ensure full coverage of the lake.

Fluctuation in the daily lake conditions contributes to the potential

complications relating to this method. High winds make it difficult to maintain a

precise location for the duration of the time required to take one measurement. Such

choppy water conditions allow for undesirable gas exchange if the seal between the

water and float chamber is broken. Calculation of K values is done with temperature

readings from the LICOR and not the water. Therefore, this method assumes surface

waters are in thermal equilibrium with the air above. In areas where discrete bubbles

do reach the surface, this portion of the flux is only included if they reach the area

under the float chamber. The seemingly random location of bubble trains is cause for

imprecision.
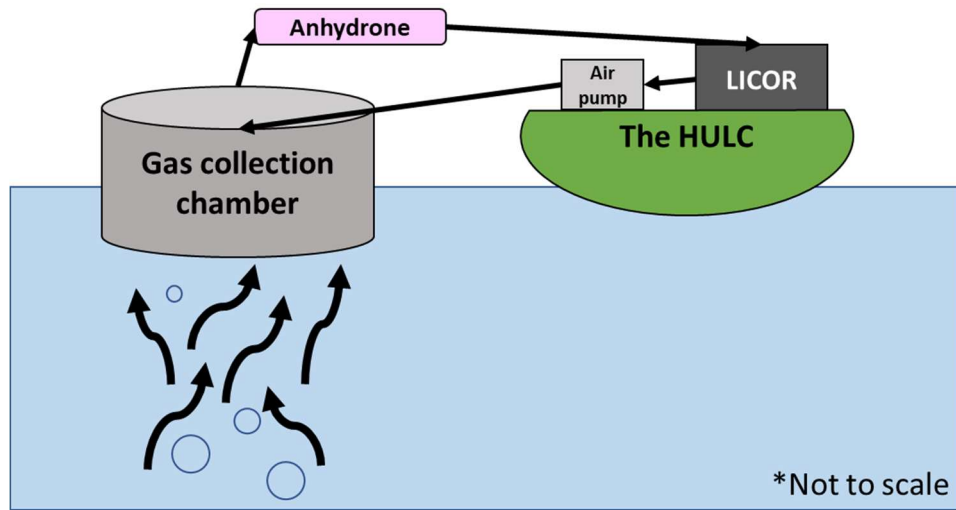
Figure 3.2. *Top:* Diagram of the HULC and CO_2 flux monitoring set-up. CO_2 flux reaches the surface as both discrete bubbles and diffusive flux. *Bottom:* Gas from the float chamber passes through anhydrone before LICOR measurement occurs. Air is then returned to the float chamber to measure CO_2 accumulation over time.

3.1.2 Water Profile In-Situ Measurements

The pH, dissolved oxygen (DO), conductivity and temperature were measured at 1-meter intervals using a YSI multiprobe (YSI Pro 2030) with a 30 m long cable. Prior to fieldwork, the probe was calibrated for temperature, pH, and DO with saturation at room temperature. The DO measurements were recalibrated for the elevation at Newberry, with $P_{atm} \sim 0.8$ bar.

The conductivity is the temperature compensated conductivity, C_{25}. Additional measurements were made at 1-foot intervals with an older YSI (3000 T-L-C YSI

27

Meter) with a longer cable (45 m). This probe yields temperature, raw conductivity, and C_{25}.
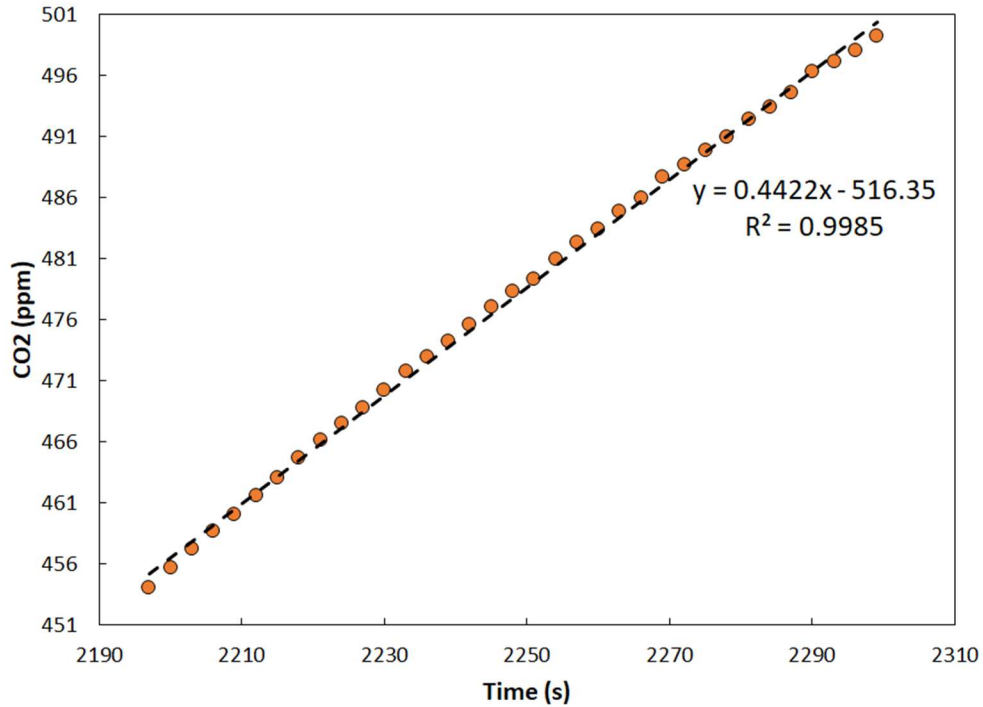
Figure 3.2. Sample plot of CO_2 accumulation at collection point MCEL26. CO_2 concentration readings were taken every 3 seconds for 102 seconds. The concentration changed by 45.2 ppm in this time, or 0.4430 ppm s^{-1}. A linear best-fit line applied to the data shows a change of 0.4422 ppm s^{-1}. At a temperature of 309.815 K and pressure of 786.844 HPa, the K factor is 0.4426, which gives a flux of 0.1957 mol m^{-2} day^{-1} at this point.

3.1.3 Water Sample Collection

Water profile samples were taken with a Teflon Van Dorn bottle every 10 meters. In shallow parts of the lake, samples were taken at 0, 2.5, and 5 m depths. All water samples were filtered in the field with 0.2 μm nylon syringe filters and stored in 250 mL HDPE bottles with no dilution. Glass crimp cap serum vials (50 mL) with zero headspace were used for samples for alkalinity titrations in the lab. Exetainer

vials were filled with filtered lake water for $\delta^{13}C$ (DIC) analyses. Two-mL serum cap glass bottles were filled with water for $\delta^{18}O$-δD analyses.

A separate suite of samples was collected for later Hg analyses, according to BASL Standard Operating Procedure TS-IOG-006 (Water Sampling for Mercury and Methyl Mercury Analysis). One set of samples for Hg was filtered with ultra-clean acid-washed 0.45 µm filter towers in the field. These samples were stored in 125 mL or 250 mL ultra-clean amber glass bottles and preserved to 0.2% or 0.4% trace-grade HCl for total dissolved Hg and dissolved methyl Hg analyses, respectively. The second set of unfiltered samples was collected in ultraclean bottles at each site and preserved to 0.2% trace-grade HCl for total Hg and total methyl Hg analyses.

3.1.4 Water Column Organisms and Particles

A tower of cylindrical filters with 100 µm and 20 µm openings was trailed behind the pontoon boat throughout a day of water sampling. The material collected was scraped off the filters back at Wesleyan for analysis.

3.1.5 Sediment Collection

Two sediment cores were collected in August 2018. Core MEL1 is 81 cm long and was collected from the drowned crater area of the lake where the water is 55 meters deep. core MEL2 is 142 cm long was collected from the pit area of the lake where the water is 12 meters deep. Cores were collected with a piston coring device from a stationary drilling platform with a tripod. The cores were retrieved, extruded,

and separated into 2 cm slices in the field, except the top 10 cm of MEL2 which was separated into 1 cm slices, and stored in 4 oz plastic cups for transport.

3.2 Sample Analysis

3.2.1 Carbon Dioxide Flux

Flux data for CO_2 was compiled and converted to a "heat map" for the lake area using a Sequential Gaussian Simulation (SGS) after Mazot and Bernard (2015). For each of the five field expeditions, the measured points (40-87 points each time) and their coordinates were subjected to inverse weighting interpolation to create thousands of synthetic data points. Hundreds of simulations were run with a random distribution of simulated points, and the average of these was taken. A separate map was also created as an average summer representation using all June and August data from 2015 to 2018.

There are some doubts as to the validity of this method due to the bimodal nature of lake degassing, which could lead to an error of 5-10 tonnes CO_2 per day. However, this correction is outside the scope of the current study.

3.2.2 Alkalinity and pH of water

The water alkalinity and pH were determined through titration on a Mettler DL12 auto-titrator at Wesleyan University. The titration is performed with additions of 0.1 N HCl until a pH of 4.320 is reached. Thirteen samples were measured from 2017 and 16 from 2018. A solution of 2.02 meq/L made from an Aqua Solutions, Inc.

was used as a standard. Accuracy was within 3%. Total CO_2 and pCO_2 were

calculated by the CO2Sys excel program developed by Woods Hole Oceanographic

Institution (Pierrot et al., 2006). The program is set to use constants for *Salinity = 0*

(freshwater); K_1, K_2 values from Millero, 1979 with pH on *NBS scale (mol kg^{-1} H_2O).*

Field temperature and pH data are input with laboratory alkalinity.

3.2.3 Anions and Cations in water

   Anion content of water was determined on a Dionex 500 series Ion

chromatograph (IC) with an ED50 Electrochemical Detector at Wesleyan University.

Samples from 2017 were evaluated for chloride (Cl^-) and sulfate (SO_4^{2-}). Samples

from 2018 showed evidence of calcium carbonate precipitate in the IC column as a

result of mixing with the high pH eluent and were therefore spiked with HCl for

evaluation of sulfate only. Ten samples collected in 2017 and 17 collected in 2018

were measured. Standards used were 0, 1, 2, 10, 30, and 70 ppm. Accuracy was

within 3%.

   Major cation content (Ca^{2+}, Mg^{2+}, Na^+, K^+, Si^{4+}) of water was determined at

Smith College in Northampton, MA by Inductively Coupled Plasma-Optical

Emission Spectroscopy (Teledyne Leeman Labs instrument). Fifteen samples

collected in 2017 and 17 samples collected in 2018 were measured. Standards used

were 5, 10, 20, 30, 50, and 100 ppm made from 1000 ppm stock solutions diluted

with double distilled water. Additional multielement and Accutrace standards with

25, 10, and 5 ppm were also used as checks. Accuracy was within 10%, except the lowest-concentration standards which were within 15%.

3.2.4 Mercury in water

Total and dissolved Hg in water samples was determined on a Tekran 2600 Total Mercury Analyzer by Oxidation, Purge and Trap, and Cold Vapor Atomic Fluorescence Spectrometry, modified after US EPA Total Mercury/ Dissolved Total Mercury Method 1631.E. Methyl Hg in water was determined with a Tekran 2750 Methyl Mercury Distillation System, Tekran 2700 Methyl Mercury Analyzer, and Perkin Elmer DRC-e ICP-MS using aqueous phase ethylation, Gas Chromatography separation and Cold Vapor Atomic Fluorescence, modified after US EPA Methyl Mercury Method 163.0.

Reported values of total Hg, total dissolved Hg, total methylated Hg, and dissolved methylated Hg were converted to more restricted groupings according to the following calculations:

$$Particulate\ MeHg\ =\ Total\ MeHg - Dissolved\ MeHg$$
$$Dissolved\ Inorganic\ Hg = Dissolved\ Hg - Dissolved\ MeHg$$
$$Particulate\ Inorganic\ Hg = Total\ Hg - Dissolved\ Hg - Particulate\ MeHg$$

with Dissolved MeHg taken as measured.

Water for Hg^0 was collected in clean amber glass bottles and tested at University of Connecticut. Samples were transferred with minimal disturbance to

sparging containers, had their headspace purged the for several minutes, and then

purged with a gold trap in-line for 10 min at ~0.5 L N_2 min^{-1}.

3.2.5 Physical Characteristics of Sediments

The average weight of the 4-oz cups was subtracted from weight

measurements to obtain the weight of the sediment only. The 2-cm slices of core

collected in the field were brought back to Wesleyan and weighed ("wet weight").

The cups were then left open and untouched for two weeks so the sediments could

completely dry in ambient room air and were then weighed again ("dry weight").

These dry sediments could then be used for all following compositional analyses.

Water fraction, WF, was then calculated as:

$$WF = \frac{wet\ weight - dry\ weight}{wet\ weight} \qquad\qquad \text{(Eq. 3.2)}$$

The volume fraction dry rock, or volume of rock (V_r) per total volume (V_{tot}), was then

calculated after Varekamp (unpublished data) as

$$\frac{V_r}{V_{tot}} = 1 - \frac{WF \times d_r}{1 + WF(d_r - 1)} = \frac{WF - 1}{WF - 1 - (WF \times d_r)} \qquad\qquad \text{(Eq. 3.3)}$$

where d_r is the grain density, taken here as a typical organic-rich sediment value of

1.93 g/cm^3. Bulk dry density (BDD) accounts for pore space previously occupied by

water and was calculated as

$$BDD = V_r(d_r) \qquad\qquad \text{(Eq 3.4)}$$

3.2.6 Tephrochronology and Pb-210 age of sediment

The time scale of sedimentation (linear sedimentation rate) for East Lake

sediments was determined by two methods. First, by tephrochronology identifying

ash at the bottom of core MEL2 as the known 1240 BP Paulina Lake Ash Flow

(PLAF).

As an alternate check, Pb-210 was measured in the top 16 cm of core MEL2

down to where no more unsupported Pb was present. ^{238}U decays according to the

following scheme:

$$^{238}U \ ... \ ^{226}Ra \rightarrow \ ^{222}Rn \rightarrow \ ^{210}Pb$$
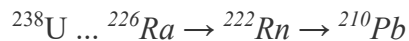
with a number of intermediates between ^{238}U and ^{226}Ra and some short-lived

intermediate nuclides between ^{226}Ra and ^{210}Pb. Crustal escape of the noble gas ^{222}Rn

leads to an atmospheric reservoir which decays to ^{210}Pb with a $T_{1/2}$ of 3.8 days. This

leads to an atmospheric depositional flux of ^{210}Pb that is "unsupported" by

grandmother ^{226} Ra. The presence of ^{226}Ra in the sediment leads to a fraction of

"supported" ^{210}Pb, which is subtracted from the total amount of ^{210}Pb analyzed. The

unsupported ^{210}Pb ("excess," ^{210}Pb*) acts as a buried clock, where buried sediment no

longer receives atmospheric deposition and starts to decay. Application of the

common decay equation shows that a log linear plot of depth versus ^{210}Pb* should be

a straight line with the initial amount of ^{210}Pb* in the top sample. Ages in years

before the core was taken are obtained from the common exponential decay equation

$$N_t = N_0 e^{-t\lambda} \hspace{3cm} \text{(Eq 3.5)}$$

and subsequently converted to calendar years (Faure, 1998).

Sediment samples were left to sit capped for one week for ^{210}Bi to propagate, then placed in a Gamma Ray Counter at Yale University in New Haven, CT to measure ^{210}Bi $\rightarrow$ ^{210}Po decays for two days. Total ^{210}Pb and ^{226}Ra were determined. From ^{210}Pb*, an equation was derived to find the ^{210}Pb content of the most recently deposited material (upper 1 cm) according to the Constant Initial Concentration method (Gee, 1986). With this, years since deposition of each slice could be calculated along with an average yearly deposition rate.

3.2.7 Major and Traces elements in sediment

Carbon, Nitrogen, and Sulfur contents of core sediments were measured on a Flash 1112 Series Elemental Analyzer (EA). The finely-ground sediments in 10-15 mg aliquots were wrapped in tin capsules. One to two samples in each run was measured in triplicate to check precision. L-cysteine and aspartic acid were used as standards for C and N analysis. Sulphanilamide was used as a standard for S analysis.

Major and minor elements were determined at SGS labs by fusion by Na_2O_2 sintering, followed by dissolution of the obtained glass in strong acids, dilution, analyses on a multicollector ICP-MS. A series of canadian national SRMs was used for accuracy and shows values well within 5%.

Two core slices were analyzed by energy dispersive spectroscopy (EDS) on a Hitachi SU5000 Field Emission SEM at Wesleyan University to determine elemental composition of electron-dense grains.

3.2.8 Mercury in sediment

Bulk Hg concentrations were measured in all 2017 core slices in a total of 118 samples. Mercury content of core sediment was determined on a DMA-80 Direct Mercury Analyzer at Wesleyan University. Sediments were ground to a "baby-powder fine" texture and placed in individual nickel boats in the instrument. The Hg was released from the samples by pyrolysis and detected by atomic absorption spectroscopy. Formal laboratory standards used were SRM TH2 (620 ppb Hg) and Pacs 2 (3040 ppb Hg), and an in-house standard Bulk2 (340 ppb Hg). Blanks were run before each standard to check for carryover from the previous sample. Maximum carryover values were 22 ng and did scale up with Hg concentration of the sample run immediately before. Accuracy was within 15%.

Chapter 4: Results

4.1 East Lake Gas Emissions

Carbon Dioxide flux measurements from East Lake surface were taken as part of this study in August 2017, May 2018, and August 2018 (Figure 4.1, Table 4.1). Data from two earlier studies (June 2015 from Capece 2016, June 2016 from Brumberg 2017) are incorporated here as well. In June 2015, the lake released an average of 0.25 mol m^{-2} day^{-1}, for 45 tonnes CO_2 per day over the whole lake surface area. Of this area, 9.3% released more than 0.5 mol m^{-2} day^{-1} with greatest emissions concentrated in the north, bordered by steep cliffs that reach the deepest part of the lake, and in the west. No part of the lake surface showed CO_2 emissions over 1.0 mol m^{-2} day^{-1}.
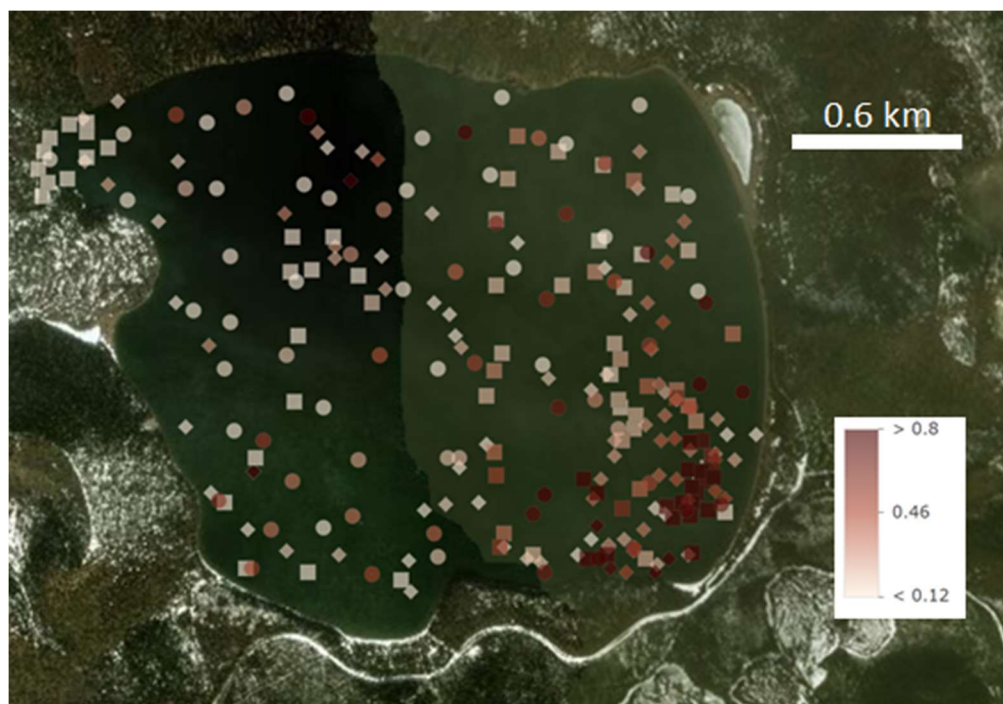
Figure 4.1. Individual CO_2 flux measurements taken as part of this study in 2018 (circles) and 2017 (squares), with those from previous years (diamonds). Created on arcgis online.

In June 2016, the lake released an average of 0.28 mol m^{-2} day^{-1}, for 51 tonnes CO_2 per day over the whole lake. The areas of greatest flux, emitting over 0.5 mol m^{-2} day^{-1}, were in the north and southeast sections of the lake and comprised 7.7% of the total lake surface.

In August 2017, the lake released an average of 0.26 mol m^{-2} day^{-1}, for 47 tonnes CO_2 per day over the whole lake. The north area with elevated emissions is less apparent but the southeast area of the lake with emissions over 0.5 mol m^{-2} day^{-1} increased from the previous year to cover 10.0% of the lake surface.

Measurements of CO_2 flux in May 2018 were taken three weeks after melting of the winter ice cover. The lake released an average of 0.51 mol m^{-2} day^{-1} for 95 tonnes CO_2 per day over the whole lake surface. More than half the lake (51.6%) was emitting more than 0.5 mol m^{-2} day^{-1}, with elevated values across the whole east half of the lake and in the north area near the steep cliffs.

In August 2018, the lake released an average of 0.20 mol m^{-2} day^{-1}, for 37 tonnes CO_2 per day over the whole lake. The high flux southeast area of the lake with emissions over 0.5 mol m^{-2} day^{-1} now covered 14% of the lake surface, with no other apparent high-flux zones. Macroscopic bubbles were visible at the lake surface in the high flux area when it was calm and undisturbed.

Datasets from each individual field expedition were run through an SGS program to create intensity maps of CO_2 flux across the lake at different times of the year (Figure 4.2). One map was also created with all the summer (June-August) data

together. With the thousands of points created by the SGS program, a mean flux in

mol m^{-2} day^{-1} could be calculated for each time of year as well as a daily whole-lake

CO_2 flux for the 4.2 km^2 lake. The southeast "high-flux zone" of the lake with

consistently greatest CO_2 flux values (>0.5 mol m^{-2} day^{-1}) covers 10% of the lake

surface area.
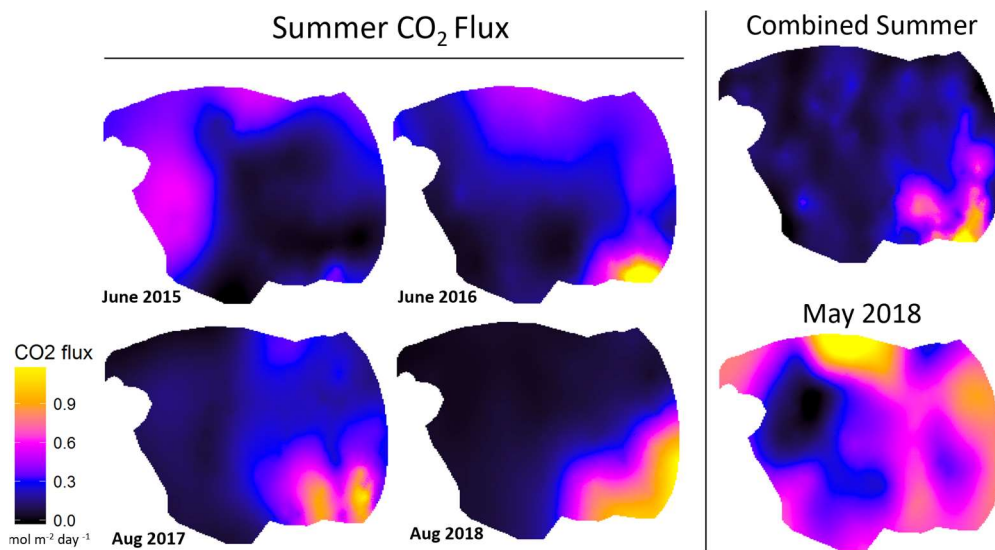
Figure 4.2. Maps created from Sequential Gaussian Simulations run in R with CO_2 flux measurements. Combined summer data uses all June-August datasets.

	Mean Flux via SGS (mol CO_2 m^{-2} day^{-1})	Whole-lake flux (Tonnes CO_2 day^{-1})
June 2015	0.244	45.0
June 2016	0.277	51.3
August 2017	0.258	47.6
May 2018	0.515	95.1
August 2018	0.203	37.6

Table 4.1. CO_2 flux estimates of East Lake for 2015-2018. May 2018 flux is about double that of June and August studies.

Ambient air was collected and measured for Hg with two different instruments and was found to be below detection (within the background noise) in both cases.

4.2 East Lake Water

East Lake is a dimictic lake overturning upon freezing around November and upon melting in May, and stratifying in between. The distinction between homogeneity in the water column in spring and stratification by late-summer is evident in the water's temperature, conductivity, dissolved oxygen, and pH.

4.2.1 Temperature

In August 2017 and 2018, the thermocline extended from 8 m depth to 18 m depth, representing a transition from 18-20°C at the surface to 4-6°C at depth (Figure 4.2). In May 2018, the thermocline was shallower and less pronounced. It extended from 5 m depth to 11 m depth representing a transition from 10-12°C at the surface to 4-6°C at depth. In September 2017, the thermocline extended from 10 m depth to 19 m depth representing a transition from 11-12°C at the surface to 3-4°C at depth. The full 2011 to 2018 data suggests that the thermocline shallows over the season or the epilimnion gets thinner from June to August/September.
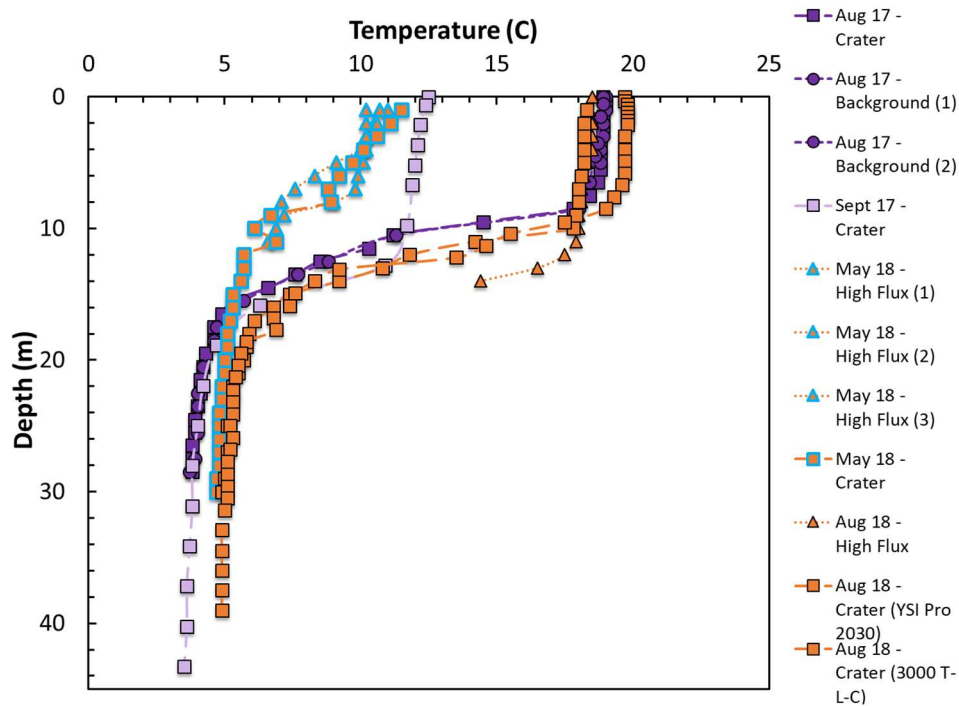
Figure 4.2. In-situ temperature profiles for 2017 and 2018. The thermocline is around 10 m depth and varies seasonally between 6 and 14 meters.

4.2.2 Conductivity

In May 2018, the temperature-compensated conductivity (TCC) throughout the water column was 347-350 µS/cm (Figure 4.3). In most profiles from August of 2017 and 2018, the epilimnion demonstrates similar values to those of May, but in the August profiles the TCC decreases to 340 µS/cm in the metalimnion then increases to up to 353 µS/cm down the hypolimnion. The profile taken in September 2017 and one taken in August 2018 were both measured with the 3000 T-L-C (others were taken with the YSI Pro 2030). They each follow a pattern similar to other August measurements with a consistent value through the epilimnion and an increase below the thermocline but in a different range.
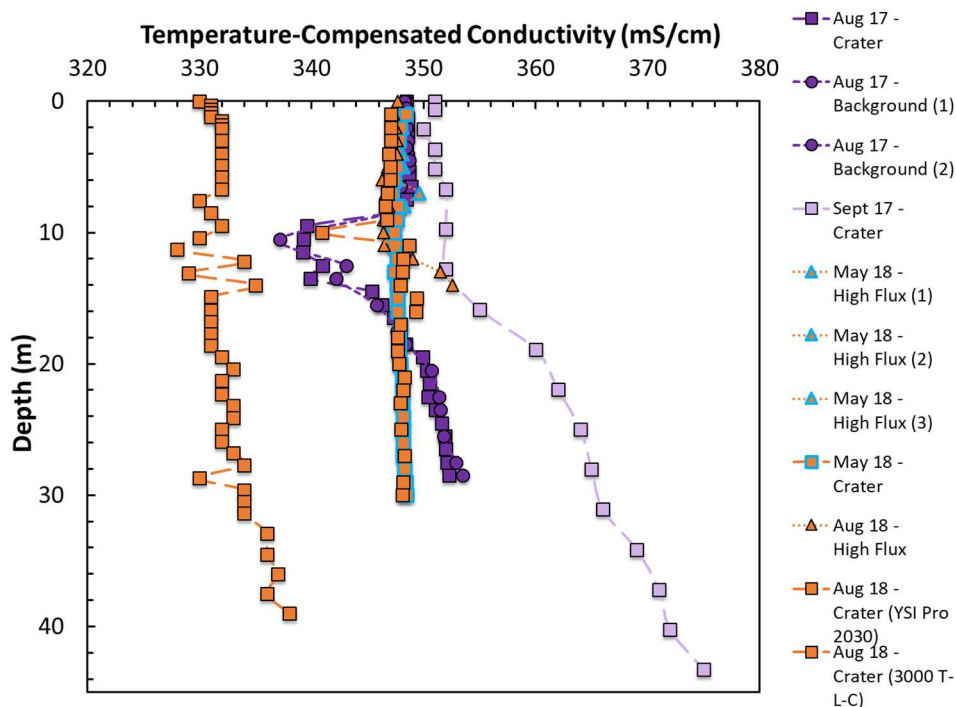
Figure 4.3. In-situ conductivity profiles (compensated for 25°C) for 2017 and 2018. The profile taken in September 2017 and one taken in August 2018 were taken with a different instrument than the others.

4.2.3 Dissolved Oxygen

Profiles from August 2017, September 2017, and August 2018 all show values of 8-10 mg/L dissolved oxygen (DO) above the thermocline, but increase to 12.1 mg/L DO (2017) or 14.6 mg/L DO (2018) just below the thermocline (Figure 4.4). Below this increase, the DO in the lake steadily drops until it reaches 2.6-3.4 mg/L below 20 m water depth (2017) or 7.1-7.5 mg/L below 25 m water depth (2018). In May 2018, DO levels throughout the water column were 7.6-9.0 mg/L.

When the raw data is compared to temperature-dependent oxygen solubility (Figure 4.5), it is clear the lake is more saturated in oxygen in August than in May, except in the deep parts of the hypolimnion. Profiles from May show that DO is

100% at the surface, steadily decreasing with depth to 80% at 30 m depth. Profiles from August, when stratification is fully developed, show surface water is over-saturated in DO (110-140%) with an increase to 150% at the top of the metalimnion and a steep decrease to 30% (2017) or 80% (2018) below the thermocline. Previous work by Lefkowitz et al. (2017) documents this phenomenon as an effect of photosynthesis at the temperature border.
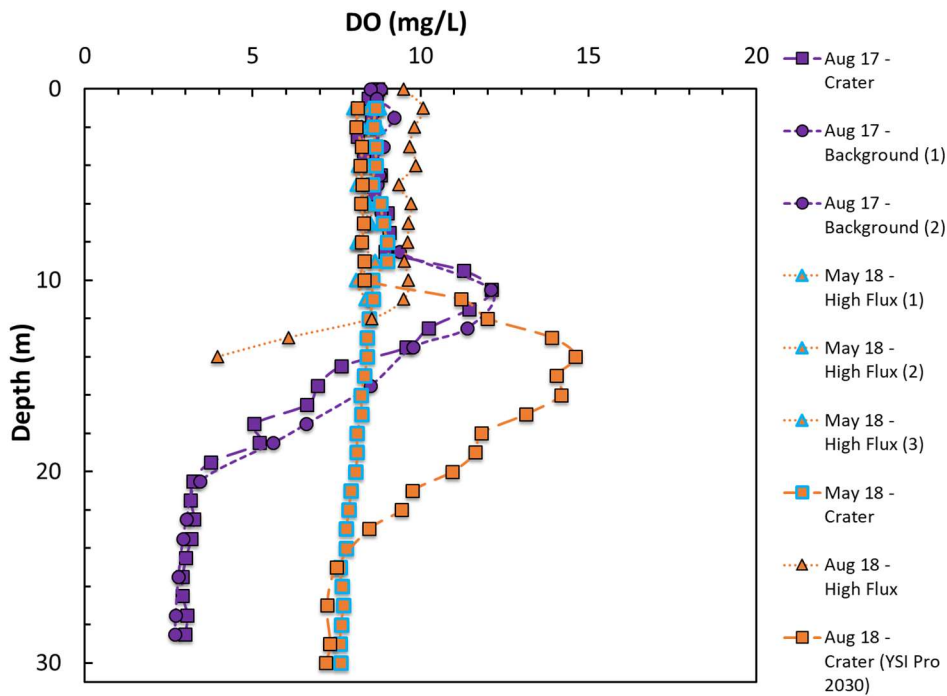
Figure 4.4. In-situ DO profiles for 2017 and 2018. The water column is homogenous in May, but stratified in August. Also in August, the water column shows an increase just below the thermocline.

4.2.4 Light penetration

A secchi disc was used to measure visible light penetration in August 2017 and August 2018 (Table 4.2). Visible light penetration was less than 3 m in August 2017 (when it was particularly smoky due to wildfires at that time, possibly causing

reduced light input). In August 2018, visible light penetration reached an average of 3.9 m.
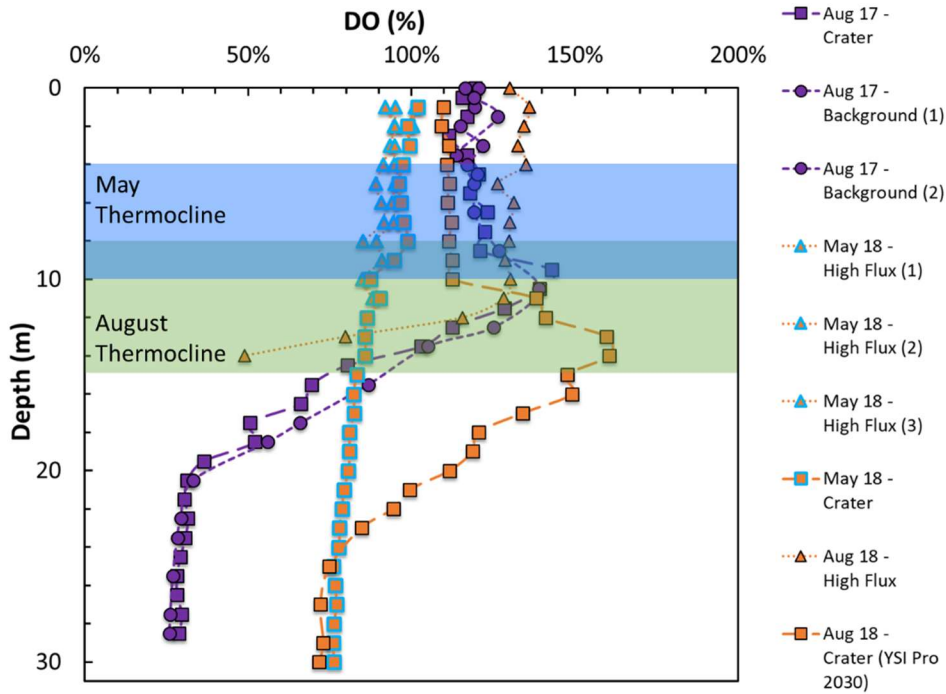
Figure 4.5. DO as a percent of temperature-dependent oxygen solubility at pressure of 600 mm Hg (USGS, 1999). There is almost no gradient developed in the water in May, but there is a strong one in August, as well as an increase in DO in the thermocline.

	Light penetration depth	Location
August 2017	2.75 m	CMPW4
August 2018	3.3 m, 4.1 m, 4.3 m	MCELW3

Table 4.2. Lake turbidity as observed on a Secchi Disc.

4.2.5 pH

In May 2018, the pH of the drowned crater area of East Lake was 7.4 above the thermocline and 7.1 below the thermocline, although this gradient is not strong

(Figure 4.6). Stratification is evident in August 2017 and 2018, when the pH of the crater and background areas of the lake are 7.4-8.0 above the thermocline and 6.4-6.9 below the thermocline. In the high flux area in May, there is large variation of pH with no depth trend.

It should be noted that this pH probe is temperature sensitive and the data are temperature compensated (pH_{25}). There is a change in pH as a result of shifting carbonate equilibria at the same bulk composition. In fluids with high internal pCO_2, samples may shift pH to higher values as a result of CO_2 degassing when brought to the surface.
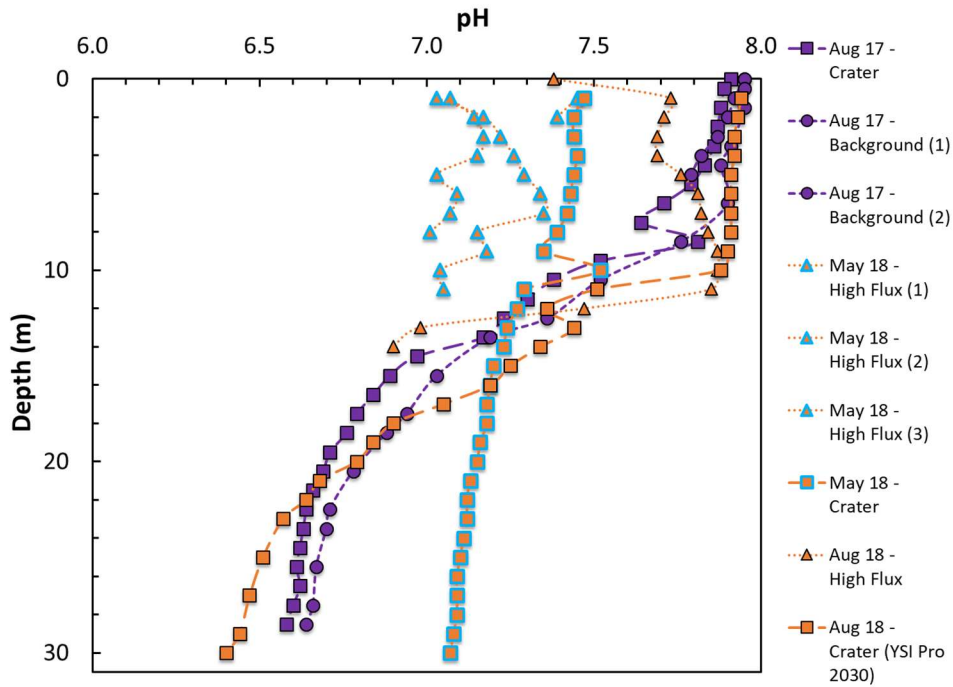
Figure 4.6. Field pH depth profiles for 2017-2018. The water column in May is homogenous around 7-7.5 pH. The water column in August is stratified and shows higher pH of 8 in surface water and lower pH of 6.5 at the lake bottom.

East Lake water contains 60-75 mg/L SO_4^{2-}, with no systematic changes in depth or over time (Figure 4.7). Concentrations of Cl^- in East Lake range from 0.5-1.0 mg/L. In 2011 and 2016, some elevated values were evident at 50 and 30 meter depth, respectively (Figure 4.7). Neither SO_4^{2-} nor Cl^- show concentration gradients between the surface and bottom waters.

Concentrations of K, Mg, Na, and Ca all show slight secular increases over the years this study has covered, with a gradual and constant increase of a few ppm between 2011 and 2018 (Figure 4.8). Neither K, Mg, nor Na show gradients between the top and bottom waters. One water profile collected in 2011 shows particularly high K and Cl at 50 m depth, but it is not relpicated in any other years. For Ca and Si, there is more secular variation in the epilimnion than for the hypolimnion.

In 2018, samples from previous years were re-run for major cations alongside the most recent set of samples such that comparisons between years could be made with the instrument running with the exact same specifications (Figure 4.9). When the average values for each element obtained from the re-runs are plotted over time, slight secular changes can be seen.

4.2.6 Alkalinity and CO_2

Alkalinity shows a slight secular increase between 2011 and 2018 (Figure 4.10). There is no consistent gradient between the top and bottom waters. Values range from 2.05 meq L^{-1} to 2.35 meq L^{-1}. The total variation is within 15%.
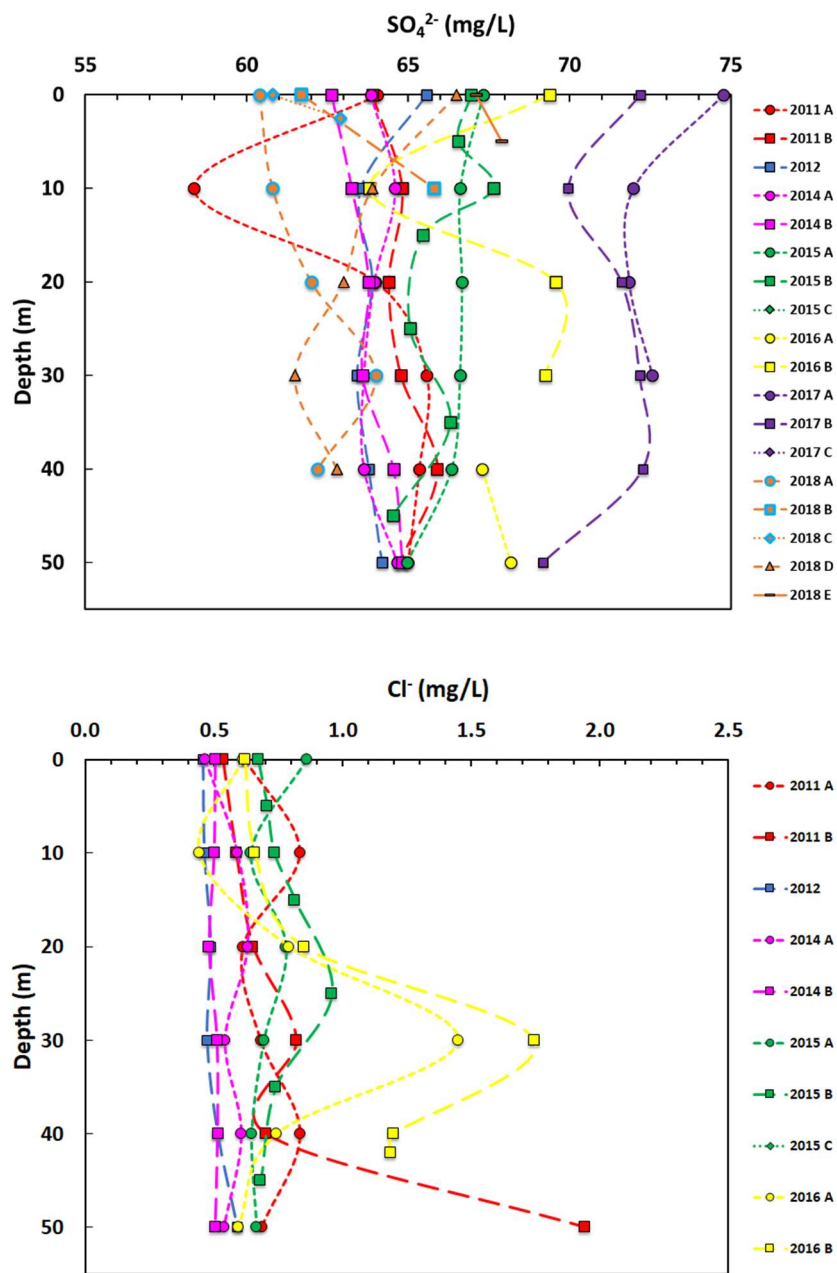
Figure 4.7. Anion concentrations in East Lake. Chloride peaks at 30 m depth in 2016 and 50 m depth in one profile from 2011.
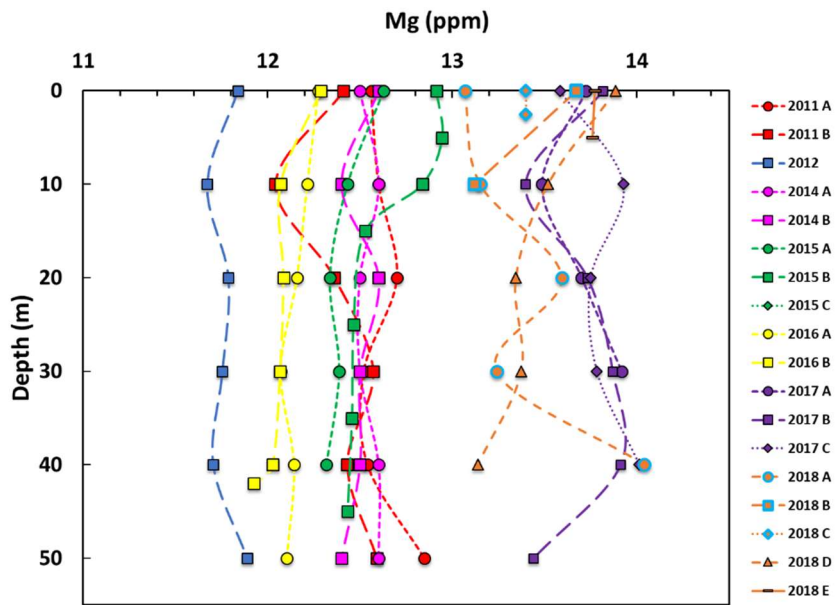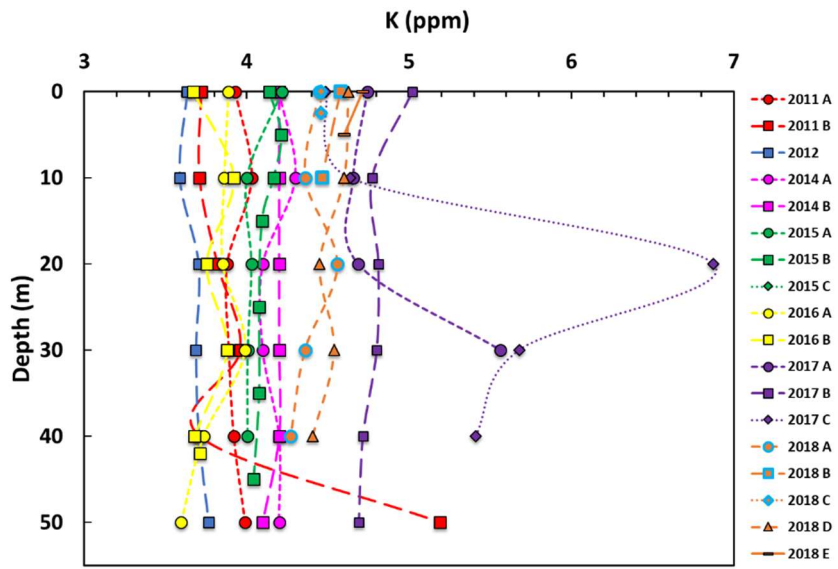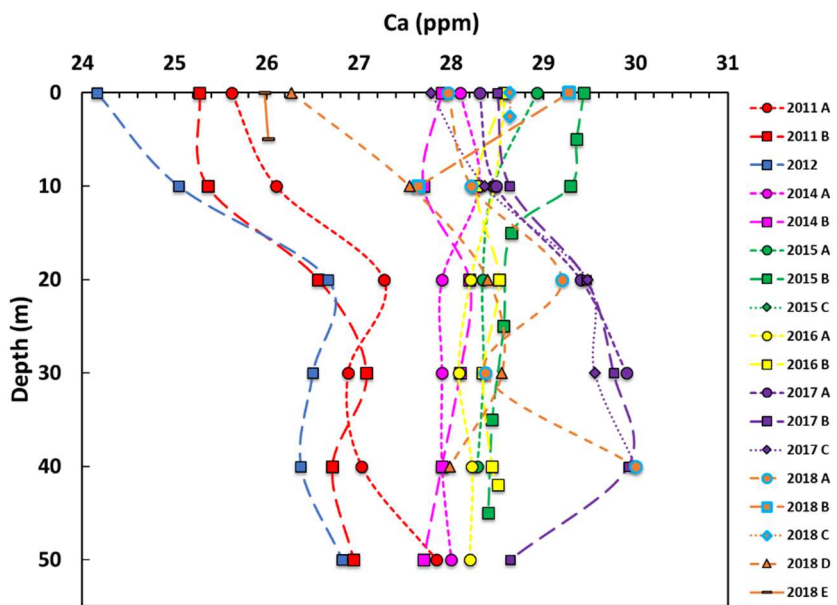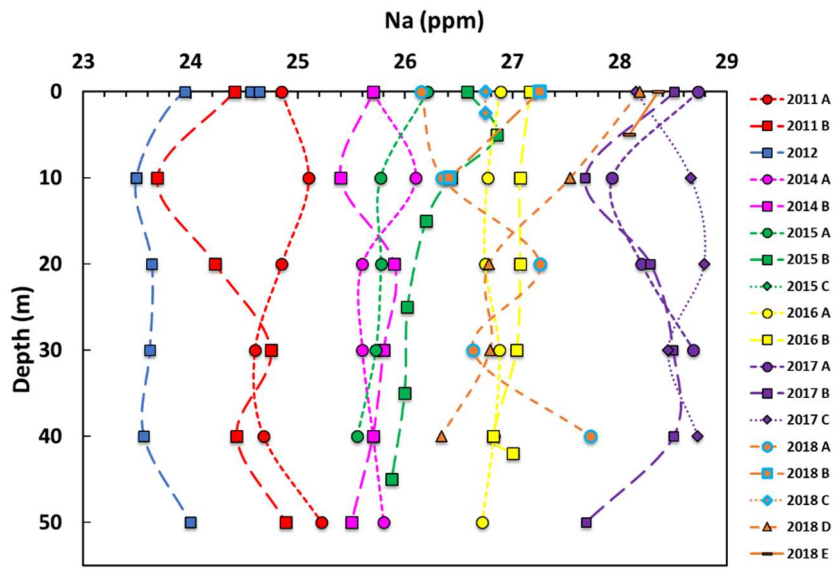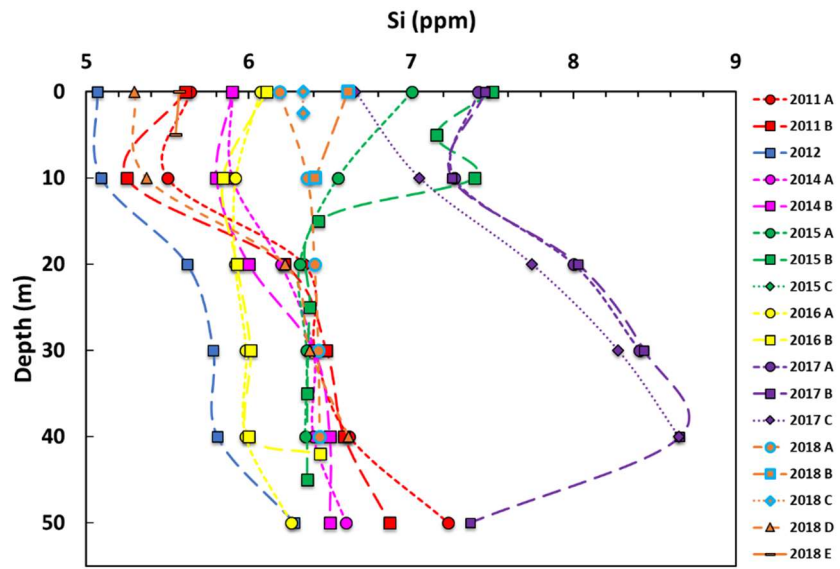
Figure 4.8. Cation concentrations in East Lake. The profiles do not appear to support any hydrothermal input to East Lake.
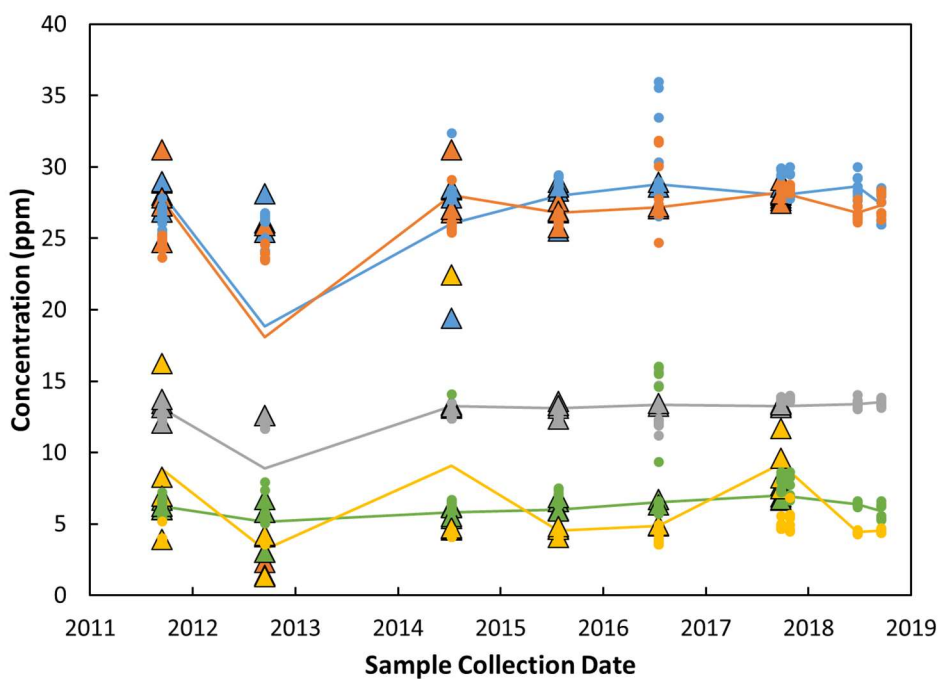
Figure 4.9. Replicate analyses (triangles) and original analyses run in the year of collection (circles). Lines connecting the average of the set of replicates from each year show the lake is in steady state. The cause for the decrease in 2012 is unknown as of this time. Ca is in blue, Na is in orange, Mg is in grey, Si is in green, and K is in yellow.

The program CO_2SYS was used to determine pCO_2 of the water at various depths using field temperature and pH, and alkalinity determined in lab (Figure 4.11). Partial pressure of CO_2 is larger in the deep waters than the surface year-round. The epilimnion shows larger pCO_2 in May than August, but the hypolimnion shoes larger pCO_2 in August than May. This gradient is larger in August as well.

Whole-lake ΣCO_2 also increases with depth, and once again there is a stronger gradient in August than in May, with greater hypolimnion values in August (Figure 12). Considering the volume of each depth slice of the lake (Brumberg, 2016), this gives an average whole-lake CO_2 load of 9.49×10^{11} mol CO_2 (Table 4.2).
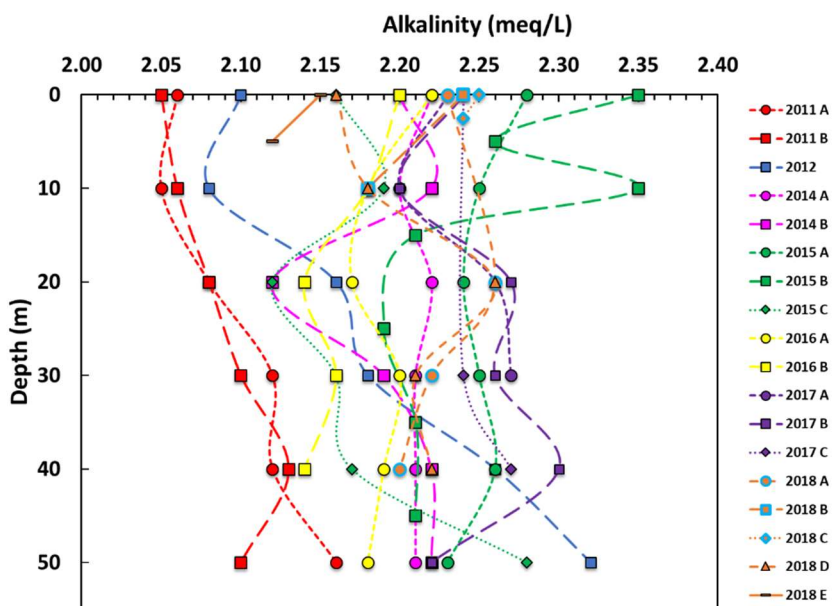
Figure 4.10. Alkalinity depth profiles for 2011-2018.
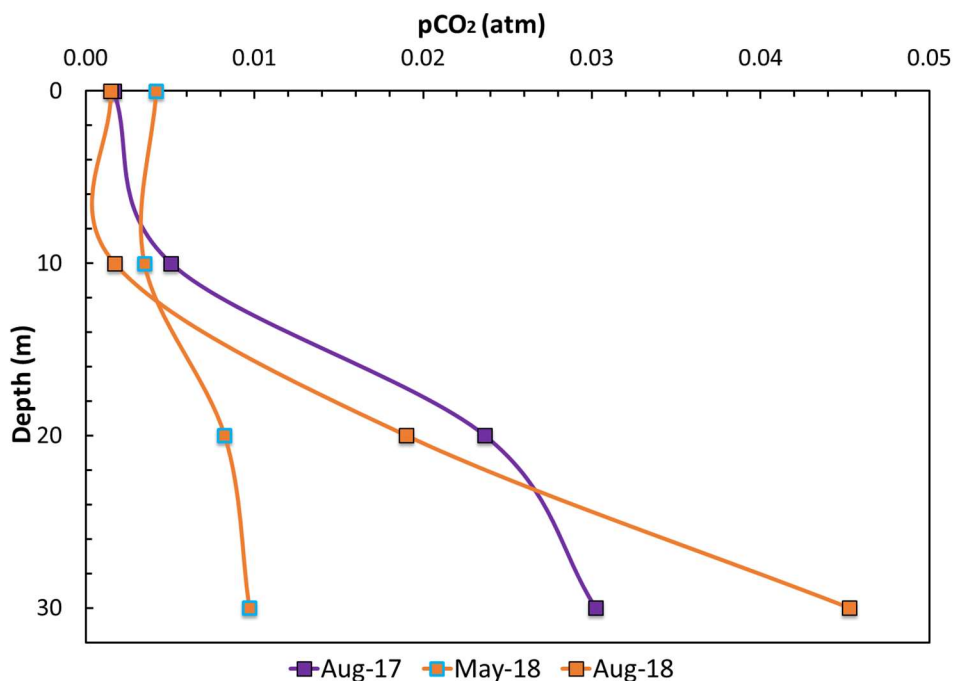
Figure 4.11. Calculated pCO_2 according to field temperature, field pH measurements, and lab alkalinity. Values determined using CO_2SYS program. In May, the water column was recently mixed due to turnover, and stratification is weak.
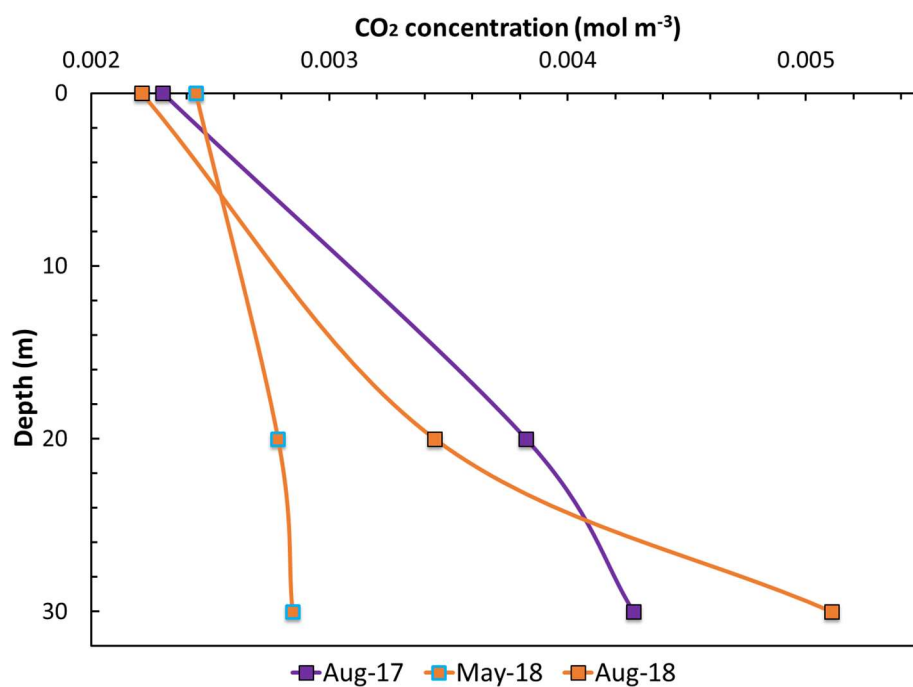
Figure 4.12. Calculated mol CO_2 per m^3 in East Lake, according to depth slices 0-12.2 m, 12.2-24.4 m, and 24.4 m-54.9 m.

	Aug 2017	May 2018	Aug 2018
Whole Lake	**4.89×10^5**	**3.79×10^5**	**5.06×10^5**

Table 4.3. Calculated bulk CO_2 in East Lake.

4.2.7 Mercury in water

Mercury in East Lake water can exist in particulate or dissolved form, and in both cases can be either inorganic or methylated. Total Hg (particulate and dissolved, inorganic and methylated) throughout much of the water column is 3-8 ng L^{-1}, reaching about 20 ng L^{-1} in the deepest part of the crater (Table 4.13). August 2017 values are generally higher than 2018 values for the drowned crater. The "high flux zone" (the same area with highest CO_2 flux) presents the highest total Hg surface

water values at 8 ng L^{-1}, as well as the highest total Hg bottom water values in the 100s of ng L^{-1}.
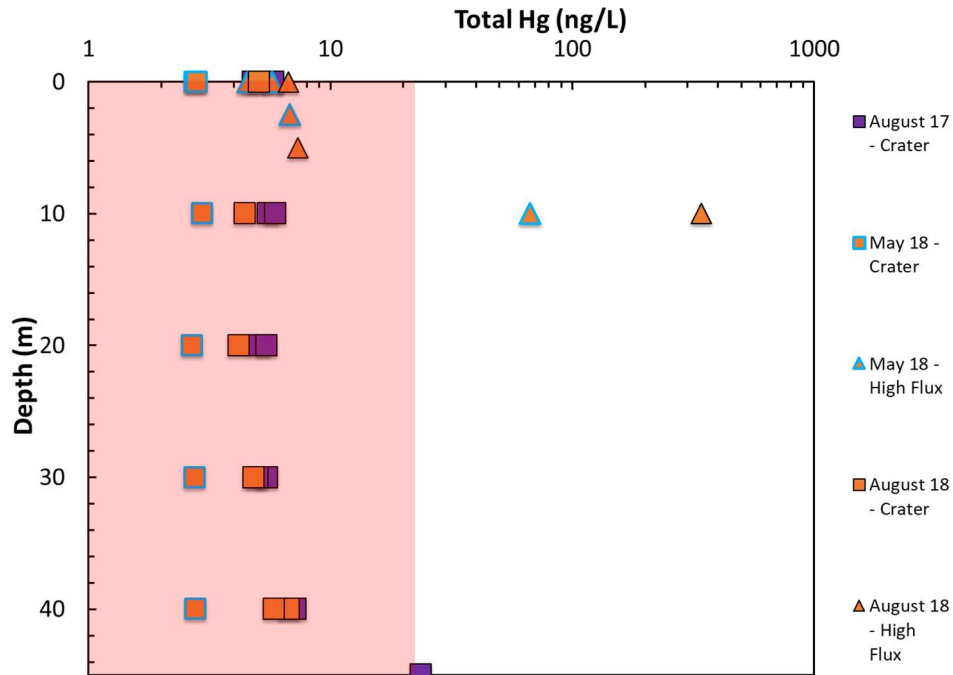
Figure 4.13. The sum of all particulate and dissolved Hg species. Red box indicates typical (non-volcanic) lake values (Morel et al., 1998). The x-axis is plotted on a log scale.

Forms of Hg are further broken down into 4 groups based on being methylated or inorganic, and particulate or dissolved (Tables 4.4, 4.5). Of the extreme Hg values at the bottom waters of the high-flux area, most of the 100s of ng L^{-1} are inorganic particulate Hg. Down the water column in the drowned crater area, and all surface waters, inorganic particulate Hg ranges from 1-5 ng L^{-1}. The deepest waters in the drowned crater carry 10 ng L^{-1} inorganic particulate Hg (Figure 4.14).

The same trends as total Hg hold true for dissolved inorganic Hg and methylated (both particulate and dissolved) Hg (Figures 4.15, 4.16). The high flux area still has the highest values, but here on the same order of magnitude as the rest of

54

the lake. Inorganic dissolved Hg ranges from 2-7 ng L^{-1}. Methylated particulate Hg ranges from 0-1.2 ng L^{-1} with the bottom waters of the drowned crater at 4 ng L^{-1}. Methylated dissolved Hg ranges from 0.2-1.5 ng L^{-1} with the bottom waters of the drowned crater at 3.8 ng L^{-1}. Dissolved Hg, in both the methylated and inorganic forms, is generally lower for August 2017 than for 2018 in the drowned crater area. For a given time of year, surface water Hg values are about the same for all parts of the lake – likely because the surface waters are continually homogenized by wind action. The dissolved MeHg fraction is up to 40% of total dissolved Hg, indicating that methylation is a very active process in this lake.
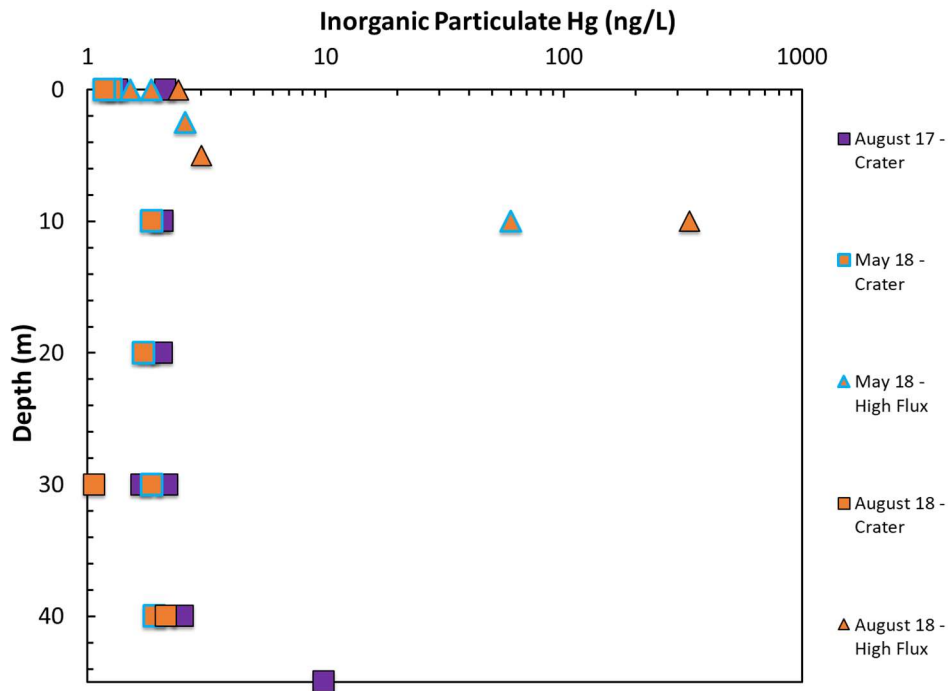
Figure 4.14. Inorganic Particulate Hg. The x-axis is plotted on a log scale. The bottom waters of the 12-m deep pit in the shallow region of the lake holds 10s-100s of ng L^{-1} particulate-bound inorganic Hg.
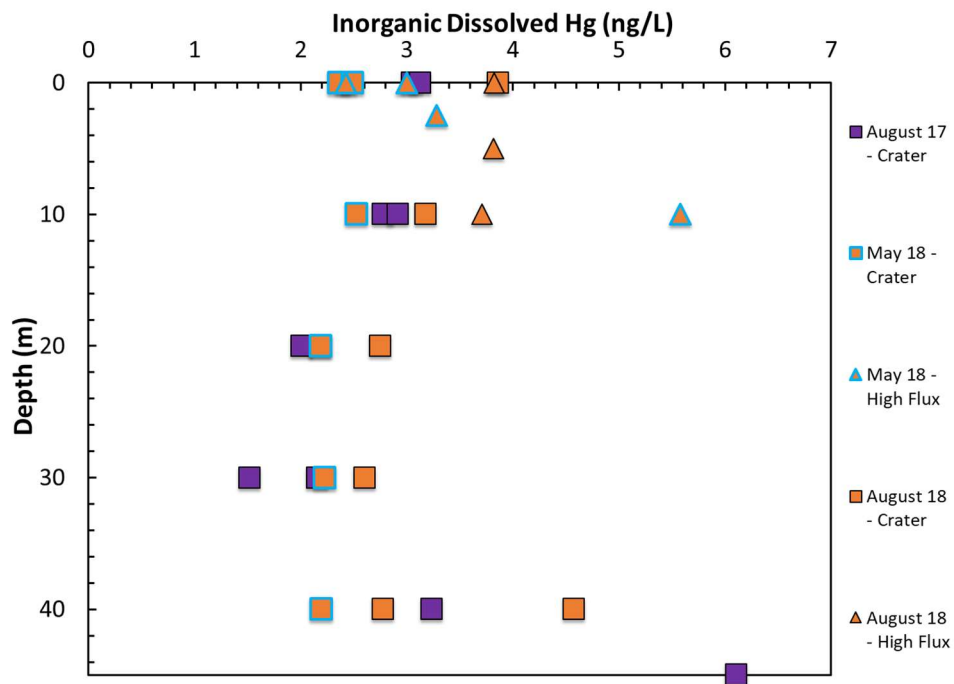
Figure 4.15. Inorganic dissolved Hg. The highest dissolved Hg value was taken in the drowned crater area.
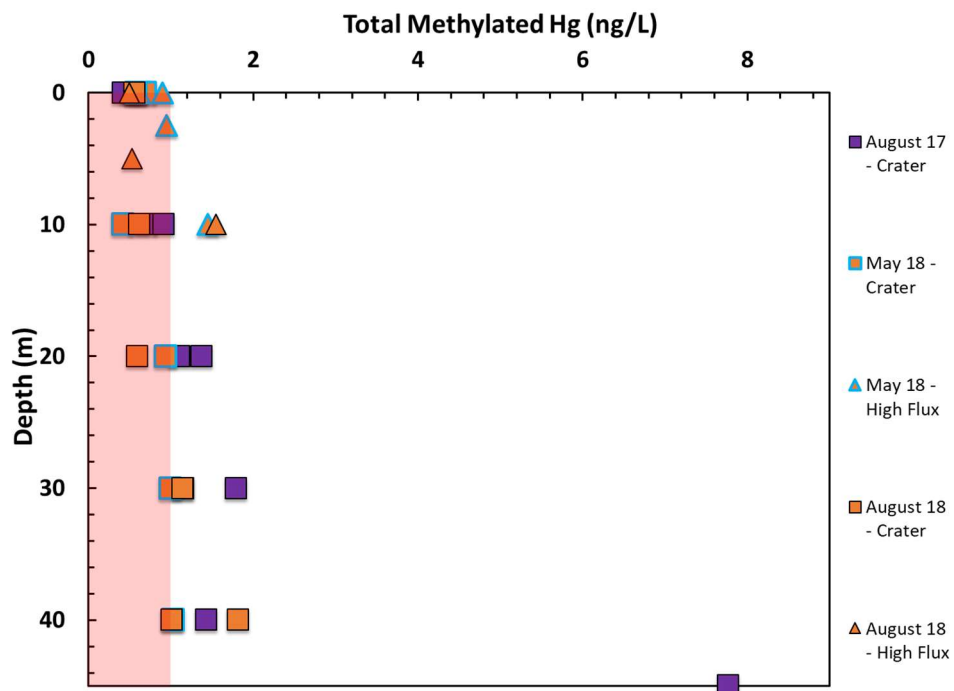
Figure 4.16. Total methylated (particulate + dissolved) Hg. Red box indicates typical (non-volcanic) lake values, where the maximum value of 1 ng L^{-1} is found in deep hypoxic waters (Morel et al., 1998).

	Avg. background concentration (ng/L) (90% of area)	Avg. high-flux zone concentration (ng/L) (10% of area)	Total mass in Lake (g)
Particulate Inorganic	1.96	58.27	652.52
Dissolved Inorganic	2.86	3.66	252.60
Particulate Methylated	0.61	0.28	49.98
Dissolved Methylated	0.64	0.65	55.30
Total Hg (all forms)	6.07	62.86	1,010.39

Table 4.4. Total Hg contents in East Lake, divided into the four forms of Hg.

	ng Hg^0 L^{-1}	Depth
Surface Water	0.191	0-10 m
Deep Water	0.668	50 m
Deep Water	0.365	50 m

Table 4.5. Elemental Hg (Hg^0) in East Lake 2014 samples from the drowned crater area.

4.3 East Lake Sediments

The sediments of East Lake comprise mainly biogenic silica (BSi), organic carbon (C_{org}), and zones of volcanic ash. C_{org} is a mixture of diatoms, cyanobacteria (*Nostoc sp.*) or subaquatic vegetation (SAV) with minimal terrestrial input.

Cores MEL1 and MEL2 are very fine grained, light beige to grey except at depths containing black peaty material with coarse grains and white pumice (Figure 4.17). Some peripheral areas of slices turned orange as the cores dried, but this color did not spread throughout. Some depths contained black (obsidian) and grey grains <1 mm but these were not abundant. Plant material was likewise not abundant through these sediments, and when present came in the form of black needle-like material. Diatoms are abundant and some are macroscopic.

Figure 4.17. *Left:* Slice MEL2-55 sediment with macroscopic diatom. *Right:* Ash layer at bottom of core MEL2.

4.3.1 Water fraction and Bulk Dry Density

The sediments in core MEL1 contain 70-85 wt % water with a decrease to 38-68 wt % in the 51-77 cm depth zone. The sediments in core MEL2 contain 74-85 wt % water with an increase to 90-94 wt % water in the top 7 cm and a decrease to 23 wt % water in the 135-111 cm depth zone. Between depths of 39 and 45 cm, there is a small decrease to 65 wt % water.

The bulk dry density (BDD) for these cores was determined according to equation 3.4 (Figure 4.18). The upper section in core MEL1 has a BDD of about 0.25 g cm^{-3}, and in the lower section there is an increase to 0.74 g cm^{-3} between 61-79 cm depth and a recovery to 0.25 g cm^{-3} between 45-61 cm depth. The sediments in core MEL2 have a BDD of 0.17-0.25 g cm^{-3}, steadily increasing with depth. The top 7 cm of the core decrease to 0.06-0.10 g cm^{-3} and depths 135-111 cm have a BDD of up to 0.97 g cm^{-3}.
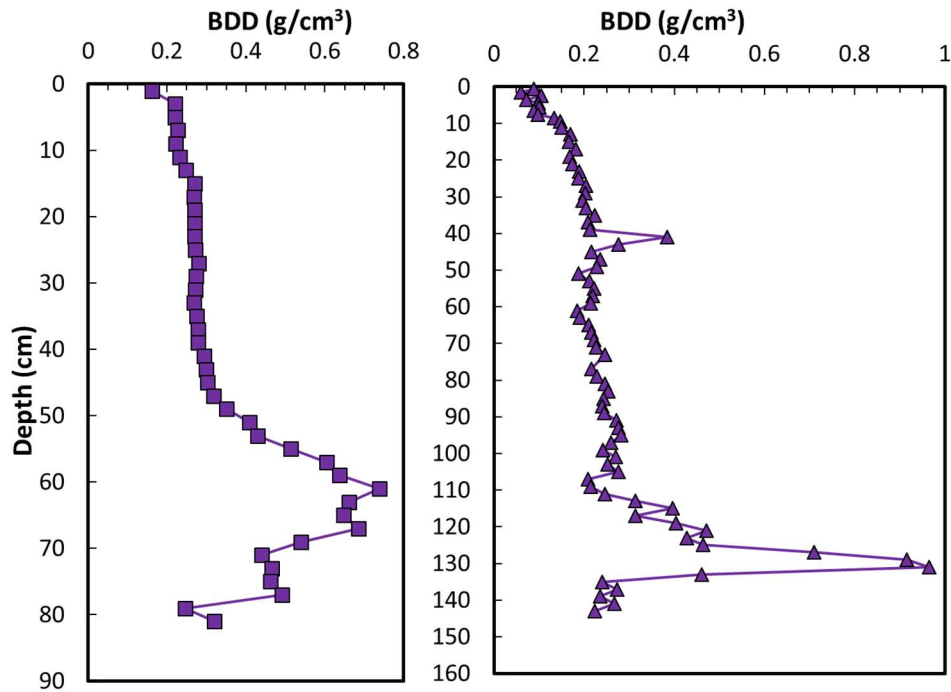
Figure 4.18. Bulk dry density for core MEL1 (left) and MEL2 (right).

4.3.2 Carbon, Nitrogen, and Sulfur

Core MEL1 contains 4-6 wt % C and 0.4-0.6 wt % N in the upper section, with as little as 1 wt % C and 0.1 wt % N in the lower section. Sulfur ranges from 0.3

to 1 wt % throughout the core. Core MEL2 contains 5-8 wt % C and 0.5-1.5 wt % N, with depth 130 cm reaching almost 0 wt % of both. Core MEL2 has about 1.5 wt % S, with maxima of 3 wt % at 27 and 111 cm depth (Figure 4.19).

The C/N ratio can be used to identify what sources of C_{org} are present at a given depth. Both cores show a C/N molar ratio of 8-10, slightly increased over typical lake algae compositions of 6-8 (Figure 4.20; Meyers, 1994). Filters from a plankton net towed through the lake in 2018 show that planktonic organisms – the material that will eventually fall to the bottom of the lake and make up the sediment – carry a C/N ratio of 7.2-7.4 (Table 4.6).

The S in core MEL1, outside the high flux area of the lake, is probably the result of SO_4^{2-} reduction in the pore waters by C_{org} via bacteria. The S in core MEL2 is strongly influenced by the gaseous input.

Material collected from the water column by a plankton net towed behind the boat is likely representative of what will ultimately settle and become part of the sediment. These particles were separated into two size fractions, 20 μm and 100 μm. Each had a molar C/N ratio of about 7.
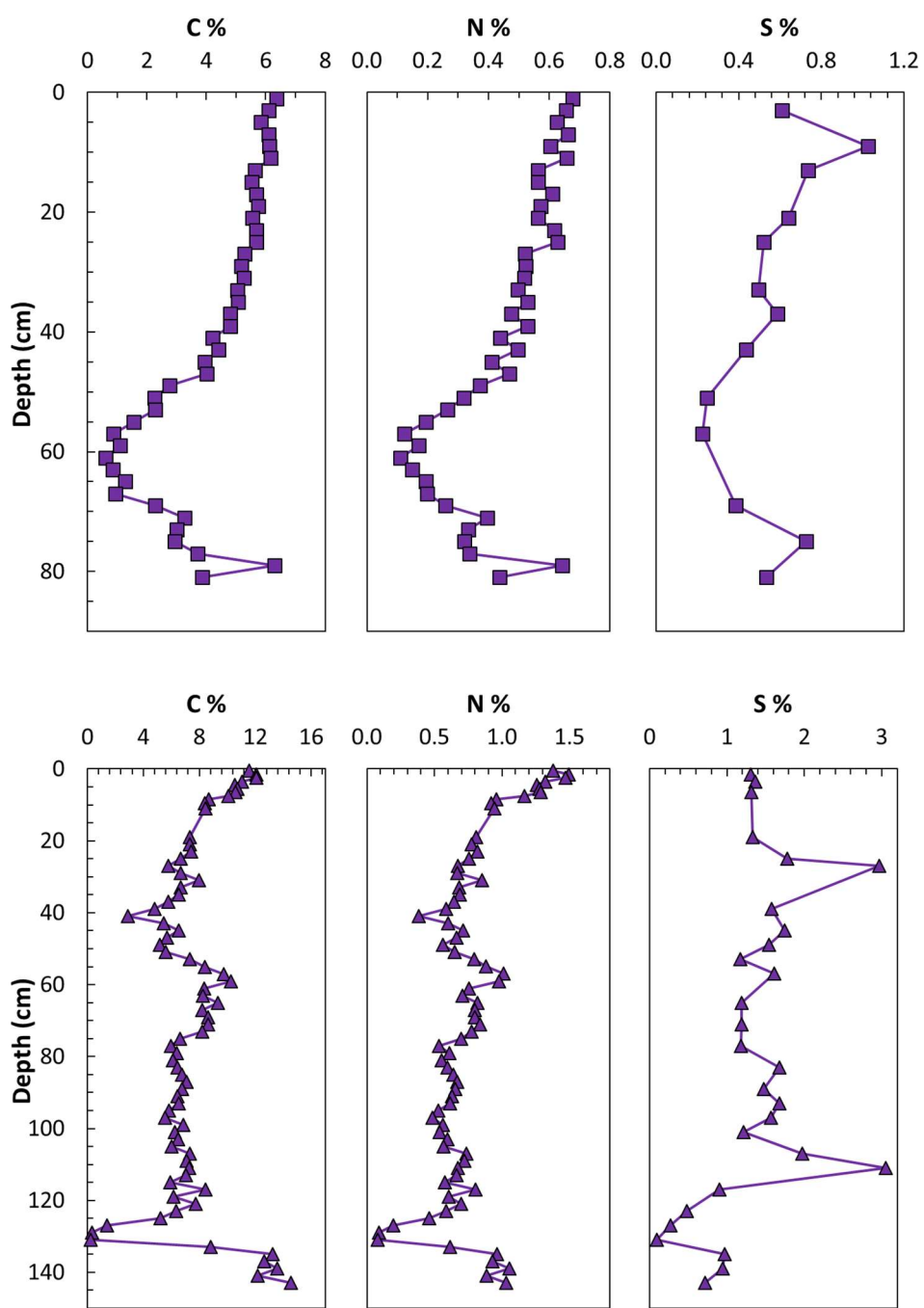
Figure 4.19. Weight percent C, N, and S in core MEL1 (top) and MEL2 (bottom). All carbon in the system is assumed to be C_{org}, as there is no evidence found for carbonate in East Lake sediment.
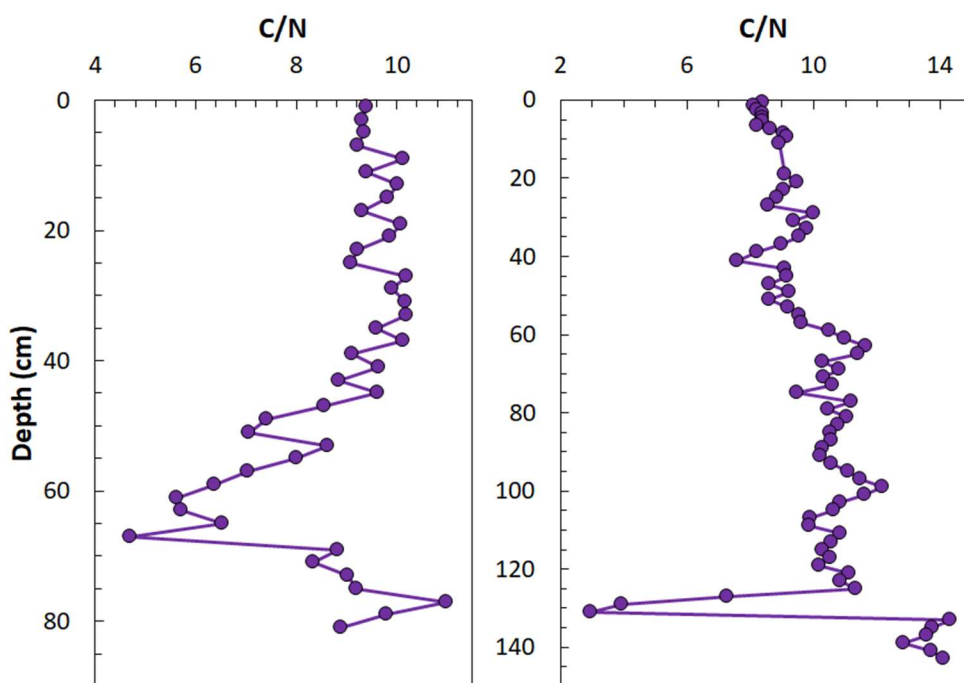
Figure 4.20. Carbon/Nitrogen ratios in core MEL1 (left) and core MEL2 (right).

	Total N (wt.%)	Total C (wt.%)	C/N (molar)
20 μm	4.808	29.748	7.22
100 μm	5.024	31.863	7.40

Table 4.6. Carbon and Nitrogen data for material collected by a plankton net, separated into two size fractions. Typical lake algae shows a C/N molar ratio of 6-8 (Meyers, 1994).

4.3.3 Bulk composition

Traditional oxide content is calculated from major element content for the bulk sediment (Figure 4.21). TiO_2 and MgO are <1% in both cores. K_2O and CaO are 1-3% in core MEL1 and <1% in more MEL2. Total Fe oxides are 3-8% in core MEL1 and 2-5% in core MEL2. Al_2O_3 is 5-13% in core MEL1 and 2-7% in core MEL2. Si content is out of range on most samples for the instrument used, which means SiO_2 content is greater than 64%. P_2O_5 is less than 0.01% through both cores.

62
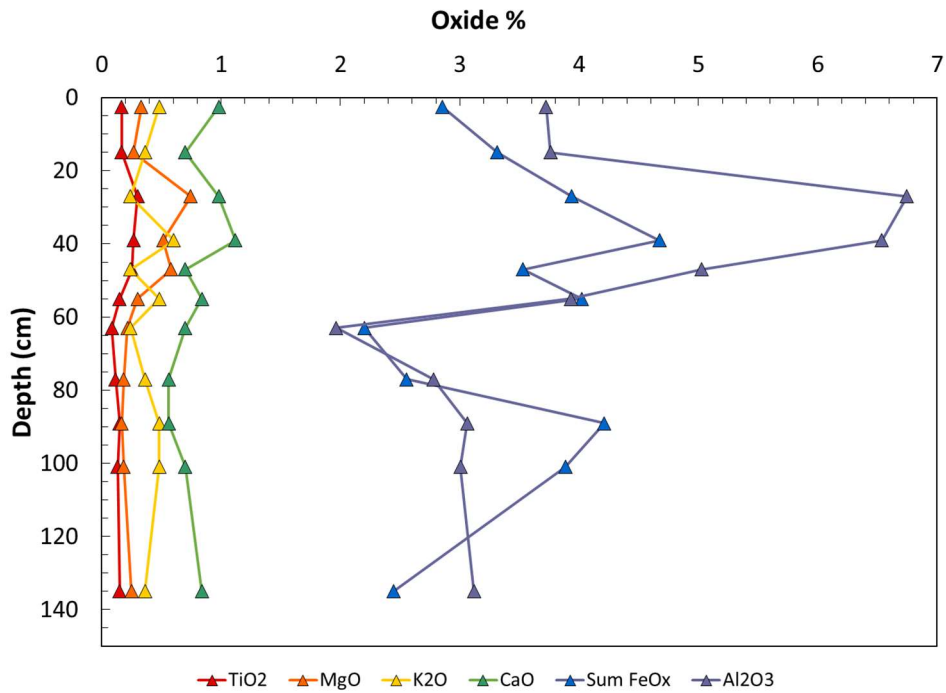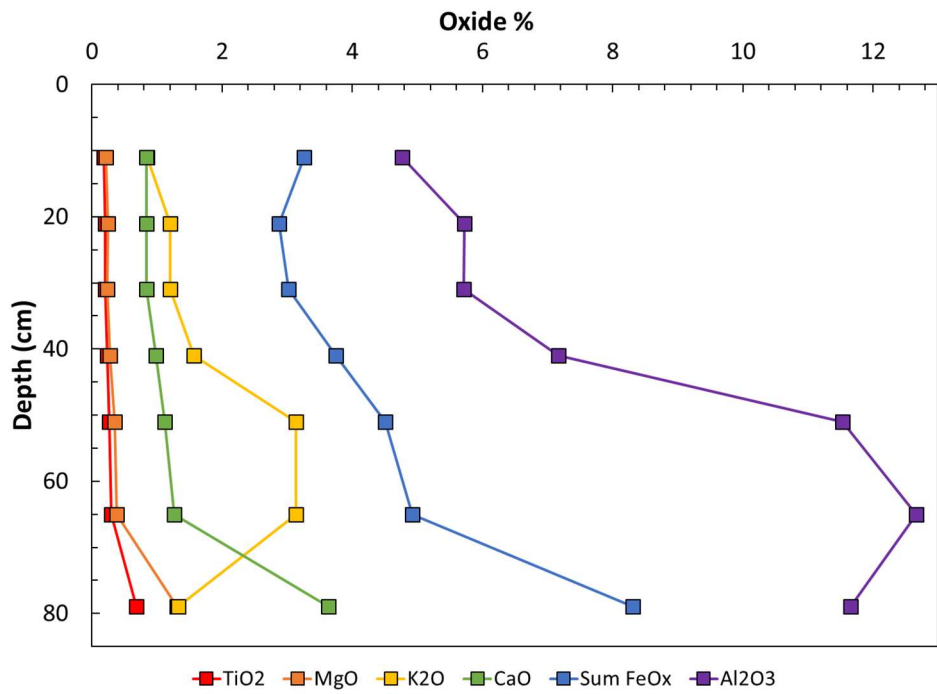
Figure 4.21. Major oxide content for bulk sediments in core MEL1 (*top*) and MEL2 (*bottom*).

Energy dispersive spectroscopy carried out on the SEM provides visual indication of electron-dense materials in the sediment as well as elemental composition of those materials by atomic percent (Table 4.7). These materials are identified as biogenic materials (diatoms), large grains, and clusters of small grains (Figure 4.22). Major element components of these particles are O, S, Fe, Si, and K. Hg is also suspected to be present based on known lake composition but is near the low end of the detection limit on this instrument.

Atomic %	S	Fe	Si
Clusters of small grains	9.85	4.11	18.24
	29.36	17.12	5.76
	35.11	19.01	8
	37.3	22.86	5.92
Diatoms	29.21	13.97	10.34
	30	17.93	6.01
	33.83	19.82	7.74
Large grains	18.36	8.31	12.88
	19.04	8.45	14.26
	31.82	18.49	6.53
	37.27	19.29	5.76
	37.42	21.68	7.67
	41.51	22.59	5.91
	38.61	25.91	6.57

Table 4.7. Atomic % of electron-dense materials identified in sediment slice MEL2-55 by SEM-EDS.
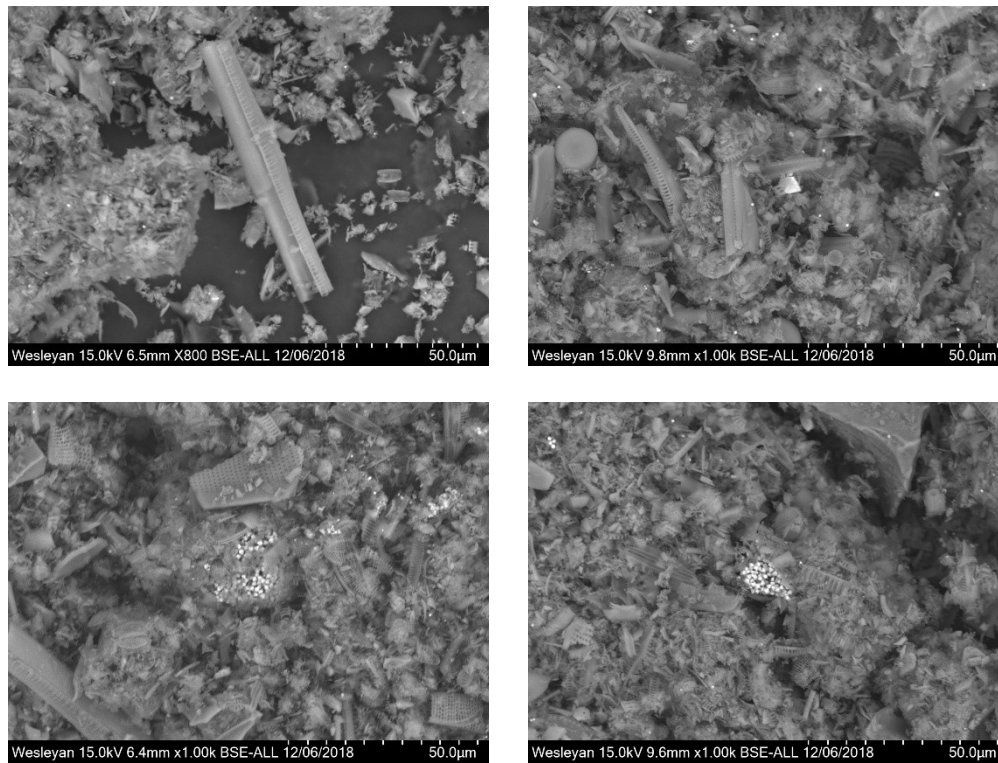
Figure 4.22. Back-scatter electron images from SEM, core MEL2, 55 cm depth slice. Sediment consists primarily of diatoms (biogenic silica, *upper left*), with large individual electron-dense grains (*upper right*) and clusters of smaller ones (*bottom*).

4.3.4 Mercury

The bottom section (depths 35-143 cm) of core MEL2 has 3-8 ppm Hg, except depths 111-133 cm which contain only 0.2-1 ppm Hg. There is a maximum Hg level of 13 ppm at 55 cm depth and a local minimum of 4 ppm at 41 cm depth. The upper 35 cm carry 7-11 ppm Hg; up to an order of magnitude larger than those values found in the other East Lake sediment cores. core MEL1 Hg values are in the same range as the low values of cores collected in East Lake in earlier years, ranging from 0.1-1.5 ppm. The upper 45 cm of the core carry about 1 ppm Hg, while the lower 36 cm carry <0.5 ppm Hg (Figure 4.23).
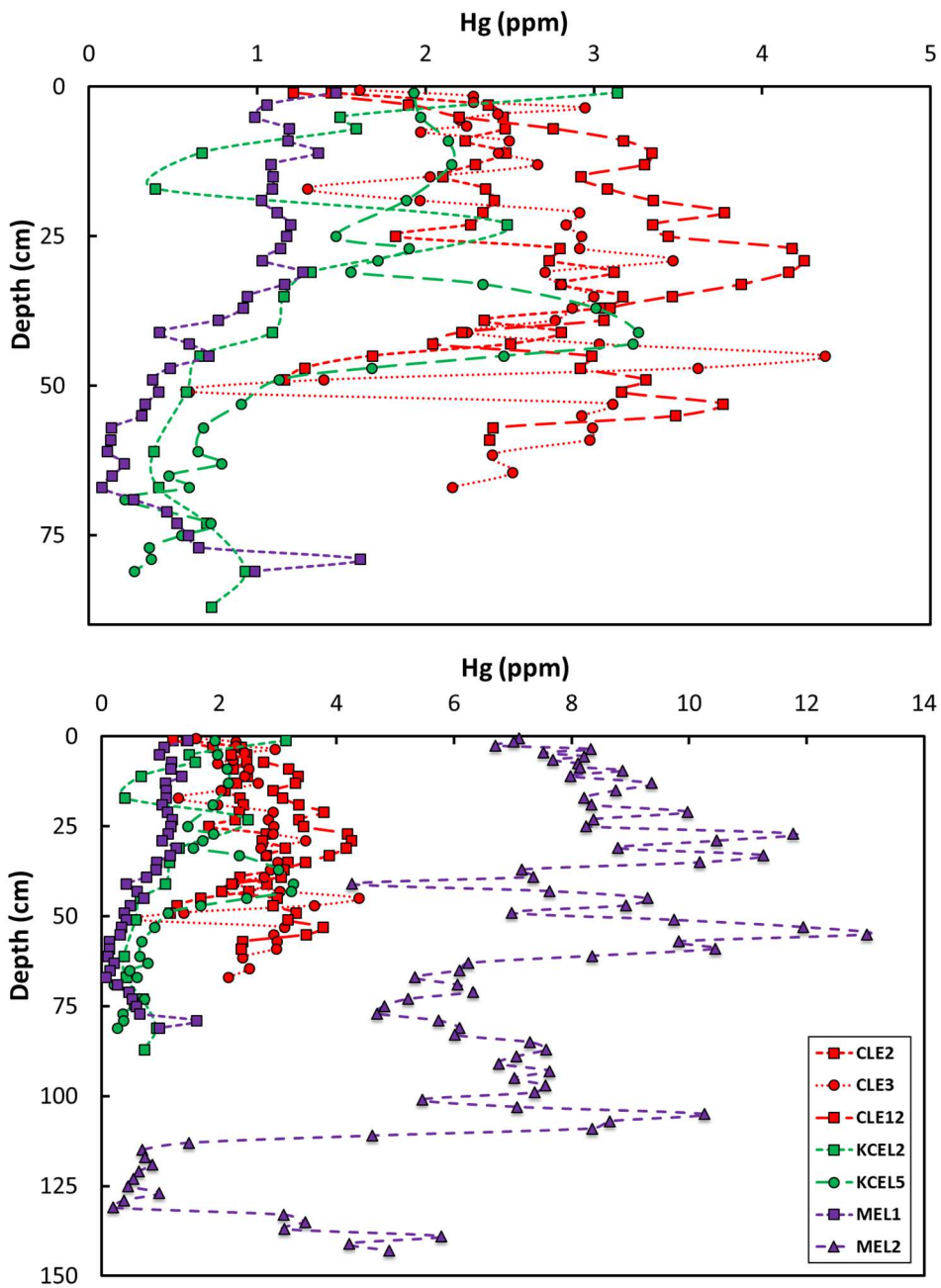
Figure 4.23. *Top:* Cores collected in 2011 and 2015 contain 1-4 ppm Hg. One core from 2017 (MEL1) is also in this range. *Bottom:* core MEL2 from 2017 contains 5-13 ppm Hg.

Material collected from the water column by a plankton net towed behind the boat carried 2.8 ppm Hg in the 100 μm fraction and 3.6 ppm Hg in the 20 μm fraction.

Three core slices from 2017 and one from 2011 were run for MeHg in sediment, and are presented in table 4.8.

Core	Depth (cm)	MeHg (ppb)	Total Hg (ppb)	Hg % methylated
CLE3	23	1.156	2,579	0.045
MEL1	21	0.885	1,116	0.079
MEL2	27	5.637	11,775	0.048
MEL2	93	1.629	7,629	0.021

Table 4.8. MeHg in two sediment slices from high flux core and two slices from background cores. Total Hg is is 0.02-0.08% methylated and shows no geographical pattern.

4.3.5 Hydrothermal elements

The geothermal fluid input to East Lake is minimal, sourced solely from the hot springs on the south shore. This area is noted for its input of gas bubbles, and those bubbles must have fluid walls to contain that gas. It is a small input, but it accounts for the fluid-associated elements found in this area. Past periods of hydrothermal fluid seeps are evidenced where concentrations of water-soluble elements Fe and As increase above background levels. Previous and ongoing work at Paulina Lake, whose volcanic input is mainly fluid, demonstrates that Fe and As are some major elements that travel with the liquid phase.

Relative to Paulina Lake, concentrations of Fe and As in the sediment column are low (Figure 4.24). Weight % of Fe is 3 at the bottom of core MEL1 and decreases to 1 by the surface of the core. In core MEL2, Fe ranges from 1 to 2.5 weight % with maxima at 110 and 40 cm depth. Arsenic also has a peak of 100 ppm at 110 cm depth

in core MEL2, and otherwise ranges from 10-50 ppm. Arsenic in core MEL1 ranges from 20-75 ppm, with a segment of increased values between 30 and 60 cm.

4.3.6 Ash tracers

The elements Y, Rb, and Ba are of interest here because they are enriched in rhyolitic ash layers (Kuehn, 2002). In core MEL1, Y ranges from 15 ppm near the top of the core to 25 ppm near the bottom, with peaks of 35 ppm at 51 and 65 cm depths. Rb ranges from 30 ppm at the top to 50 ppm at the bottom with peaks of 80 ppm at the same depths. Ba ranges from 300 to 600 ppm, with peaks around 700 ppm, also at the same depth. (It should be noted that Ba also commonly travels with the hydrothermal phase and may here signify an input from either/both.)

In core MEL2, Y is around 10 ppm through the core with little variation except where it reaches over 35 ppm at 127-131 cm depth. Rb is around 10 ppm through the core except a peak of 35 ppm at 41 cm depth and 100 ppm at 127-131 cm depth. Ba is around 130 ppm through the core except a peak of 333 ppm at 41 cm depth and 800 ppm at 127-131 cm depth (Figure 4.25).

The bulk dry density (BDD) of sediments from both cores varies between 0.1 and 0.3 g cm^{-3} with core depth. Samples in core MEL2 at 41 cm depth and 115-133 cm depth and samples in core MEL1 at 47-77 cm depth have higher BDD up to 0.9 suggesting the present of an ash layer, devoid of light organic material (Capece, 2016). Volcanic ash is deposited quickly as a snapshot in time and carries little to none of the elements deposited steadily by secular processes.
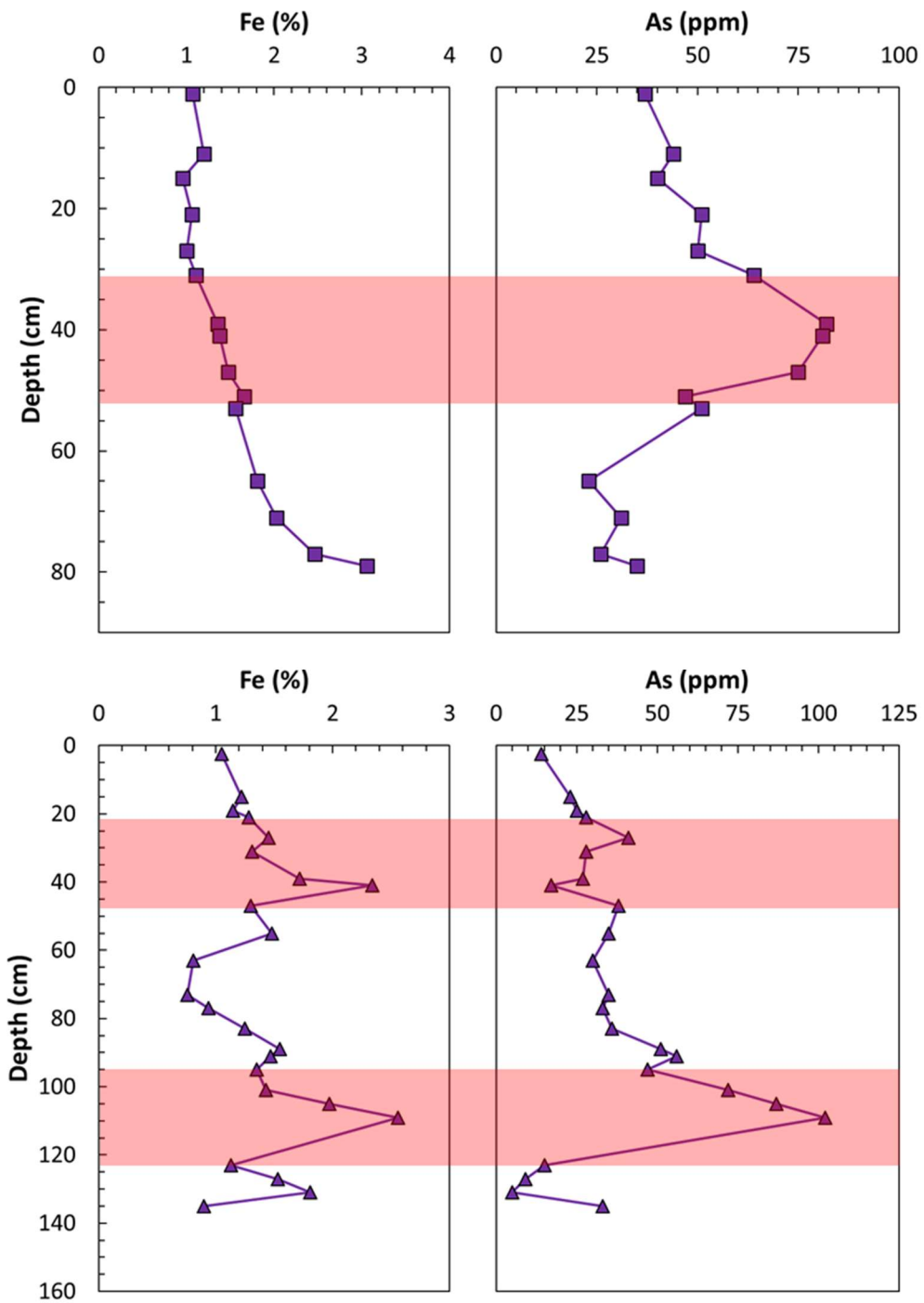
Figure 4.24. Iron and Arsenic in core MEL1 (top) and MEL2 (bottom). These elements travel with the hydrothermal fluid phase, not the gas phase, and are common in Paulina Lake but rare in East Lake.
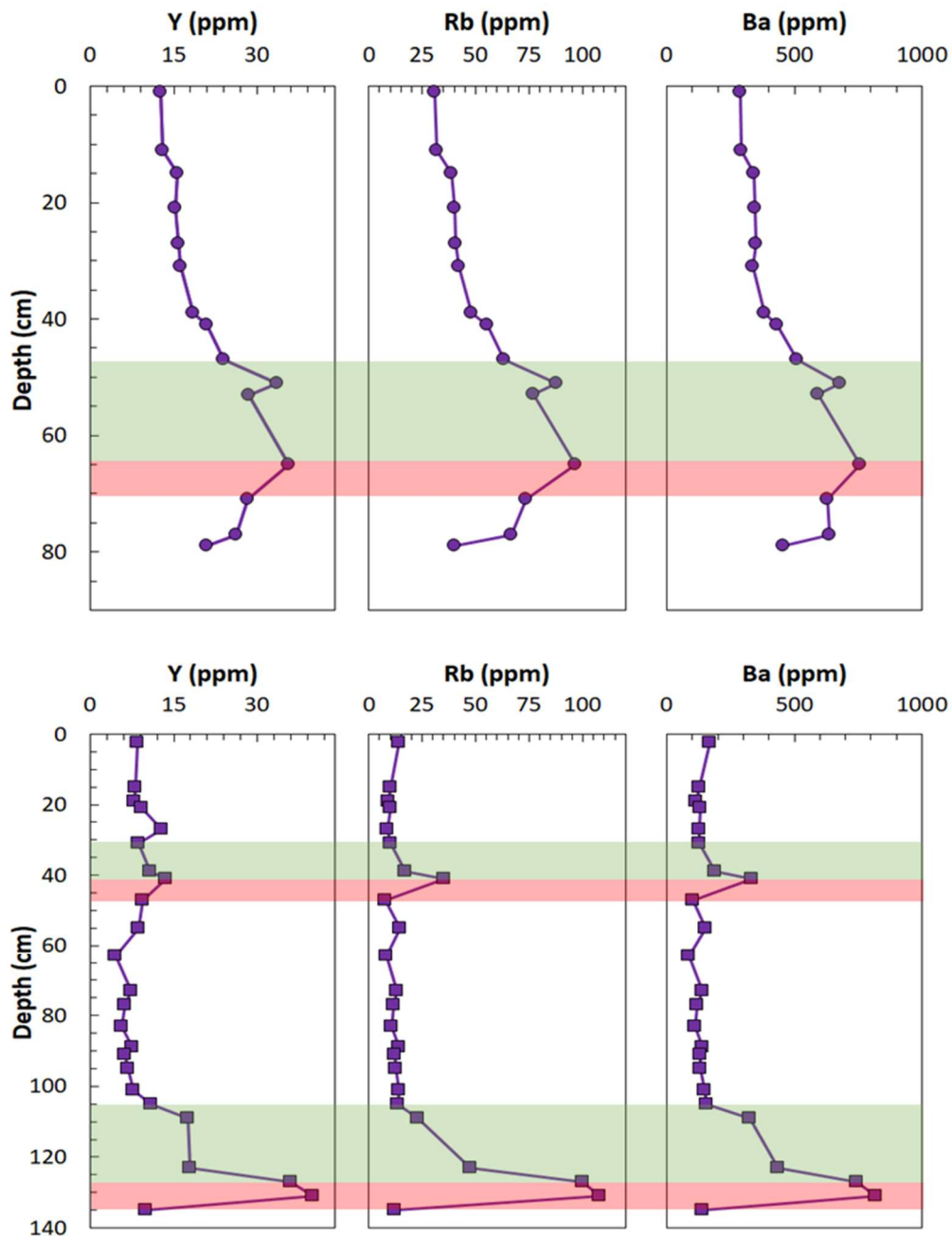
Figure 4.25. Common ash-tracer elements in MEL cores. Onset of ash (red) represents an instantaneous accumulation in geologic time. Rate of recovery to background levels of these elements (green) is likely due to ash within the watershed (Newberry crater) being carried into the lake by natural processes.

Chapter 5: Discussion

Understanding potential secular variations in the influx of Hg and CO2 in East Lake demands insight into the lake processes that modify those fluxes through temporary storage or direct precipitation of mineral phases. This study follows the understanding that East Lake is in steady state (Lefkowitz et al., 2016), where Hg and C contents are approximately constant and the input is equal to the output. For this reason, Hg influx can be quantified by what ends up in the sediments, and CO_2 influx can be quantified by what exits out the lake surface. Bulk deposition rates are thus determined to assign an annual deposition rate for Hg. Finally, these values are then be compared to other volcanic locations to place East Lake in a global context.

5.1 Physical and Chemical Nature of East Lake

East Lake is a dimictic, seasonally stratified lake, with a well-mixed epilimnion probably influenced by the common westerly winds. The deeper waters held in the crater area of the lake are separate from this mixing (Lefkowitz et al., 2017). The thermocline is shallower in late-summer and represents a larger temperature difference between the epilimnion and the hypolimnion than either autumn or early summer, as the surface waters stay in thermal equilibrium with the air above by radiation.

Major element concentration data for East Lake water appears constant over time and depth. These elements are at values slightly more concentrated than found in

non-volcanic lakes that are fed with sediments by rivers. Given that East Lake has no fluvial input, these species must be sourced from volcanic input.

Many of the elements measured don't show significant depth trends, except Si and Ca. Silicon may show nutrient behavior in the surface waters as it is taken up by diatoms to make their SiO_2 shells. The concentration of Si in the bottom waters is higher than in the epilimnion, likely due to some hydrothermal fluid inputs and to dissolution of the diatom frustules when the organisms die and settle.

Evasion of CO_2 from the surface waters shifts carbonate equilibrium away from carbonic acid (H_2CO_3) and increases the pH, while addition of CO_2 into the bottom waters decreases the pH values. In the photic zone - where photosynthesis occurs and CO_2 escapes at the surface - carbon dioxide is consumed and taken out of the water. Thus, carbonic acid content decreases as a result of the pH increase. In the bottom waters, both the volcanic CO_2 input and the action of organic decay increase acidity (decrease pH). Such a gradient builds over the course of the season, from a near-homogenous lake immediately after spring overturn. The pH gradient thus is strengthened over the course of the summer when the homogenous waters have time to again become stratified. When the epilimnion reaches a higher pH, it yields a higher ratio of bicarbonate (HCO^-) to CO_2. The subsequent lower pCO_2 in late-summer than spring provides for a decreased surface flux at that time.

5.2 Seasonal Changes in Carbon Dioxide Flux

Volcanic lakes serve as a particularly large source of CO_2 to the atmosphere due to volcanic gases dissolving into the water. On top of this, lakes are generally a CO_2 source to the atmosphere due to high biologic activity (respiration), oxidation of organic matter in the sediment, and the oxidation of imported suspended terrestrial carbon.

East Lake CO_2 flux measurements from August 2017 and 2018 showed an average flux rate of 0.26 and 0.20 moles CO_2 m^{-2} day $^{-1}$, respectively. These numbers agree with previous data collected by Capece (2016, collected 2015) and Brumberg (2017, collected 2016) which show average fluxes in June of 0.24 and 0.28 moles CO_2 m^{-2} day $^{-1}$, respectively. Measurements from May 2018, just three weeks after ice cover melting, showed a much larger average flux rate of 0.51 moles CO_2 m^{-2} day $^{-1}$. The CO_2 flux was elevated over the entire lake in May 2018, but the greatest flux was along the north cliffs, where the walls of the lake enter steeply and reach down into the deep crater area. This is consistent with mixing models where degassing is channeled along tectonic structures (Andrade et al., 2016).

The daily whole-lake CO_2 flux in May 2018 was 95 tonnes: about double the value for June and August (37-51 tonnes). Measurements of flux taken in spring were generally higher than those taken in summer, as CO_2 released into the lake from below throughout the winter has no way to escape so it builds up in the water. Ice melting is accompanied by spring turnover which initiates agitation of bottom waters and release of dissolved gases, as well as homogenizing the water column. Flux

measurements taken in late summer are lower due to the higher epilimnal pH values and the strong thermal stratification that impedes easy transfer of CO_2 from deep to shallow waters (Andrade et al., 2016). As argued above, the summer flux measurements may still contain the tail end of the built-up winter CO_2 release.

The steady-state volcanic input should be 9,000 tonnes CO_2, or 25 tonnes CO_2 per day (6.7 tonnes C per day), according to a power function decay model fit to the data, $y=70100 * x^{-1.6}$ (Figure 5.1). While the observed daily fluxes vary from 37-95 tonnes day^{-1}, the lowest observed summer fluxes are still larger than the calculated daily input. East Lake has a complete ice cover from the beginning of November to the end of April, for 26 "winter" weeks. During this time, 173 t CO_2 per week is added to the lake under the ice, for a total of 4,500 tonnes of excess gas. During the other 26 "summer" weeks, when there is no ice cover, there is still a release of 173 t CO_2 per week into the lake, which together with the pH, T, local mixing processes, and diminishing resident winter CO_2 creates a P_{CO2} that determines the escape rate at the surface.

The entire 9,000 tonnes CO_2 must escape during the summer months where there is no ice cover on the lake, and for this reason the daily flux is always larger than 25 tonnes CO_2. With no added biologic or dissolution effects, the winter CO_2 would be released from the lake following exponential decay. However, the overprinting of lake processes means it is a more complicated function.

In East Lake, all the winter gas buildup is released over the following summer. This is not the case for all lakes – work by Chiodini et al. (2012) at Lago

Albano demonstrates that if there is a catastrophic injection of CO_2, elevated levels may still be seen two decades later. The decay of CO_2 dissolved in Lago Albano does indeed fit an exponential model, possibly because the 6×10^7 kg of CO_2 injected gives a strong enough signal to overwhelm competing lake processes.
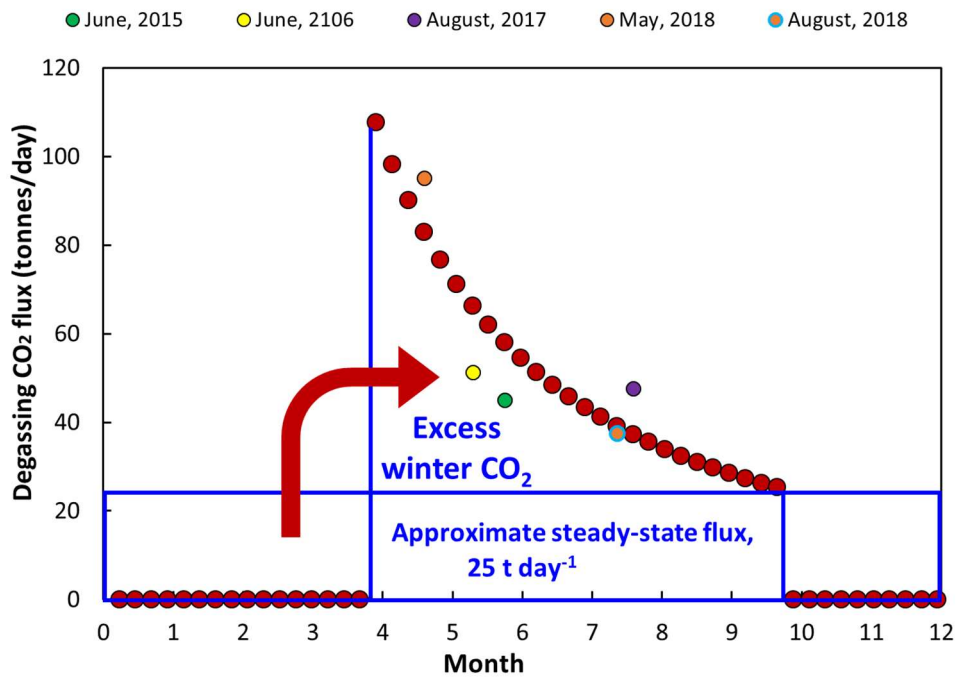
Figure 5.1. Calculated daily CO_2 flux values from five expeditions fit to a power function model, $y=70100 * x^{-1.6}$. Approximately 25 t CO_2 is emitted per day, but observations are always larger than this because gas built up in the lake during the winter is added to the summer flux. CO_2 that builds under the winter ice cover would alone decay along an exponential model, but seasonal lake processes change CO_2 solubility in the waters and complicate the pattern.

Gas emission from the lake surface occurs by two methods: bubble transport or diffusion (Mazot and Taran, 2009). Across 90% of East Lake, CO_2 is released by diffusion (passive). Gas that enters at the lake floor (55 m depth) as bubbles at 6.5 bar

CO_2 (Brumberg et al., *unpublished manuscript*) quickly dissolves into the water as it rises, such that the bubbles are either completely dissolved or microscopic in size when they reach the surface. The exception to this is in the "high flux zone" (10% of surface area) shown in the combined late-summer SGS map for 2015-2018, around the 12-meter deep pit in the southeast section of the lake. This zone is taken to be the major site of volcanic gas input to East Lake and is expected to carry high Hg levels along with CO_2 (Varekamp and Buseck, 1986).

The expansion of the high-flux zone may be related to local fractures opening up in a larger area, but at this time do not seem to have influenced the overall CO_2 flux of the lake. There is no evidence for carbonate formation in East Lake, so all the incoming CO_2 must be either released to the atmosphere or incorporated in the sediment as organic material.

The estimated global CO_2 emission from volcanic lakes is $112 +/- 19$ Mt yr^{-1}, which is close to 30% of global CO_2 emission from subaerial volcanoes and a significant portion of the global carbon budget (Perez et al., 2011). Neutral lakes with pH 6-8 account for 72 Mt yr^{-1}, which is most of this release (Perez et al., 2011). A suite of CO_2-emiting lakes compiled by Perez et al.(2011) is shown in Figure 5.2, with the Newberry Lake data from this and concurrent studies added. East Lake falls within the expected range for a neutral volcanic lake of its surface area.
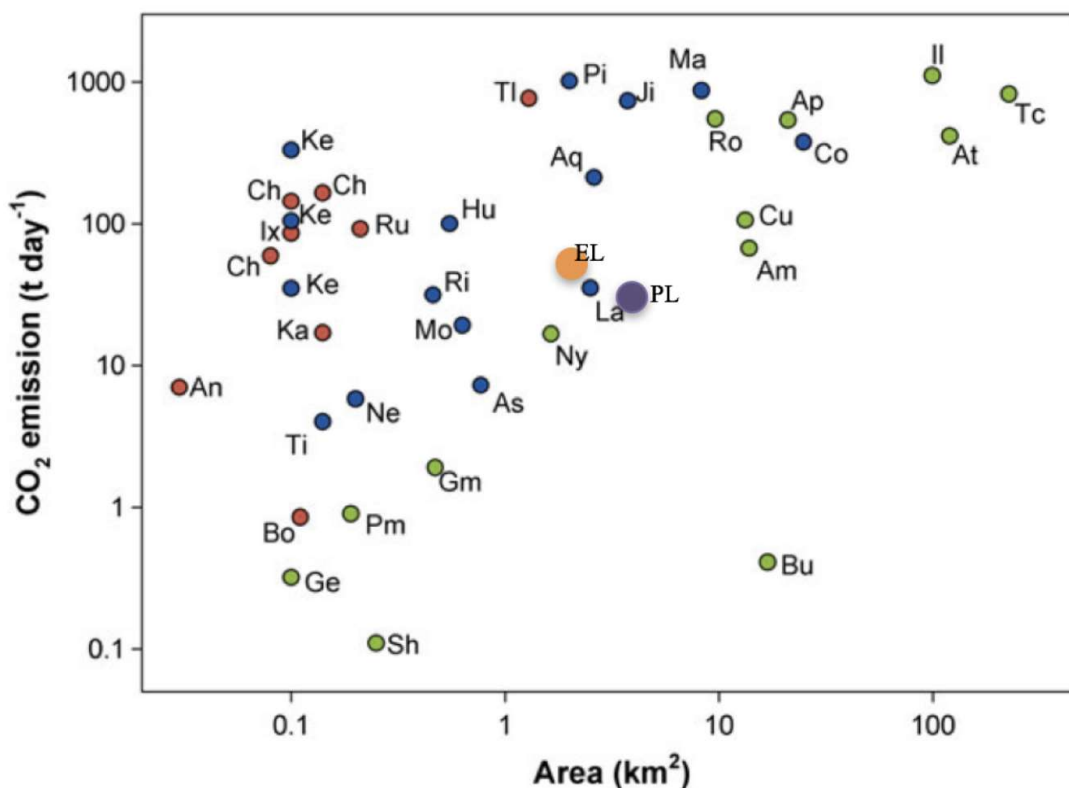
Figure 5.2. CO_2 flux from different volcanoes, with surface area. Red circles are acidic lakes, blue circles are neutral lakes, and green circles are alkaline lakes (Mazot and Bernard, 2015; Pérez et. al, 2011). Y-axis is a log scale. The orange circle indicates East Lake, and the purple circle indicates Paulina Lake.

Annual degassing of CO_2 has been measured at other volcanic lakes and hydrothermal systems (Table 5.1). Mt. Etna, for example, is recognized as the one of the largest atmospheric inputs of volcanic CO_2, at 25 Mt yr^{-1} (6.8 Mt C yr^{-1}). This extreme flux is due to de-carbonization of limestone and dolomite of the bedrock beneath the volcano (Hards, 2005).

Passive degassing		
Location	Annual CO₂ Flux	Reference
Mt Etna	25 Mt	D'alessandro et al., 1997
Mammoth Mountain, CA	0.21 Mt	Evans et al., 2002; Gerlach et al., 2001
Yellowstone hotspot	1.6+/- 0.6 Mt	Werner and Brantley, 2003
Eruptive events		
Location, Year	CO₂ Flux	Reference
Pinatubo (1991)	42 Mt	Gerlach et al., 1996
Mount St. Helens (1980)	4.8-22 Mt	Casadevall et al., 1983

Table 5.1. Local CO_2 emissions for passively degassing and erupting volcanoes.

5.3 Determination of sedimentation rates

For a quantification of the accumulation of Hg and C in the sediment bed, it is necessary to determine both the amount of Hg in the sediment and the rate at which those sediments were deposited. Two linear sedimentation rates are calculated here by means of ^{210}Pb for the upper 16 cm of core, and by means of tephrochronology for the deeper part.

Excess ^{210}Pb in the top of core MEL2 is around 300 milli-Bq g^{-1}, with decreasing values until 18 cm depth, where no appreciable ^{210}Pb* is detected. A best-fit line applied to the data gives an initial concentration of 499.6 mBq g^{-1} at time t=0 (deposition). Using the half-life for this system, 22.3 years (Nittrouer et al., 1979), the decay constant is calculated as

$$\lambda = \frac{\ln(2)}{22.3} \qquad \text{(Eq. 5.1)}$$

and the years since deposition for each slice can be calculated as

$$age = \ln\left(\frac{excess\ Pb}{499.6}\right) \div -\lambda \qquad \text{(Eq. 5.2)}$$

where the age refers to how many years the sediment was deposited before the collection date, following the Constant Initial Concentration model (Nittrouer et al., 1979). Dating by ^{210}Pb gives a sedimentation rate of 1.29 mm yr^{-1} over the top 16 cm of core MEL2 (Figure 5.3).
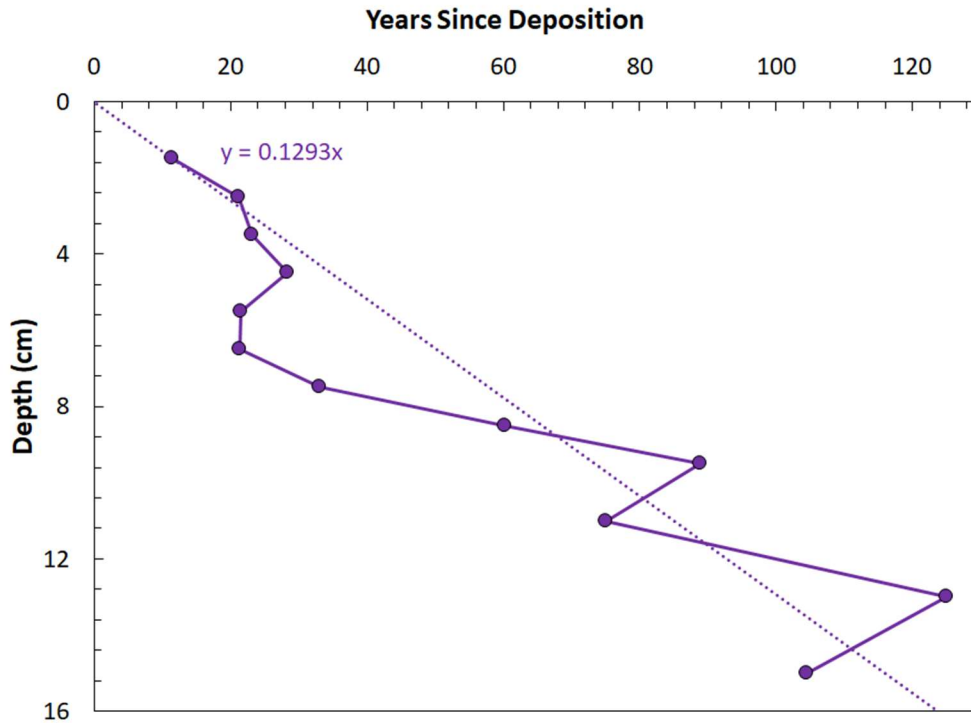
Figure 5.3. Sediment slice age via ^{210}Pb age. Best fit line applied to these data gives a deposition rate of 0.1293 cm yr $^{-1}$, with the assumption that sediments at 0 cm depth have an age of 0 years. Constant calculated age for upper 7 cm may be evidence of re-working.

Two distinct ash layers are identified in core MEL2, one at 41 cm depth and one at 131 cm depth. A broad zone of ash is identified in core MEL1, from 57-67 cm depth.

If the sedimentation rate is assumed constant since deposition of these layers, it can be determined from the known age of that ash. The ash layer at 41 cm has not

been correlated to any known regional volcanic eruption about the estimated time. The ash layer at 131 cm depth is recognized by major and trace element compositions as the Paulina Lake Ashflow (PLAF, Figures X, X) defined by MacLeod et al. (1995) via ^{14}C dating as having a calibrated age of 1240 BP.

The rare earth element (REE) composition of this ash layer are compared to those values of pure ash reported by Kuehn (2002). Because the ash in East Lake is diluted, these numbers are all lower than the pure ash. Since there is Y in the ash but not in the bulk sediment, the ratio of Y in the MEL2 layer to Y in the PLAF ash is used to determine what percent of the sediment is ash. REE values show a 1:1 match in the heavy REEs, and a slight enrichment in the MEL2 slice for the light REEs (Figure 5.4).

The identity of this ash layer is also confirmed with binary comparison of elements found in ash but not bulk sediments (Kuehn, 2002). A line from the PLAF values to the origin represents that ash diluted by bulk sediment, and the MEL2 slice falls approximately on this line (Figure 5.5).

Mapping by MacLeod et al. (1982) suggests this pumice fall erupted from a vent very near the Big Obsidian Flow. This method gives an average deposition rate of 1.06 mm yr^{-1}, which includes an increased deposition rate during the eruptive events, averaged over the whole core. Where there is deposition from ash-producing eruptions, the instantaneous addition of more material causes more sedimentation in a given length of time.
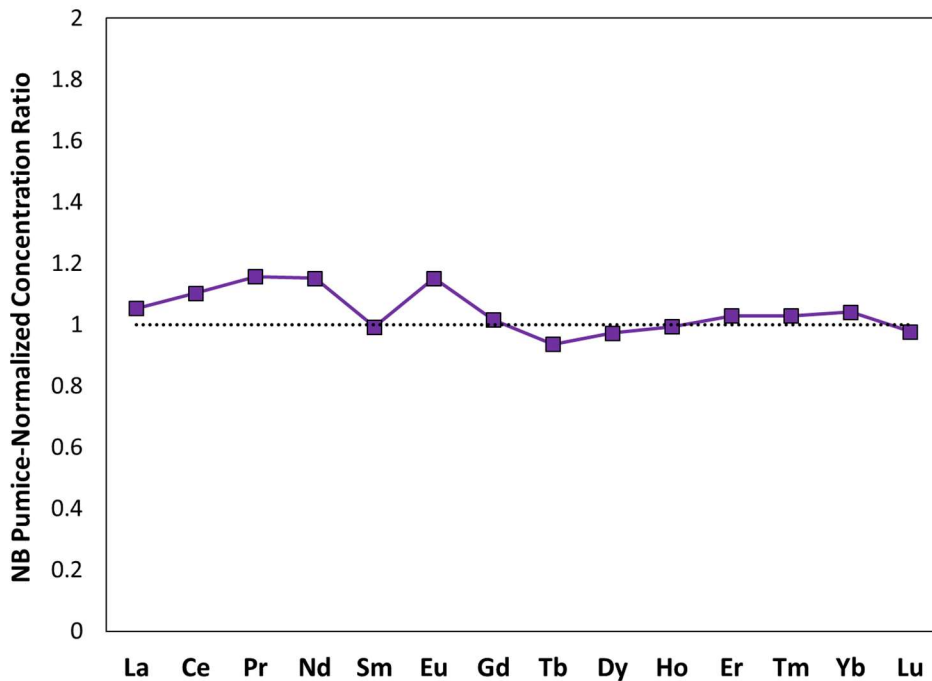
Figure 5.4. Spider diagram for REEs. Values are MEL2 ash divided by Newberry Pumice values (Kuehn 2002), normalized for dilution with ratio of Y in MEL2 ash to Y in Newberry Pumice.

Both methods, tephrochronology and ^{210}Pb dating, agree on a sedimentation rate of the same order (1.06-1.29 mm yr $^{-1}$) but it should be noted that the Pb-210 method assigns ages based on years before collection, while the PLAF method is based on a radiocarbon age (converted to 720 AD calendar year according to tree ring record).

5.4 Hg and C accumulation and storage

The calculated average sediment mass accumulation rates (MAR) from core MEL2, excluding ash layers, is 0.023 g cm^{-2} yr $^{-1}$. With the range of 3-13 ppm Hg and 5-15 wt% C, this accounts for a Hg accumulation rate of 1.72 mg m^{-2} yr $^{-1}$ and a C
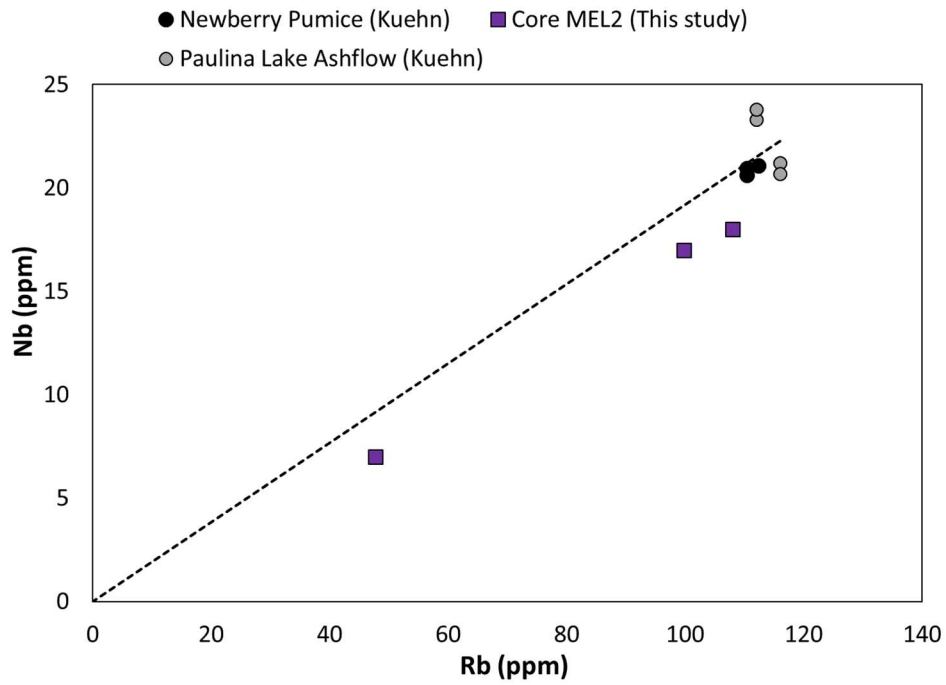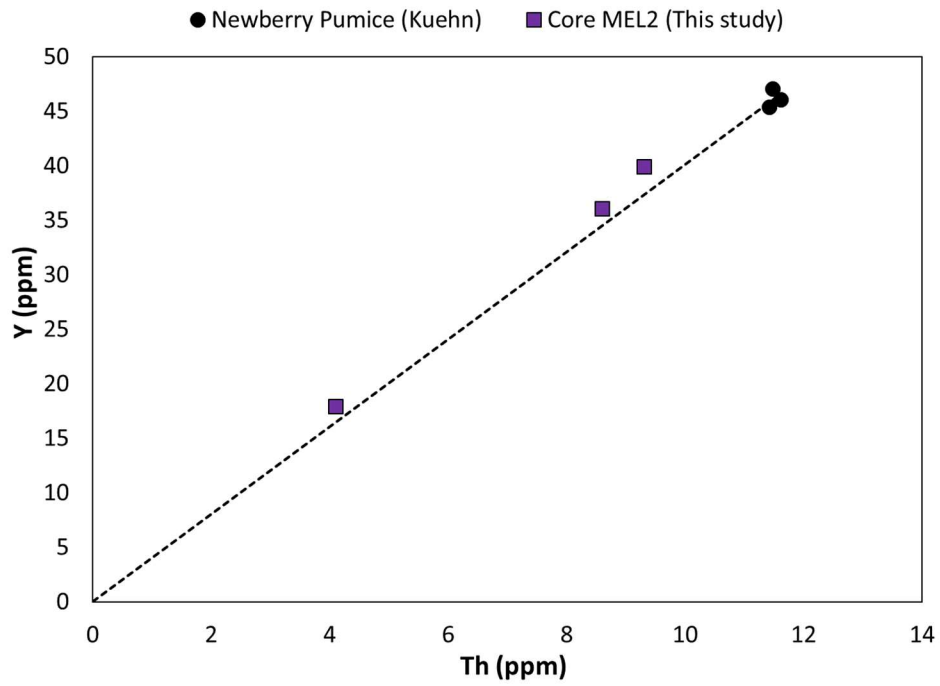
Figure 5.5. Binary plots for elements found in rhyolitic ash. MEL2 ash falls within the trend for Newberry Pumice/PLAF, with varying levels of dilution.
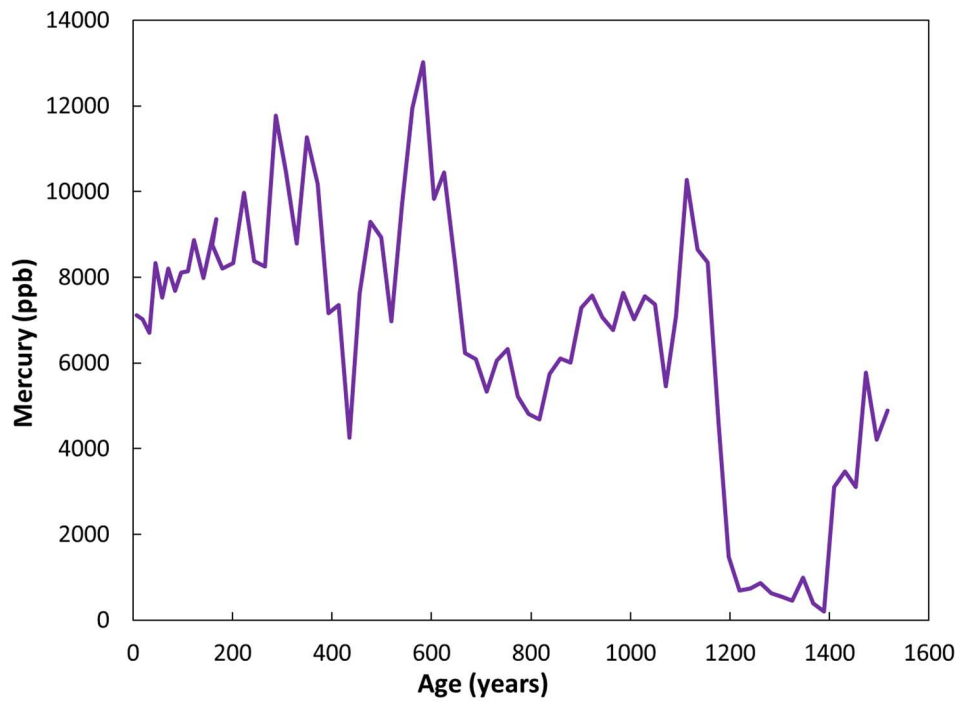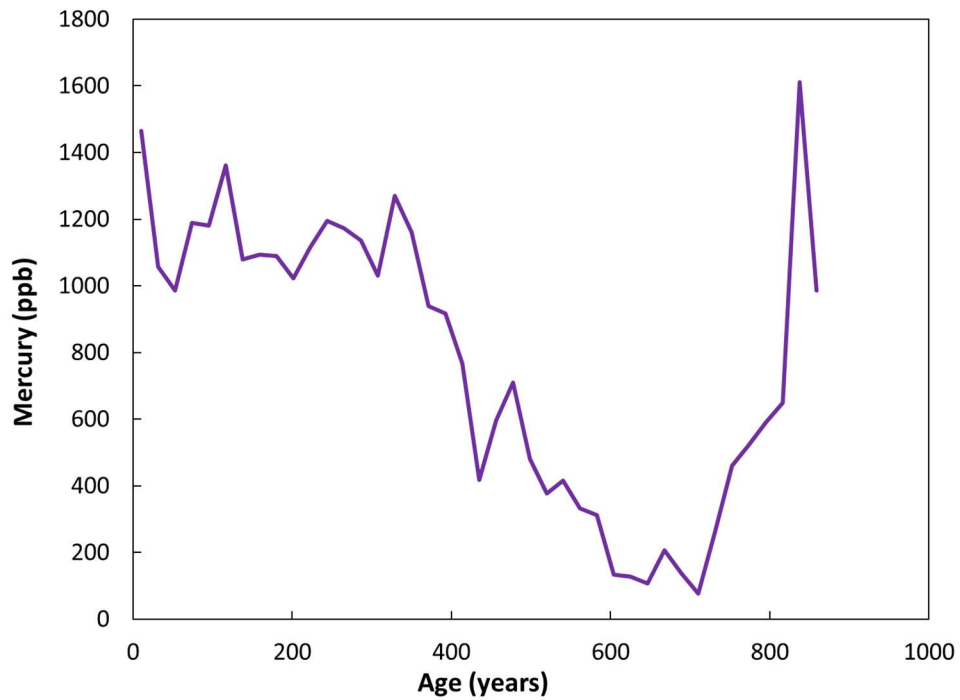
Figure 5.6. Hg content of sediments in core MEL1 (*top*) and core MEL2 (*bottom*), corrected for sedimentation rate using ^{210}Pb deposition rate for upper 15 cm of core MEL2 and tephrochronology-derived deposition rate for core MEL1 and the rest of core MEL2.

accumulation rate of 8.8 g m^{-2} yr $^{-1}$. Core MEL1 demonstrates an average MAR of 0.033 g cm^{-2} yr $^{-1}$ when the tephrochronology-derived linear sedimentation rate is used, but Hg content is much smaller. With the range of 0.1-1.5 ppm Hg and 1-6 wt% C, this accounts for a Hg accumulation rate of 0.026 mg Hg m^{-2} yr $^{-1}$ and a C accumulation rate of 7.9 g m^{-2} yr $^{-1}$ (Figure 5.7).

Over the 4.2 km^2 area of East Lake, this would account for a lake-wide burial rate of 8.3 kg Hg yr $^{-1}$ or an annual Hg input of 7.2 kg per year in the high flux zone (10% of lake area) and 1.1 kg per year in the rest of the lake. For the 6,500-year history of East Lake, this Hg store may be as large as 54.1 tonnes. The annual carbon burial rate across the whole lake is 70.1 tonnes C yr $^{-1}$, which should be considered as input in addition to the 6.7 t day^{-1} that is released as CO_2 gas.

The stores of Hg building up in East Lake sediments today could represent the first steps in the formation of an ore deposit along the lines of Sulphur Bank at Clear Lake, CA or Almadén, Spain. The Hg deposit at Clear Lake comprises 2,400 tonnes accumulated over 15,000 years, or 160 kg Hg yr $^{-1}$. The pathways for Hg-carrying thermal fluids to reach the surface were created by faulting and tectonic subsidence. Temporal variations in the Hg deposition rate are interpreted as changes in discharges from the underlying hydrothermal system (Varekamp and Waibel, 1987).

The fluxes of Hg from other volcanic sources are listen in table 5.2. East Lake exhibits a flux similar to that of Hawaii, another intracontinental plume volcano.
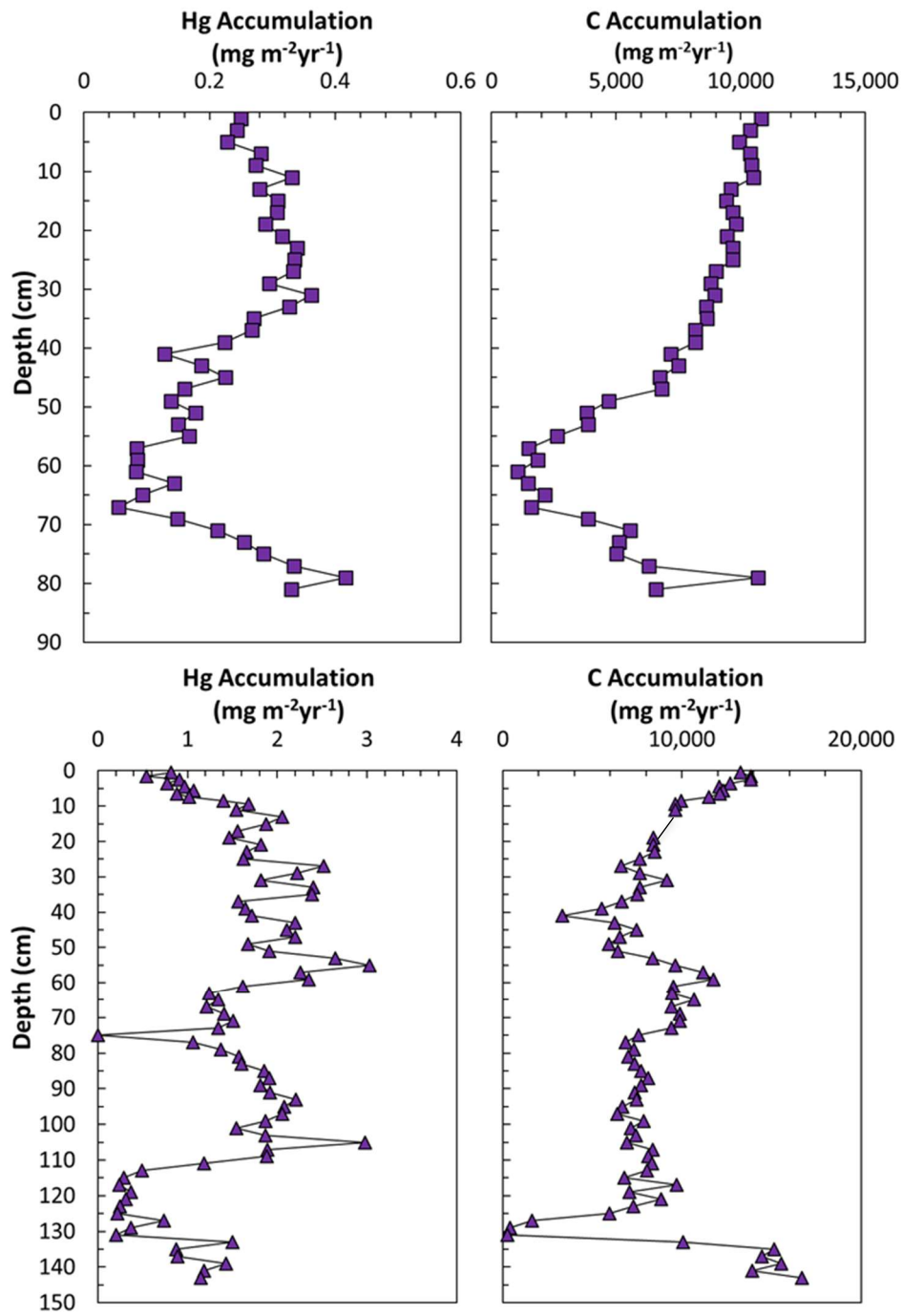
Figure 5.7. Annual mass accumulation rate of Hg and C for core MEL1 (*top*) and core MEL2 (*bottom*).

Location	Annual Hg Flux
Hawaii	1.5×10^{-3} Mg
Colima volcano, Mexico	0.44 Mg
Etna Volcano, Italy	2.7 Mg

Table 5.2. Local Hg emissions vary with volcano type and activity level (Varekamp and Buseck, 1986)

East Lake receives 1.5 kg Hg year^{-1} (at the calculated sedimentation rate of 1.1 mm/year) and 9,000 tonnes C per year (from SGS modeling of daily CO_2 flux). This gives a Hg:C ratio on the order of 10^{-7}. Murchison and Allende, two chondritic meteorites, have been measured for Hg and C and represent primordial solar system values. They carry Hg:C ratios on the order of 10^{-5} and 10^{-1}, respectively (Table 5.3). The lower ratios obtained from the Newberry plume may signify that the mantle has been enriched in C through recycling of subducted oceanic material, or that the mantle has been depleted in Hg due to its volatile state.

Source	Hg:C mass ratio
East Lake (this study)	4.6×10^{-7}
Murchison	15.9×10^{-6}
Allende	3.0×10^{-1}

Table 5.3. Ratio of Hg:C for this study and two chondritic meteorites. Chondritic meteorites are representative of undifferentiated mantle material (Lauretta et al., 2001,Van der Stap et al., 1986, Jarosewich, 1971)

5.5 Two-vector Hg model

Levels of Hg found in East Lake are extremely high by any means, given that natural unpolluted sediment usually carries between 50 and 100 ppb Hg In East Lake,

the bulk sediment of the lake carries 1,000-4,000 ppb Hg. In the high-flux area, the sediment holds 6,000-13,000 ppb Hg, with lower values in the ash-rich deposits.

Mercury is deposited in the high-flux area and across the rest of the lake floor by two different pathways, resulting in these two populations of concentrations and of MARs. In the lower concentration population, represented by core MEL1 (and cores from earlier studies), Hg is correlated with C_{org} and with S. In the higher concentration population, represented by core MEL2 and found near the high-flux zone, Hg is correlated with S but not with C_{org} (Figures 5.8, 5.9)
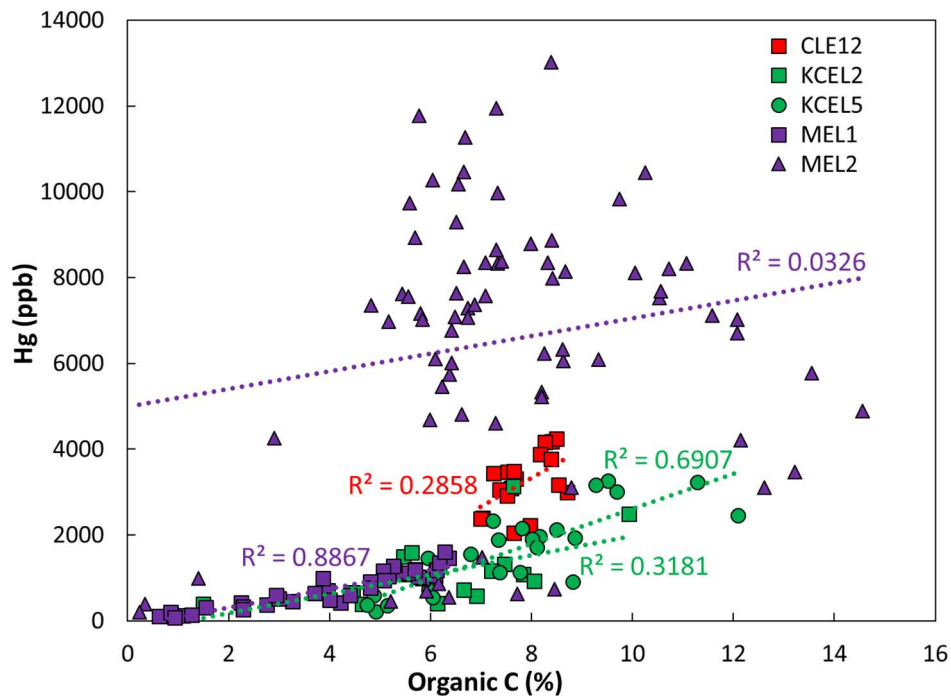
Figure 5.8. Comparison of C_{org} and Hg in East Lake sediment cores. Correlation coefficients vary but are lowest in core MEL2. Concentration of Hg is likely controlled by some phase other than C_{org}. C and Hg values for cores MEL1 and MEL2 (purple) are shown in Figure X, in addition to S values.
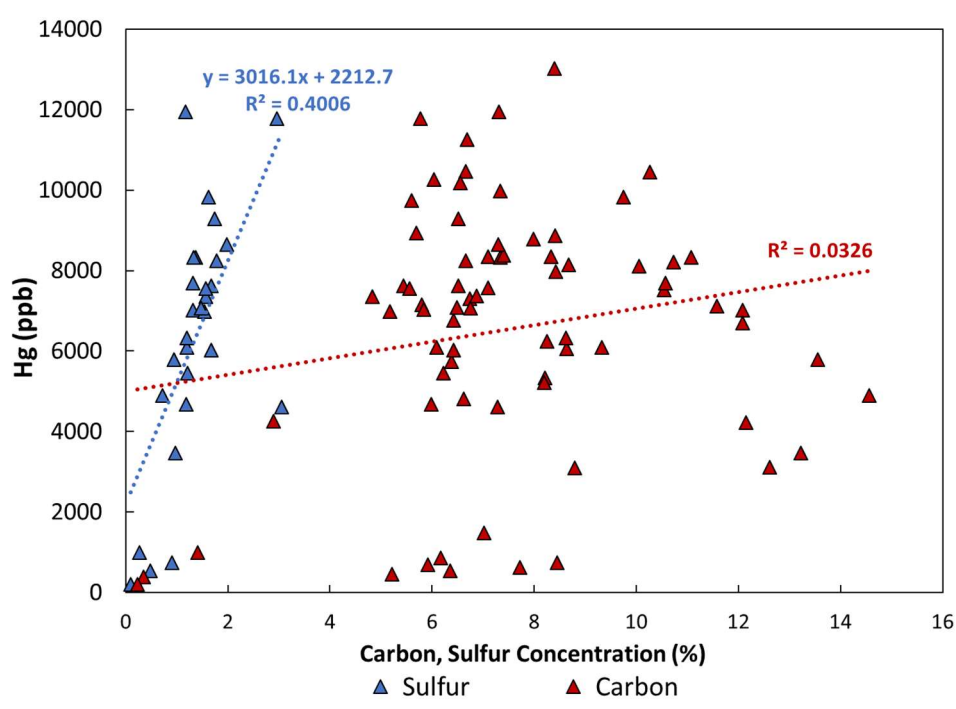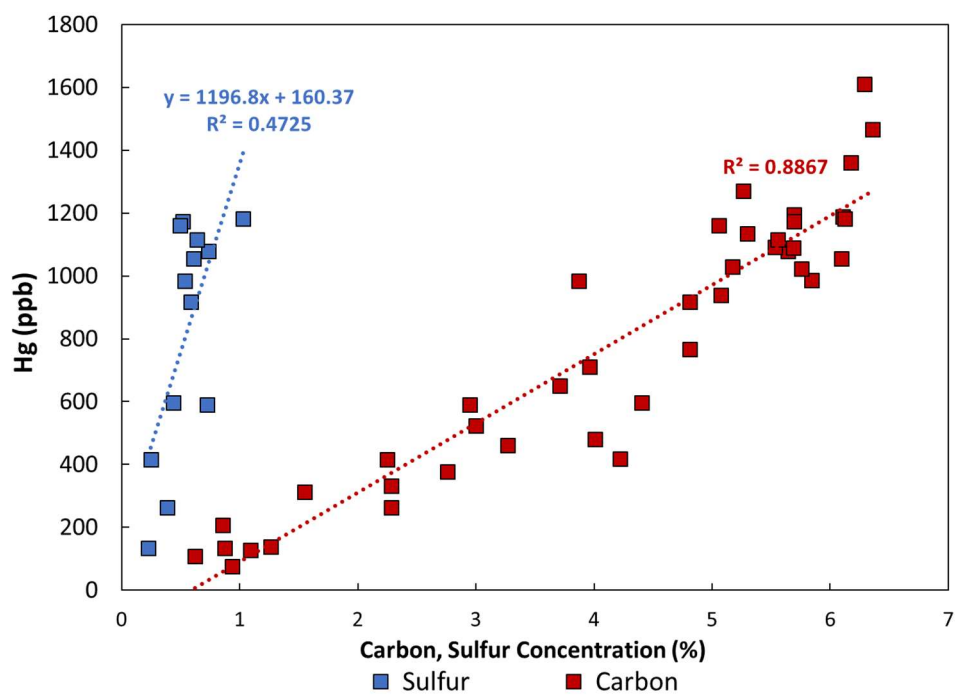
Figure 5.9. C and S concentration compared to Hg concentration in core MEL1 (top) and core MEL2 (*bottom*). Hg is poorly correlated to C in MEL2, but shows a better match to S. In core MEL1, Hg is correlated to both C and S.

When hydrothermal gases bearing Hg^0, H_2S, and CO_2 (and some fluid) enter the waters of East Lake at the high flux zone, they are exposed to oxygen, and their oxidized forms may be fixed as solid cinnabar or metacinnabar according to

$$Hg^0_{(aq)} + 0.5\ O_2 + H_2S \rightarrow HgS_{(s)} + H_2O$$
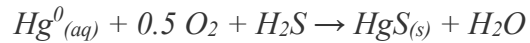
and those crystals will be incorporated in the sediment. Some Hg may also enter already in the oxidized form as bubble wall fluid, and may be fixed immediately in the sediment column as

$$Hg^{2+} + H_2S \rightarrow HgS_{(s)} + 2H^+$$
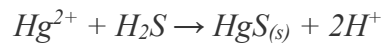
Some of this HgS_2 may be built into pyrite crystals, formed from Fe also present in the bubble wall fluid as

$$0.5\ Fe^{2+} + 0.5\ Hg^{2+} + 0.5\ O_2 + 2\ HS^- \rightarrow (Fe,Hg)S_2 + H_2O$$
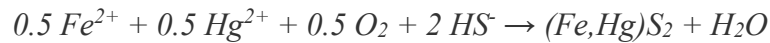
This fixed fraction of the Hg input will never move through the lake water (Pathway 1, Figure X). Hg and S that are oxidized but are not worked into sulfide crystals are now available to chemosynthetic bacteria that derive energy from reducing SO_4 and methylate Hg in the process as

$$Hg^{2+} + SO_4 \xrightarrow{bacteria} MeHg + H_2S$$
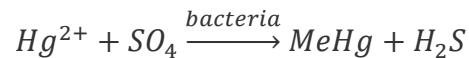
Both the methylated and oxidized forms of Hg are able to bind to C_{org} by ingestion or adsorption, respectively. Now bound to organic matter, this Hg will move through the lake until that material is deposited (Pathway 2, Figure 5.10).
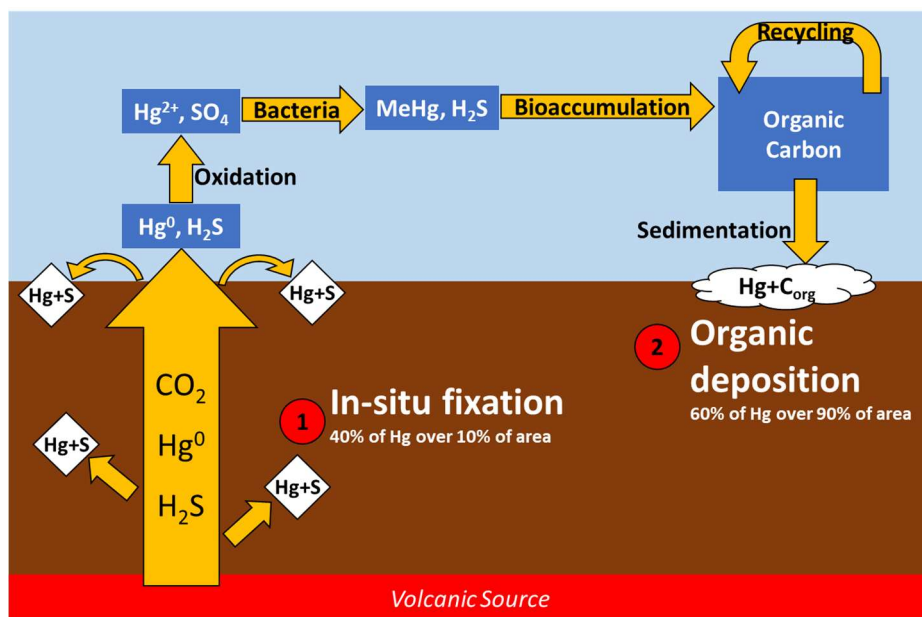
Figure 5.10. Two-vector Hg model. Incoming volcanic Hg may be (*1*) fixed to metal sulfides immediately in the sediment at very high concentrations or (*2*) cycle through the ecosystem and be deposited bound to C at a local "background" level.

In earlier years, dispersed bubbles have been seen at depth in East Lake on sonar, in areas besides the high flux zone. This could be an input of CO_2 and Hg on a much smaller scale and could allow for solid phase pyritization. In these instances, the amount of pyrite formed is controlled by the availability both of S and of some reducer. The reducer here is organic matter in the sediment here that converts SO_4 in the porewaters to H_2S, allowing for cinnabar precipitation throughout the lake. In this scheme, S and C_{org} would show a correlation that is not seen in precipitation in the high flux zone (Figure 5.11).
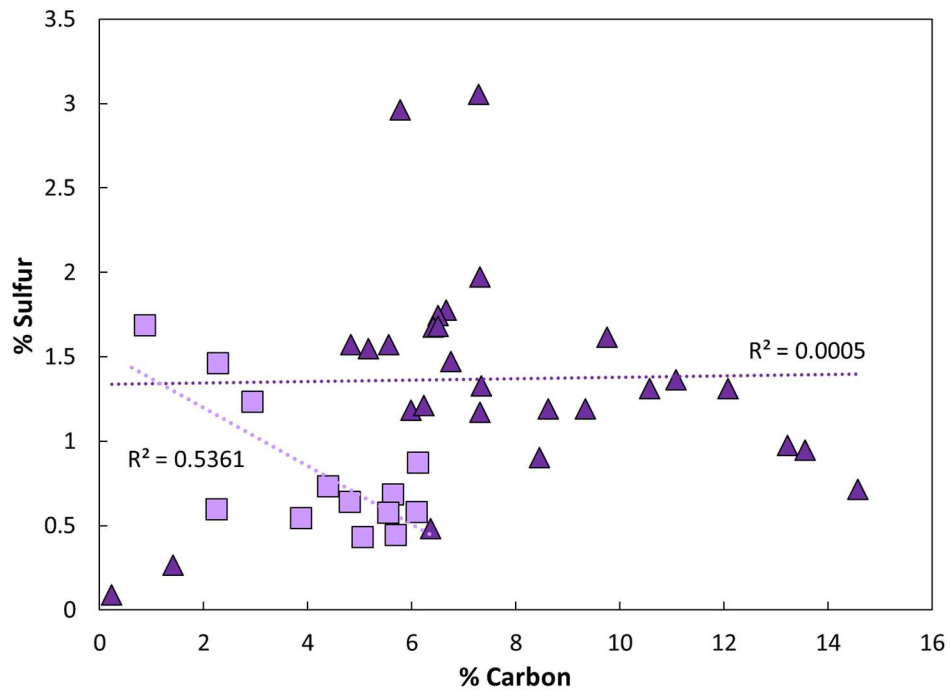
Figure 5.11. In core MEL1 (*light purple*), there is a negative correlation between C and S. No such correlation exists in core MEL2 (*dark purple*).

In the drowned crater area, 0.4-7.8 ng L^{-1} (10-35% of the total Hg) is in a methylated form, either particulate or dissolved (Figure 5.12). Methylation occurs by microbial processes in hypo- to anoxic conditions in these bottom waters and is then moved into the surface waters by diffusion and advection (Morel et al., 1998).

Near the high-flux area, 0.1-1.5 ng L^{-1} (0-15% of the total Hg) is methylated (Figure 5.12). Either this water is too shallow for proliferation of the methylating bacteria or because the MeHg is diluted by the abundance of incoming inorganic Hg. Additionally, the particulate fraction in this part of the lake is extremely large and particulate-bound Hg is unavailable to the organisms that carry out methylation. Alpers et al. (2005) suggest that a high concentration of dissolved organic carbon

(DOC) will lead to a higher rate of methylation as it keeps Hg in the dissolved phase so that it can be used in methylation reactions.

The residence time of Hg in East Lake waters is about 3.5 months (Table 5.4), which means that all the Hg that enters the lake (and is not immediately fixed as crystals in the sediment) is incorporated by organic matter in one season. This suggests that the Hg accumulated in each slice of sediment is indeed representative of the Hg that was input to the lake at that time.

Lacking from this Hg cycle model is any significant atmospheric input from above. Hg that is deposited usually enters a lake system already particulate-bound and is not available for the important methylation process exhibited in East Lake. Additionally, the flux from below is so great that any input from pollution is drowned out by the volcanic signal.

The methods in this project are only applicable under the assumption that all Hg entering the lake from the volcanic system below remains in the water column and sediments. While escape of Hg to the atmosphere would transform these calculated values to just minimum possible loads, there is no evidence for Hg escape from the surface. The vector for Hg escape that could indeed present a problem is that of the Hg taken up by fish at the top of the food chain and subsequently removed by fishermen.
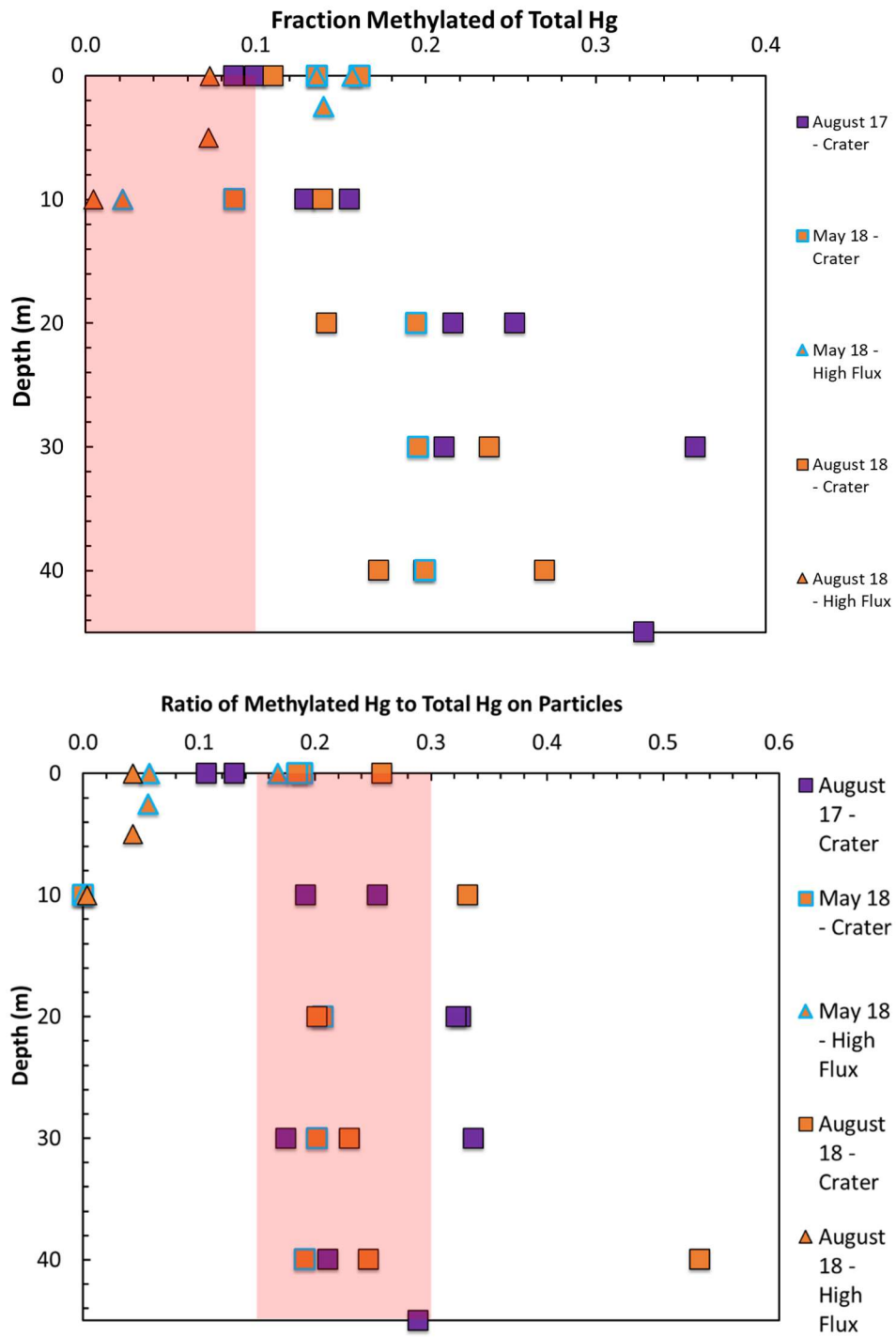
Figure 5.12. Fraction of total Hg in the water column that is methylated (top) and ratio of inorganic particulate Hg to methylated particulate Hg (bottom). Red box represents accepted typical (non-volcanic) lake values (Morel et al., 1998)

Concentration of Hg in water	6.07 ng L^{-1}
Volume of East Lake	86 x 10^6 L
Mass of Hg in water	0.52 g
Hg flux in/out (non-bubbling zone)	1.7 kg yr^{-1}
Residence time	0.31 years (*about 3.5 months*)

Table 5.4. Values used in the calculation of residence time of Hg in East Lake.

Conclusions

East Lake has substantial volcanic gas input from the subsurface of Newberry volcano, consisting of CO_2, H2S and Hg^0. The CO2 largely dissolves in the water and then is largely vented through diffusive degassing at the surface. A small area near the beach hotsprings has zones with intense bubbling at the surface and a smell of H2S. The measured CO2 fluxes vary over the season, with the highest fluxes directly after ice melting in late april early may and then decrease over the summer to reach close to steady state values near the fall. During the frozen over winter period, little or no CO2 escapes from the lake. Organic carbon in the lake also forms from the volcanic CO2, but the Corg accumulation rates are very small compared to the CO2 surface gas fluxes. Data from the last few years suggest that the overall lake is in steady state wrt CO2 and the residence time of carbon in the lake is short at < 1 year. The water residence time is >20 years, so clearly the carbon cycle and water cycle are decoupled. The year round volcanic CO2 input is estimated at ~ 25 tonnes CO2/day, whereas the surface fluxes range from zero in winter, ~ 100 tonnes in early May and close to 25 in the fall. The carbon extraction occurs largely in the surface waters while the input is at the lake bottom. The coupling over depth through, diffusion, bubble transport and water mixing processes that resupply CO2 to the surfae water layer are not well knowns. The SO4 in the water is supposedly the result of oxidized H2S which may return to the sediment as FeS2 during diagenesis.

The Hg cycle in the lake is very different from the CO2 cycle. We assumed that the Hg enters the lake with the CO2 bubbles as Hgo gas, which may be oxidized

to Hg2+ once it dissolves in the lake waters. A complex pathway of methylation, Hg2+ adsorption and ecosystem processing creates top of the food chain fish with close to 3 ppm Hg. Most of the sediment has Hg concentrations between 1-3 ppm, and the Hg correlates strongly with sediment organic content. This is a conventional Hg pathway, described from many lakes where the methylated Hg forms enter the ecosystem progress up the food chain, and waste products (dead organic matter, fish poo) become part of the sediment bed. The bubbly zone has sediment with up to 13 ppm Hg and the Hg abundances correlate here with sulfur, suggesting a different Hg pathway into the sediment. A variety of reactions can be proposed to fix Hg into pyrite, either at the water-sediment interface or in the sediment bed.

In the identified "high-flux zone" in the southeast corner of the lake, Hg values in the water reach 100s of ng L^{-1}. This highly altered zone is where the volcanic gas input is focused and about 40% of the Hg input is fixed locally in the sediment. Through the rest of the lake, Hg values are 3-8 ng L^{-1} in the water, with high % of methylated Hg.

Mercury values in the East Lake waters and sediments are extremely high relative to natural background levels, and even relative to areas affected by regional pollution. [Report burial rates here and total conetnts, repeat the C/Hg value of primitive earth,)However, these levels do put Newberry within the expected range of an intraplate plume volcano. The CO_2 flux out of East Lake is also comparable to other global volcanic lakes of similar area.

This work demonstrates the importance of studying the seasonal processes in a volcanic lake before it can be utilized for longer-term volcanic monitoring. While release of gases such as Hg and CO_2 are extremely useful signals of activity below the surface, they cannot be meaningfully used without a pre-existing framework for changes in those fluxes throughout the year.

This work also identifies important nuances to consider when calculating a global flux. While no measurable Hg is evaded from the East Lake surface, it is clear significant amounts are introduced to the surface environment from below. Fluxes of Hg such as this one at Newberry – where it is never seen in the atmosphere but still added to the hydrosphere and biosphere – must be closely considered to build a true global Hg flux model.

References

Alpers, C.N., Hunerlach, M.P., May, J.T., Hothem, R.L., 2005, Mercury contamination from historical gold mining in California, Publications of the US Geological Survey, 61.

Andrade, C., Viveiros, F., Cruz, J.V., Coutinho, R., Silva, C., 2016, Estimation of the CO_2 flux from Furnas volcanic lake (Sao Miguel, Azores), Journal of volcanology and geothermal research, v. 315, p. 51-64.

Bagnato, E., Viveiros, F., Pacheco, J.E., D'Agostino, F., Silva, C., and Zanon, V., 2018, Hg and CO2 emissions from soil diffuse degassing and fumaroles at Furnas Volcano (Sao Miguel Island, Azores): gas flux and thermal energy output, Journal of Geochemical Exploration, v. 190, p. 39–57.

Beachly, M.W., Hooft, E.E.E., Toomey, D.R., Waite, G.P., 2012, Upper crustal structure of Newberry Volcano from P-wave tomography and finite difference waveform modeling, Journal of Geophysical Research, v. 117, 17 pp.

Brumberg, H., Capece, L., Wagner, S.M., Tartell, P., Smith, C., Cauley, C., Varekamp, J.C., *unpublished manuscript,* East Lake, Newberry, OR: A geophytic volcanic lake degassing CO_2

Burton, M.R., Sawyer, G.M., Granieri, D., 2013, Deep carbon emissions from volcanoes: Reviews in Mineralogy and Geochemistry, v. 75, p. 323-354

Caracausi, A., Martelli, M., Niccion, P.M., Paternoster, M., Stuart, F.M., 2013, Active degassing of mantle-derived fluid: A geochemical study along the Vulture line, southern Apiennines (Italy), Journal of Volcanology and Geothermal Research, v. 253, p. 65-74.

Cardellini, C., Chiodini, G., Frondini, F., 2003, Application of stochastic simulation to CO_2 flux from soil: Mapping and quantification of gas release, Journal of Geophysical Research, v. 108, 13 pp.

Casadevall, T.J., Rose, W.I., Gerlach, T.M., Greenland, L.P., Ewert, J., Wundermand, R., Symonds, R., 1983, Gas emissions and the eruptions of Mount St. Helens through 1982, Science, v.221, p. 1383-1385.

D'Alessandro, W., Giammanco, S., Perallo, F., 1997, CO_2 output and $d^{13}C(CO_2)$ from Mount Etna as indicators of degassing of shallow asthenosphere: Bulletin of Volcanology, v. 58, p. 455-458.

Delemelle, P., Bernard, A., 1999, Volcanic Lakes, *in* Encyclopedia of Volcanoes, Sigurdsson, H., *ed*, p. 877-896.

Domagalaski, J., Majewski, M.S., Alpers, C.N., Eckley, C.S., Eagles-Smith, C.A., Schenk, L., Wherry, S., 2016, Comparison of mercury mass loading in streams to atmospheric deposition in watersheds of North America: Evidence for non-atmospheric mercury sources, Science of the Total Environment, v. 568, p. 638-650.

Eagles-Smith, C.A., Wiener, J.G., Eckley, C.S., Willacker, J.J., Evers, D.C., YEAR, Mercury in western North America: A synthesis of environmental contamination, fluxes, bioaccumulation, and risk to fish and wildlife, Science of the Total Environment, v. 568, p. 1213-1226.

Engle, M.A., Gustin, M.S., Goff, F., Counce, D.A., Janik, C.J., Bergfeld, D., Rytuba, J.J., 2006, Atmospheric mercury emission from substrates and fumaroles associated with three hydrothermal systems in the western United States: Journal of Geophysical Research, v. 111, 16 pp.

Evans, W.C., Sorey, M.L., Cook, A.C., Kennedy, B.M., Shuster, D.L., Colvard, E.M., While, L.D., Huebner, M.A., 2002, Tracing and quantifying magmatic carbon discharge in cold groundwaters: lessons learned from Mammoth Mountain, USA, Journal of Volcanology and Geothermal Research, v. 114, p. 291-312.

Faure, G., 1998, Principles and applications of Geochemistry: a comprehensive textbook for geology students (second edition).

Fleck, J.A., Marvin-DiPasquale, M., Eagles-Smith, C.A., Ackerman, J.T., Lutz, M.A., YEAR, Mercury and methylmercury in aquatic sediment across western North America: Science of the Total Environment, v. 568, p. 727-738.

Gee, A., 1986, Heavy metals in the Connecticut River estuary: analysis and questions of approach [BA thesis]: Wesleyan University.

Gerlach, T.M., Westrich, H.R., Symonds, R.B., 1996, Pre-eruptions vapour in magma of the climactic Mount Pinatubo Eruption: source of the giant stratospheric sulphur dioxide cloud, *in* Fire and Mud: Eruption and lahaars of Mount Pinatubo, Phillipnes, Newhall, C.G., Punongbayan, RS., *eds*, Philippine Institude of Volcanology and Seismology, p. 415-433.

Gerlach, T.M., Doukas, M.P., McGee, K.A., Kessler, R., 2001, Soil efflux and total emission rates of magmatic CO_2 at the Horseshoe Lake tree kill, Mammoth Mountain, California, 1995-1999, Chemical geology, v. 177, p. 101-116.

Hards, V., 2005, Volcanic contributions to the global carbon cycle: British Geological Survey Occasional Publication, no. 10, 26 pp.

Holmes CD, Jacob DJ, Soerensen AL, Corbitt ES, 2010, Global atmospheric budget of mercury including oxidation of Hg(0) by bromine atoms: Geochimica et Cosmochimica Acta, v. 74, p. A413– A413.

Jarosewich, E., 1971, Chemical Analysis of the Murchison Meteorite: Meteoritics, v. 6, p. 49.

Krabbenhoft, D.P. and Sunderland, E.M., 2013, Global change and mercury: Science, v. 341, p. 1457-1458.

Kuehn, S.C. and Foit, F.F., 2000, Silicic Tephras of Newberry Volcano, in Jensen, R.A., and Chitwood, L.A., eds, What's New at Newberry Volcano, Oregon: Guidebook for the Friends of the Pleistocene Eighth Annual Pacific Northwest Cell Field Trip, pp. 135-163.

Lauretta, D.S., Klaue, B., Blum, J.D., Buseck, P.R., 2001, Mercury abundances and isotopic compositions in the Murchison (CM) and Allende (CV) carbonaceous chondrites, Geochimica et Cosmochimica Acta, v. 65, p. 2807–2818.

Lekowitz, J.N., 2012, A Tale of Two Lakes: The Newberry Twin Crater Lakes, OR. [BA thesis]: Wesleyan University

Lefkowitz, J.N., Varekamp J.C., Reynolds R.W. and Thomas E., 2016, A tale of two lakes: the Newberry Volcano twin crater lakes, Oregon, USA, *in* Geochemistry and Geophysics of Active Volcanic Lakes: Geological Society of London, Special Publication, 437.

MacLeod, N.S., Sherron, D.R., 1988, Geologic evidence for a magma chamber beneath Newberry Volcano, Oregon: Journal of Geophysical Research, v. 93, p. 10,067-10,079.

Mazot, A., Bernard, A., 2015, CO_2 degassing from volcanic lakes: D. Rouwet et al. (eds), Volcanic Lakes, Advances in volcanology, Springer

Mazot, A., Taran, Y., 2009, CO_2 flux from the volcanic lake of El Chichon (Mexico), Geofisica Internacional, v. 48, p. 73-83.

Meyers, P.A., 1994, Preservation of elemental and isotopic source identification of sedimentary organic matter, Chemical Geology, v. 114, p. 289-302

Morel, F.M.M., Kraepiel, A.M.L., and Amyot, M., 1998, The chemical cycle and bioaccumulation of Mercury. Annual Review of Ecology and Systematics Vol. 29:543-566 (Volume publication date November 1998) https://doi.org/10.1146/annurev.ecolsys.29.1.543

Nittrouer, C.A., Sternberg, R.W., Carpenter, R., Bennett, J.T., 1979, The use of Pb-210 geochronolgy as a sedimentological tool, *in* Application to the Washington continental shelf: Marine Geology, v. 31, p. 297-316.

Pasternack, G.B., Varekamp, J.C., 1997, Volcanic lake systematics I. Physical constraints, Bulletin of Volcanology, v. 58, p. 528-538.

Perez, N.M., Hernandez, P.A., Padilla, G., Nolasco, D., Barrancos, J., Melian, G., Padron, E., Dionis, S., Calvo, D., Rodriguez, F., Notsu, K., Mori, T., Kusakaba, M., Arpa, M.C., Reniva, P., Ibarra, M., 2011, Global CO_2 emission from volcanic lakes, Geology, v. 39, p 235-238.

Pierrot, D. E. Lewis,and D. W. R. Wallace. 2006. MS Excel Program Developed for CO2 System Calculations. ORNL/CDIAC-105a. Carbon Dioxide Information Analysis Center, Oak Ridge National Laboratory, U.S. Department of Energy, Oak Ridge, Tennessee.

Phelps, D., Buseck, P.R. 1980. Distribution of soil mercury and the development of soil mercury anomalies in the Yellowstone geothermal area, Wyoming. Economic Geology 75, 730-741.

Pyle, D.M., Mather, T. A., 2003, The importance of volcanic emissions for the global atmospheric mercury cycle,Atmospheric Environment 37, 5115-5124.

Ramlal, P.S., Kelly, C.A., Rudd, J.W.M., Furutani, A., 1993, Sites of methyl mercury production in remote Canadian shield Lakes: Canadian Jounal of Fisheries and Aquatic Sciences, v. 50, p. 972-979

Rizzo, A.L., Caracausi, A., Chavagnac, V., Nomikou, P., Polymenakou, P.N., Mandalakis, M., Kotoulas, G., Magoulas, A., Castillo, A., Lampridou, D., Marusczak, N., Sonke, J.E., 2019, Geochemistry of CO_2-rich gases venting from submarine volcanism: The case of Kolumbo (Hellenic Volcanic Arc, Greece), Frontiers in Earth Science, v. 7, 20 pp.

Schmincke, H.U., Volcanism, 2004, Springer

Smith, C. N., 2010, Isotopic geochemistry of mercury in active and fossil hydrothermal systems. PhD Dissertation, University of Michigan, Ann Arbor, MI.

Ullrich, S.M., Tanton, T.W., Abdrashitova, S.A., 2001, Mercury in the aquatic environment: A review of factors affecting methylation, Critical Reviews in Environmental Science and Technology, v. 31, p. 241-293.

USEPA, 2001. Method 1630 Methyl Mercury in Water by Distillation, Aqueous Ethylation, Purge and Trap, and CVAFS, Draft January 2001.

USEPA, 2005, Human Health Risk Assessment Protocol for Hazardous Waste Combustion Facilities, Multimedia Planning and Permitting Division, Center for Combustion Science and Engineering

USGS, 1999, Collection of water samples, Wilde, F.D., Radtke, D.B., Gibs, J., and Iwatsubo, R.T., *eds*: USGS—TWRI Book 9, Chapter A4.

Van Der Stap, C.A.H., Heylann, D., Vis, R.D., Verheul, H., 1986, Mapping of carbon concentrations in the Allende Meteorite with the $^{12}C(d,p)^{13}C$ method, Journal of Geophysical Research, v. 91, p. D373-D377.

Varekamp, J.C., Buseck, P.R., 1981, Mercury emissions from Mount St Helens during September 1980, Nature 293, 555–556.

Varekamp, J.C., Buseck, P.R., 1984a, Changing mercury anomalies in Long Valley, California: Indication for magma movement or seismic activity, Geology, v. 15, p. 283-286.

Varekamp, J.C., Buseck, P.R., 1984b, The speciation of mercury in hydrothermal systems, with applications to ore deposition, Geochimica et Cosmochinica Acta, v. 48, p. 177-185.

Varekamp, J.C., Buseck, P.R., 1986, Global mercury flux from volcanic and geothermal sources, Applied Geochemistry 1, 65-73.

Varekamp, J.C., Waibel, A.F., 1987, Natural cause for mercury pollution at Clear Lake, California, and paleotectonic inferences. Geology 15, 1018-1021.

Varekamp, J.C., Pasternack, G.B., Rowe Jr., G.L., 2000, Volcanic lake systematics II. Chemical constraints, Journal of Volcanology and Geothermal Research, v. 97, p. 161-179.

Varekamp, J.C., Caldwell, S., Capece, L., Horne, J., Upin, H., 2016, The Newberry Crater Lakes, Oregon: Learning Science Through Research, Keck Geology Consortium, v. 29,

West Instruments, 2012, Portable diffuse flux meter with LI-COR CO2 detector. Handbook. Italy.

Werner, C., Brantley, S., 2003, CO_2 emissions from the Yellowstone volcanic system: Geochemistry Geophysics Geosystems, v. 4.

White, D.E., Muffley, L.J.P., Truesdell, A.H., 1971, Vapor-dominated hydrothermal systems compared with hot-water systems: Economic Geology, v. 66, p. 75-97.

Appendices

East Lake 2017, 2018 sample IDs, types, collection dates, and coordinates. Sediment core depths given as core length. Grab sample depths given as water depth at that location.

Sample ID	Type	Length/ Depth(s)	Date Collected	Lat.	Long.
MEL1	Core	81 cm	8/28/17	43.733722	-121.20840
MEL2	Core	143 cm	8/28/17	43.723298	-121.20377
CMPELW1	Water profile	0-30 m	8/24/17	43.73363	-121.20685
CMPELW2	Water profile	0-50 m	8/25/17	43.73320	-121.20871
CMPW3	Hg Water profile	0-45 m	8/26/17	43.7306	-121.20972
CMPW4	Hg Water profile	0-30 m	8/26/17	43.72603	-121.21147
CMPLAG1	Lagoon water	0 m	8/22/17	43.72777	-121.22499
Aug 17 Background (1)	YSI Profile	0-5 cm	8/22/17	43.72976	-121.20389
Aug 17 Crater	YSI Profile	0-28.5 m	8/22/17	43.73077	-121.20530
Aug 17 Background (2)	YSI Profile	0-28.5 m	8/22/17	43.72743	-121.21275
Sept 17	Yellow Box Profile	0-43.3 m	9/24/17	43.72996	-121.20838
JEEL1	Water profile	0-40 m	9/24/17	43.72996	-121.20838
JEEL2	Surface water	0 m	9/24/17		
MTELW1	Surface water; grab sample	0 m; 0 cm	5/24/18	43.72239	-121.20440
MTELW2	Water profile	0-40 m	5/24/18	43.73272	-121.20960
MTELW3	Water profile; SAV, grab sample	0-10 m; 0 cm	5/27/18	43.72468	-121.20306
MTELW4	Water profile; SAV, grab sample	0-2.5 m; 0 cm	5/27/18	43.72089	-121.20370

May 18 High Flux (1)	YSI Profile	0-8 m	5/24/18	43.72239	-121.20440
May 18 Crater	YSI Profile	0-30 m	5/24/18	43.73272	-121.20960
May 18 High Flux (2)	YSI Profile	0-11 m	5/27/18	43.72468	-121.20306
May 18 High Flux (3)	YSI Profile	0-2 m	5/27/18	43.72089	-121.20370
MCELW1	Water profile	0-40 m	8/15/18	43.73361	-121.20670
MCELW2	Water profile	0-5 m	8/16/18	43.72111	-121.20560
MCELW3	Hg bottom water	40 m	8/16/18	43.73306	-121.20580
MCELW4	Hg bottom water	40 m	8/16/18	43.73278	-121.20830
MCELW5	Hg bottom water	10 m	8/16/18	43.72472	-121.20310
MCELHS	Hot springs water	0 m	8/17/18	43.71965	-121.20451
MCELG1	Pore water	0 cm	8/16/18	43.72472	-121.20310
MCELG2	Pore water, grab sample	0 cm	8/16/18	43.72583	-121.21470
MCELG3	Grab sample	0 cm	8/16/18	43.72278	-121.21610
MCELG4	Grab sample	0 cm	8/16/18	43.72222	-121.21720
MCELG5	Grab sample	0 cm	8/19/18	43.732631	-121.19655
MCELG6	Grab sample	0 cm	8/21/18	43.73028	-121.14183
MCELG7	Grab sample	0 cm	8/21/18	43.72412	-121.20387
MCELG8	Grab sample	0 cm	8/21/18	43.72072	-121.20237
MELF	Plankton net	n/a	8/16/18	n/a	n/a
Aug 18 Crater (1)	YSI Profile	0-30 m	8/21/18	43.72968	-121.21206
Aug 18 High flux	YSI Profile	0-14 m	8/21/18	43.72412	-121.20387
Aug 18 Crater (2)	Yellow Box Profile	0-39 m	8/19/18	43.72820	-121.21007

CO_2 flux measurements, 2015-2018

June 2015			June 2016		
Mol m^{-2} day^{-1}	Lat (N)	Long (W)	Mol m^{-2} day^{-1}	Lat (N)	Long (W)
0.0361	43.72342	-121.20913	0.0034	43.72143	-121.2185
0.0391	43.71945	-121.21127	0.0179	43.72415	-121.208
0.0450	43.72328	-121.2183	0.0421	43.72471	-121.2212
0.0460	43.72867	-121.2103	0.0570	43.72263	-121.2202
0.0511	43.7306	-121.20663	0.0795	43.72087	-121.2072
0.0562	43.72232	-121.20827	0.0827	43.72042	-121.2114
0.0588	43.7302	-121.21256	0.1107	43.7287	-121.2217
0.0613	43.72209	-121.21072	0.1269	43.72448	-121.1973
0.0742	43.72446	-121.19607	0.1574	43.73132	-121.2225
0.0811	43.72196	-121.20003	0.1648	43.7332	-121.2216
0.0865	43.72062	-121.20393	0.1676	43.73513	-121.2243
0.1006	43.7211	-121.20331	0.1827	43.7264	-121.2027
0.1068	43.72833	-121.20961	0.1950	43.72066	-121.2145
0.1087	43.73364	-121.21501	0.2030	43.7263	-121.2053
0.1151	43.72762	-121.20936	0.2315	43.73458	-121.2258
0.1159	43.7298	-121.20277	0.2345	43.7273	-121.2091
0.1398	43.72214	-121.20051	0.2363	43.73321	-121.2258
0.1503	43.73156	-121.21034	0.2373	43.72587	-121.2001
0.1653	43.72049	-121.20618	0.2471	43.72911	-121.2124
0.1663	43.72589	-121.20336	0.2573	43.72368	-121.197
0.1677	43.72227	-121.20977	0.2634	43.7325	-121.2247
0.1792	43.73355	-121.21342	0.2794	43.72428	-121.2023
0.1856	43.72076	-121.2168	0.2852	43.72382	-121.2023
0.1973	43.72037	-121.20558	0.2905	43.72498	-121.1977
0.2005	43.72833	-121.2016	0.2907	43.72732	-121.2202
0.2083	43.72143	-121.19213	0.2910	43.72383	-121.1978
0.2273	43.73237	-121.20128	0.3051	43.73051	-121.2147
0.2314	43.72031	-121.20044	0.3156	43.72561	-121.1995
0.2538	43.7301	-121.21466	0.3174	43.72481	-121.201
0.2570	43.72115	-121.20188	0.3245	43.72308	-121.2029
0.2675	43.72092	-121.20254	0.3388	43.73155	-121.2169
0.2681	43.72063	-121.19903	0.3566	43.724	-121.199
0.2858	43.73352	-121.20117	0.3579	43.72145	-121.201
0.2994	43.73414	-121.21545	0.3681	43.72868	-121.2008
0.3251	43.72087	-121.20256	0.3717	43.7251	-121.2001
0.4253	43.73326	-121.21275	0.3745	43.72611	-121.2003

0.4269	43.72075	-121.20146
0.4562	43.72091	-121.20147
0.9014	43.72329	-121.21829

0.3783	43.73128	-121.1992
0.3798	43.73066	-121.1997
0.3837	43.72718	-121.2006
0.3994	43.72244	-121.2032
0.4047	43.7232	-121.2003
0.4214	43.72428	-121.2002
0.4363	43.73003	-121.1999
0.4390	43.72308	-121.1996
0.4538	43.72239	-121.1991
0.4544	43.72807	-121.2002
0.4600	43.72436	-121.1996
0.4698	43.72242	-121.1974
0.4808	43.72268	-121.1979
0.4883	43.72008	-121.2018
0.5473	43.72367	-121.1978
0.7674	43.7202	-121.2024
0.8659	43.72154	-121.2031
1.6079	43.72052	-121.1999
3.4684	43.72006	-121.2005

August 2017		
Mol m^{-2} day^{-1}	Lat (N)	Long (W)
0.0242	43.73295	-121.2278
0.0274	43.73438	-121.2264
0.0276	43.73397	-121.2273
0.0283	43.73415	-121.2257
0.0295	43.73446	-121.2256
0.0405	43.73338	-121.2256
0.0527	43.72556	-121.2165
0.0541	43.72766	-121.2163
0.0578	43.72974	-121.2157
0.0611	43.73255	-121.2274
0.0616	43.73354	-121.2276
0.0618	43.73367	-121.2247
0.0680	43.73209	-121.2276
0.0754	43.73269	-121.2265
0.0787	43.72233	-121.2196
0.0873	43.72007	-121.2159
0.0924	43.72956	-121.2136
0.0940	43.72021	-121.2186

May 2018		
Mol m^{-2} day^{-1}	Lat (N)	Long (W)
0.1105	43.72809	-121.21931
0.1379	43.73021	-121.21933
0.1394	43.73207	-121.21494
0.1443	43.72657	-121.21951
0.2038	43.72701	-121.2168
0.2302	43.72372	-121.20913
0.2383	43.73233	-121.22124
0.2825	43.72369	-121.21361
0.3069	43.73497	-121.21866
0.3110	43.73023	-121.21396
0.3381	43.73166	-121.21253
0.3430	43.72557	-121.20312
0.3701	43.72301	-121.21655
0.3750	43.72185	-121.21386
0.3807	43.72145	-121.21753
0.4068	43.72134	-121.21032
0.4092	43.73395	-121.20564
0.4211	43.72971	-121.20931

0.1127	43.73068	-121.203	0.4499	43.72703	-121.21271
0.1150	43.7198	-121.2117	0.4848	43.72536	-121.19899
0.1169	43.72305	-121.1985	0.5022	43.72292	-121.20078
0.1240	43.73079	-121.2148	0.5047	43.72002	-121.21305
0.1293	43.72197	-121.1975	0.5136	43.72936	-121.20229
0.1304	43.7308	-121.2165	0.5179	43.7347	-121.2217
0.1345	43.72374	-121.2182	0.5262	43.72677	-121.20844
0.1403	43.73027	-121.2011	0.5281	43.7202	-121.21832
0.1443	43.72972	-121.2167	0.5542	43.72735	-121.20076
0.1543	43.73219	-121.1997	0.5592	43.7243	-121.21783
0.1724	43.72533	-121.2021	0.5863	43.73315	-121.20274
0.1865	43.72642	-121.2025	0.6144	43.72238	-121.21979
0.1911	43.72922	-121.2019	0.6189	43.72084	-121.20148
0.1952	43.73037	-121.199	0.6272	43.72885	-121.20531
0.2006	43.73313	-121.2028	0.6451	43.73154	-121.20448
0.2018	43.72872	-121.2131	0.6542	43.73123	-121.20754
0.2069	43.72709	-121.2073	0.6949	43.72007	-121.20536
0.2079	43.72925	-121.2046	0.6950	43.72535	-121.20479
0.2097	43.7274	-121.2023	0.7385	43.72225	-121.19756
0.2177	43.72928	-121.2075	0.7575	43.72191	-121.20587
0.2255	43.73351	-121.2048	0.7603	43.72867	-121.19823
0.2295	43.7257	-121.208	0.7842	43.72585	-121.19667
0.2315	43.72467	-121.2015	0.8264	43.73034	-121.20082
0.2328	43.72344	-121.1982	0.9690	43.73413	-121.20894
0.2334	43.72062	-121.2059	0.9822	43.73464	-121.21587
0.2364	43.72562	-121.2021			
0.2366	43.7251	-121.2014			
0.2414	43.73269	-121.207	**August 2018**		
0.2414	43.73134	-121.2075	**mol/m2/day**	**Lat (N)**	**Long (W)**
0.2540	43.72051	-121.2009	0.0001	43.73209	121.19908
0.2723	43.72432	-121.2019	0.0164	43.73326	121.22731
0.2782	43.72689	-121.2021	0.0178	43.73411	121.22404
0.3083	43.72972	-121.2031	0.0237	43.72848	121.22091
0.3090	43.72491	-121.1987	0.0247	43.73235	121.21986
0.3391	43.72652	-121.2077	0.0304	43.73227	121.21147
0.3531	43.72592	-121.1995	0.0336	43.72911	121.21167
0.3580	43.73402	-121.2066	0.0407	43.73444	121.22031
0.3704	43.73262	-121.2014	0.0449	43.73248	121.21599
0.3737	43.7254	-121.1991	0.0494	43.73528	121.20724
0.3743	43.7213	-121.2072	0.0532	43.73538	121.21678
0.3804	43.7277	-121.1971	0.0597	43.73199	121.22385

0.3899	43.72393	-121.2076	0.0612	43.73397	121.21081
0.4043	43.72272	-121.2012	0.0659	43.72984	121.20678
0.4110	43.72606	-121.2009	0.0712	43.72462	121.21911
0.5082	43.72319	-121.2075	0.0754	43.73376	121.20444
0.5276	43.72563	-121.1996	0.0797	43.72936	121.21637
0.5596	43.72088	-121.2074	0.0932	43.72536	121.21517
0.5981	43.72214	-121.202	0.0985	43.73281	121.20782
0.6423	43.7238	-121.198	0.1036	43.73080	121.20272
0.7251	43.72336	-121.198	0.1077	43.72672	121.20550
0.7551	43.7243	-121.1984	0.1163	43.72660	121.21008
0.7554	43.723	-121.1985	0.1230	43.72150	121.21515
0.7696	43.72217	-121.2	0.1243	43.72909	121.19863
0.8182	43.72334	-121.1991	0.1391	43.73502	121.20116
0.8547	43.72306	-121.2037	0.1957	43.72060	121.21015
0.9069	43.72061	-121.2026	0.2121	43.72374	121.20972
0.9686	43.72263	-121.1987	0.2627	43.72469	121.20209
0.9807	43.72331	121.19845	0.7586	43.72203	121.19912
0.9964	43.72182	-121.1997	0.8773	43.72257	121.20535
1.0717	43.72228	-121.1989	0.9656	43.72052	121.20296
1.1028	43.72051	-121.2035	0.9693	43.72609	121.19851
1.1084	43.72263	-121.2031			
1.1138	43.7207	-121.1989			
1.1701	43.7231	-121.198			
1.1710	43.72188	-121.1989			
1.1937	43.72281	121.19888			
1.2215	43.72232	121.1993			
1.2294	43.72425	-121.1989			
1.4689	43.72207	-121.1982			

Raw Hg in water data, 2017 and 2018

	Total Hg (ng/L)	Dissolved Hg (ng/L)	Methyl Hg (ng/L)	Dissolved MeHg (ng/L)
CMPW3-0	4.80	3.31	0.418	0.259
CMPW3-10	5.51	3.01	0.711	0.231
CMPW3-20	5.12	2.42	1.106	0.227
CMPW3-30	5.47	2.85	1.154	0.695
CMPW3-40	7.19	3.99	1.431	0.755
CMPW3-45	23.69	9.90	7.773	3.790

CMPW4-0	5.83	3.39	0.579	0.261
CMPW4-10	5.91	3.13	0.916	0.210
CMPW4-20	5.45	2.41	1.376	0.398
CMPW4-30	5.00	2.46	1.792	0.937
MTW1-0	4.31	2.76	0.694	0.401
MTW2-0	4.25	2.80	0.579	0.311
MTW2-10	4.81	2.95	0.421	0.421
MTW2-20	4.85	2.68	0.942	0.493
MTW2-30	5.09	2.75	0.996	0.524
MTW2-40	5.14	2.77	1.026	0.572
MTW3-0	4.56	2.74	0.619	0.314
MTW3-10	66.86	7.03	1.451	1.449
MTW4-0	5.75	3.79	0.900	0.788
MTW4-2.5	6.80	4.08	0.950	0.798
MCW1-0	5.09	4.19	0.562	0.330
MCW1-10	4.43	3.48	0.617	0.302
MCW1-20	4.18	3.13	0.592	0.380
MCW1-30	4.82	3.43	1.144	0.825
MCW1-40	4.48	4.46	1.847	1.222
MCW2-0	6.72	4.21	0.491	0.384
MCW2-5	7.35	4.21	0.529	0.395
MCW3-40	6.73	3.90	1.817	1.120
MCW4-40	5.87	5.27	1.012	0.693
MCW5-10	341.96	4.11	1.547	0.404
MCHS	5.87	1.50	0.124	0.102
MCG1	NR	7.43	NR	2.001
MCG2	NR	12.10	NR	1.463

Hg in water speciation

	Inorganic Particulate (ng/L)	Inorganic Dissolved (ng/L)	Methylated Particulate (ng/L)	Methylated Dissolved (ng/L)
CMPW3-0	1.33	3.05	0.159	0.259
CMPW3-10	2.02	2.78	0.480	0.231
CMPW3-20	1.82	2.19	0.879	0.227
CMPW3-30	2.16	2.16	0.459	0.695

CMPW3-40	2.52	3.24	0.676	0.755
CMPW3-45	9.81	6.11	3.983	3.790
CMPW4-0	2.12	3.13	0.318	0.261
CMPW4-10	2.07	2.92	0.706	0.210
CMPW4-20	2.06	2.01	0.978	0.398
CMPW4-30	1.69	1.52	0.855	0.937
MTW1-0	1.26	2.36	0.293	0.401
MTW2-0	1.18	2.49	0.268	0.311
MTW2-10	1.86	2.53	0.000	0.421
MTW2-20	1.72	2.19	0.449	0.493
MTW2-30	1.87	2.23	0.472	0.524
MTW2-40	1.92	2.20	0.454	0.572
MTW3-0	1.52	2.43	0.305	0.314
MTW3-10	59.83	5.58	0.002	1.449
MTW4-0	1.85	3.00	0.112	0.788
MTW4-2.5	2.57	3.28	0.152	0.798
MCW1-0	0.67	3.86	0.232	0.330
MCW1-10	0.64	3.18	0.315	0.302
MCW1-20	0.84	2.75	0.212	0.380
MCW1-30	1.07	2.61	0.319	0.825
MCW1-40	*No data*	*No data*	*No data*	1.222
MCW2-0	2.40	3.83	0.107	0.384
MCW2-5	3.01	3.82	0.134	0.395
MCW3-40	2.13	2.78	0.697	1.120
MCW4-40	0.28	4.58	0.319	0.693
MCW5-10	336.71	3.71	1.143	0.404
MCHS	4.35	1.40	0.022	0.102
MCG1	*No data*	5.43	*No data*	2.001
MCG2	*No data*	10.64	*No data*	1.463

Core MEL1 physical properties

Depth (cm)	Water Fraction	Bulk Dry Density	Mass Accumulation Rate
1	0.84	0.16	0.17
3	0.79	0.22	0.23

5	0.79	0.22	0.23
7	0.79	0.23	0.24
9	0.79	0.22	0.23
11	0.78	0.23	0.24
13	0.77	0.25	0.26
15	0.75	0.27	0.28
17	0.75	0.27	0.28
19	0.75	0.27	0.28
21	0.75	0.27	0.28
23	0.75	0.27	0.28
25	0.75	0.27	0.29
27	0.74	0.28	0.29
29	0.74	0.27	0.29
31	0.75	0.27	0.28
33	0.75	0.27	0.28
35	0.74	0.28	0.29
37	0.74	0.28	0.29
39	0.74	0.28	0.29
41	0.73	0.29	0.31
43	0.72	0.30	0.31
45	0.72	0.30	0.32
47	0.71	0.32	0.33
49	0.68	0.35	0.37
51	0.63	0.41	0.43
53	0.61	0.43	0.45
55	0.55	0.51	0.54
57	0.48	0.60	0.63
59	0.45	0.64	0.67
61	0.38	0.74	0.77
63	0.44	0.66	0.69
65	0.45	0.65	0.68
67	0.42	0.68	0.72
69	0.53	0.54	0.56
71	0.61	0.44	0.46
73	0.58	0.47	0.49
75	0.59	0.46	0.48
77	0.56	0.49	0.52
79	0.77	0.25	0.26
81	0.70	0.32	0.34

Core MEL2 physical properties

Depth (cm)	Water Fraction	Bulk Dry Density	Mass Accumulation Rate
0.5	0.91	0.09	0.09
1.5	0.94	0.06	0.06
2.5	0.90	0.10	0.11
3.5	0.93	0.07	0.07
4.5	0.90	0.10	0.10
5.5	0.90	0.10	0.11
6.5	0.91	0.09	0.09
7.5	0.91	0.10	0.10
8.5	0.87	0.13	0.14
9.5	0.86	0.15	0.15
11	0.86	0.15	0.16
13	0.84	0.17	0.18
15	0.84	0.17	0.17
17	0.83	0.18	0.19
19	0.84	0.17	0.18
21	0.83	0.17	0.18
23	0.82	0.19	0.20
25	0.82	0.19	0.20
27	0.81	0.20	0.21
29	0.81	0.20	0.21
31	0.81	0.20	0.21
33	0.81	0.20	0.21
35	0.79	0.22	0.23
37	0.80	0.21	0.22
39	0.80	0.21	0.22
41	0.65	0.38	0.40
43	0.74	0.28	0.29
45	0.80	0.22	0.23
47	0.78	0.23	0.25
49	0.78	0.23	0.24
51	0.82	0.19	0.20
53	0.80	0.21	0.22
55	0.79	0.22	0.23

57	0.79	0.22	0.23
59	0.80	0.21	0.23
61	0.82	0.18	0.19
63	0.82	0.19	0.20
65	0.80	0.21	0.22
67	0.80	0.22	0.23
69	0.79	0.22	0.23
71	0.79	0.23	0.24
73	0.77	0.25	0.26
75	*No data*	*No data*	*No data*
77	0.79	0.22	0.23
79	0.79	0.23	0.24
81	0.77	0.25	0.26
83	0.76	0.25	0.27
85	0.77	0.24	0.25
87	0.77	0.24	0.25
89	0.77	0.24	0.26
91	0.75	0.27	0.28
93	0.74	0.28	0.29
95	0.74	0.28	0.30
97	0.76	0.26	0.27
99	0.77	0.24	0.25
101	0.75	0.27	0.28
103	0.76	0.25	0.26
105	0.74	0.28	0.29
107	0.80	0.21	0.22
109	0.80	0.22	0.23
111	0.77	0.25	0.26
113	0.71	0.31	0.33
115	0.64	0.40	0.42
117	0.71	0.31	0.33
119	0.63	0.40	0.42
121	0.58	0.47	0.49
123	0.61	0.43	0.45
125	0.59	0.46	0.49
127	0.40	0.71	0.74
129	0.26	0.92	0.96

131	0.23	0.97	1.01
133	0.59	0.46	0.48
135	0.77	0.24	0.25
137	0.75	0.27	0.29
139	0.78	0.24	0.25
141	0.75	0.27	0.28
143	0.79	0.22	0.23

Core MEL1 chemical composition

Depth	Hg ppb	%C	%N	%S
1	1465.6	6.3582	0.6763	
3	1056.2	6.0956	0.6552	
5	986.2	5.8416	0.6244	
7	1188.5	6.1047	0.6618	
9	1181.3	6.1216	0.6042	0.9771
11	1361.0	6.1728	0.6573	
13	1079.1	5.6406	0.5632	
15	1092.6	5.5348	0.5634	
17	1090.4	5.6870	0.6106	
19	1022.8	5.7577	0.5710	
21	1115.5	5.5564	0.5630	0.6407
23	1195.7	5.6915	0.6176	
25	1173.4	5.6924	0.6269	0.5199
27	1135.7	5.2955	0.5197	
29	1030.1	5.1694	0.5215	
31	1270.4	5.2630	0.5171	
33	1161.0	5.0570	0.4960	
35	938.5	5.0726	0.5284	
37	917.5	4.8081	0.4753	0.5866
39	765.9	4.8114	0.5281	
41	417.8	4.2233	0.4386	
43	596.3	4.4019	0.4976	
45	710.6	3.9601	0.4116	
47	481.5	4.0096	0.4690	
49	377.2	2.7613	0.3725	
51	415.1	2.2508	0.3190	

53	333.0	2.2839	0.2649	
55	311.5	1.5496	0.1937	
57	132.9	0.8710	0.1236	0.2237
59	126.7	1.0904	0.1711	
61	107.0	0.6210	0.1106	
63	206.8	0.8569	0.1497	
65	137.7	1.2630	0.1937	
67	76.2	0.9350	0.1985	
69	263.7	2.2828	0.2584	0.3849
71	461.2	3.2719	0.3951	
73	522.6	3.0023	0.3329	
75	589.5	2.9478	0.3203	
77	649.4	3.7100	0.3377	
79	1611.4	6.2880	0.6421	
81	985.2	3.8713	0.4359	

Core MEL2 chemical composition

Depth	Hg ppb	%C	%N	%S
0.5	7111.73	11.579	1.379	
1.5	7014.67	12.078	1.492	1.3111
2.5	6702.43	12.076	1.469	
3.5	8325.95	11.069	1.319	
4.5	7521.92	10.540	1.258	
5.5	8211.41	10.728	1.277	
6.5	7683.95	10.564	1.287	1.3119
7.5	8105.14	10.053	1.166	
8.5	8144.83	8.674	0.957	
9.5	8873.58	8.406	0.919	
11	7978.91	8.417	0.945	
13	9362.01			
15	8755.63			
17	8210.15			
19	8334.03	7.330	0.806	
21	9977.68	7.335	0.775	
23	8377.84	7.404	0.817	
25	8251.96	6.663	0.754	1.7784

27	11774.84	5.770	0.673	2.9634
29	10468.22	6.665	0.667	
31	8791.08	7.982	0.853	
33	11263.10	6.688	0.683	
35	10185.87	6.547	0.687	
37	7156.04	5.800	0.645	
39	7348.92	4.823	0.587	1.5738
41	4264.69	2.898	0.382	
43	7620.63	5.434	0.599	
45	9289.94	6.507	0.710	
47	8929.39	5.691	0.662	
49	6978.47	5.170	0.560	1.5468
51	9743.03	5.591	0.651	
53	11944.43	7.306	0.796	1.1704
55	13025.23	8.390	0.879	
57	9826.92	9.745	1.012	
59	10451.55	10.259	0.978	
61	8351.97	8.323	0.757	
63	6237.47	8.253	0.709	
65	6089.08	9.329	0.818	1.1899
67	5335.08	8.205	0.799	
69	6053.38	8.628	0.799	
71	6324.90	8.620	0.836	
73	5217.17	8.200	0.775	
75	4811.05	6.621	0.699	
77	4683.66	5.984	0.535	
79	5741.38	6.376	0.611	
81	6098.72	6.094	0.551	
83	6016.67	6.415	0.596	
85	7295.61	6.738	0.640	
87	7571.49	7.090	0.671	
89	7061.67	6.745	0.655	1.4737
91	6762.39	6.414	0.630	
93	7628.82	6.507	0.616	1.6787
95	7027.41	5.838	0.527	
97	7551.42	5.557	0.484	
99	7366.99	6.871	0.564	

101	5457.81	6.227	0.537	1.2123
103	7077.79	6.481	0.598	
105	10265.46	6.037	0.568	
107	8647.45	7.301	0.737	1.9736
109	8349.04	7.092	0.720	
111	4605.17	7.285	0.673	
113	1486.40	7.019	0.665	
115	692.38	5.919	0.576	
117	737.79	8.452	0.802	
119	863.17	6.166	0.606	
121	631.49	7.725	0.695	
123	544.58	6.360	0.586	
125	448.86	5.208	0.460	
127	985.03	1.409	0.193	0.2676
129	383.91	0.345	0.087	
131	196.57	0.233	0.079	
133	3104.92	8.794	0.614	
135	3466.20	13.220	0.961	
137	3111.43	12.617	0.930	
139	5780.34	13.558	1.056	
141	4217.71	12.147	0.886	
143	4896.05	14.562	1.032	0.7155

Core CLE2 and CLE3 Hg content

Core CLE2 depth	Hg ppb	Core CLE3 depth	Hg ppb
1	1437	0.5	1607
3	2371	1.5	2281
5	2461	2.5	2281
7	2470	3.5	2946
9	2234	4.5	2428
11	2477	5.5	2200
13	2293	6.5	2241
15	2103	7.5	1968
17	2356	9	2496
19	2406	11	2433
21	2340	13	2664
23	2266	15	2023
25	1822	17	1299

27	2796		19	1965
29	2731		21	2913
31	3121		23	2832
33	2800		25	2926
35	3173		27	2915
37	3041		29	3468
39	2348		31	2709
41	2807		33	2806
43	2505		35	2996
45	1682		37	2870
47	1281		39	2771
49	1163		41	2246
			43	3029
			45	4372
			47	3616
			49	1395
			51	593
			53	3109
			55	2926
			57	2990
			59	2975
			61.5	2396
			64.5	2517
			67	2158

Core CLE12 chemical composition

Depth	Hg ppb	C wt %	$\delta^{13}C$	N wt %	$\delta^{15}N$
25	3439	7.256	-20.561	0.769	2.237
27	4177	8.405	-19.970	0.891	2.393
29	4247	8.503	-19.886	0.931	2.266
31	4157	8.271	-20.794	0.877	2.341
33	3876	8.170	-21.238	0.970	-4.847
35	3465	7.528	-21.634	0.790	2.448
37	3095	7.598	-21.795	0.809	2.146
39	3057	7.373	-22.228	0.809	2.032
41	2215	7.974	-21.715	0.907	1.925
43	2042	7.655	-20.701	0.879	2.012
45	2988	8.714	-22.882	0.984	2.864
47	2918	7.522	-23.356	0.849	2.880

49	3308	7.695	-22.888	0.865	2.680
51	3163	8.533	-21.901	0.875	2.352
53	3766	8.385	-20.786	0.865	2.250
55	3485	7.647	-21.810	0.819	2.052
57	2401	7.039	-21.446	0.770	1.816

Core KCEL2 chemical composition

Depth	Hg ppb	C wt %	N wt %
1	3138	7.639	0.735
5	1491	5.463	0.521
7	1586	5.622	0.523
17	392	1.497	0.162
23	2484	9.929	0.788
31	1317	7.464	0.677
35	1157	7.206	0.656
41	1090	7.837	0.730
45	658	4.453	0.415
51	580	6.920	0.681
61	384	4.651	0.448
67	412	6.129	0.559
81	929	8.048	0.801
87	726	6.654	0.670

Core KCEL5 chemical composition

Depth	Hg ppm	C wt %	$\delta^{13}C$	N wt %	$\delta^{15}N$
1	1930	8.858		0.697	
6	1970	8.155	-23.81	0.660	3.23
9	2132	8.499		0.642	
13	2153	7.812		0.591	
20	1885	7.345		0.625	
25	1467	5.950		0.460	
27	1899	8.012		0.644	
30	1715	8.114		0.634	
32	1553	6.788		0.529	
33	2338	7.233		0.642	
38	3012	9.683	-22.37	0.770	2.91

41	3262	9.522		0.783	
44	3230	11.280	-19.85	0.912	2.52
46	2464	12.085	-17.84	0.965	1.95
47	1678				
50	1128	7.366		0.577	
50	1128	7.771		0.627	
53	904	8.813		0.742	
57	679				
60		5.933	-16.77	0.500	1.42
60		6.194	-16.77	0.529	1.42
59		6.196	-16.77	0.499	1.42
61	648				
63	789	5.977		0.563	
65	476				
67	595	4.881		0.502	
70	213	4.916	-18.09	0.512	2.06
73	722	5.968		0.537	
76	551	6.038		0.551	
78	358	5.150		0.481	
80		4.730	-21.41	0.443	0.37
79	368	4.736	-21.41	0.426	0.37
81	270				
88	3175	9.272	-20.44	0.729	2.73

Core MEL2 ^{210}Pb

Depth	Excess Pb210 (mBq g^{-1})	Age	Mm year^{-1}
0.5	269.456		
1.5	352.228	11.396	1.3162
2.5	261.269	21.136	1.1828
3.5	246.344	23.054	1.5182
4.5	209.340	28.361	1.5867
5.5	258.043	21.541	2.5532
6.5	259.737	21.328	3.0476
7.5	181.220	33.064	2.2683
8.5	78.757	60.236	1.4111
9.5	32.776	88.82	1.0696
11.0	49.926	75.098	1.4647
13.0	10.803	125.01	1.0399

| 15.0 | 20.274 | 104.48 | 1.4356 |